

DESIGNING ADVANCED CELL ENCAPSULATION SYSTEMS FOR TYPE 1
DIABETES (T1D) TREATMENT

A Dissertation

Presented to the Faculty of the Graduate School
of Cornell University

In Partial Fulfillment of the Requirements for the Degree of
Doctor of Philosophy

by

Duo An

May 2018

© 2018 Duo An

DESIGNING ADVANCED CELL ENCAPSULATION SYSTEMS FOR TYPE 1 DIABETES (T1D) TREATMENT

Duo An, Ph. D.

Cornell University 2018

Type 1 diabetes (T1D) is an autoimmune disease in which the patient's own immune system attacks and destroys the insulin-producing beta cells in the pancreas. It is estimated that in the US alone there are as many as three million people with T1D, with approximately 80 newly diagnosed patients every day. One in every 400 children and adolescents in the US has T1D and the rate of T1D incidence among children under the age of 14 is estimated to increase by 3% annually worldwide. Current treatments include injections and infusion of exogenous insulin and require constant attention and strict patient compliance. The transplantation of pancreases or islets offers a better alternative. However, its wide application is limited by the need for long-term immunosuppression and a persistent shortage of donor organs. Cell encapsulation has been shown to hold promise for effective, long-term treatment of T1D. However, encapsulation systems developed to date still face various challenges. For example, alginate hydrogel capsules, despite their biocompatibility and function, are difficult to retrieve or replace completely due to the large number of capsules required for effective treatment and the complicated organ structures in the transplantation site (i.e. peritoneal space), contributing to risks and concerns in case of transplant failure or medical complications. On the other hand, macroscopic devices (e.g. planar diffusion chambers), although considered retrievable, are challenging to scale up to a clinically relevant capacity due to their small surface area for mass transfer. In this thesis, I present three independent yet correlated research projects developing advanced cell encapsulation systems. Firstly, I developed a novel

method to fabricate toroidal particles. Alginate hydrogel toroidal particles have a shorter diffusion path within compared to conventional spherical alginate hydrogel particles, facilitating mass transport and benefiting encapsulated cells. Secondly, to enhance the mechanical robustness of the hydrogel and prevent cells from escaping, I engineered a novel nanofiber-enabled encapsulation device by combining electrospun nanofibers with biocompatible hydrogel. Last but not least, to further push cell encapsulation therapies toward clinical applications, I designed a retrievable and scalable device. I demonstrated the therapeutic potential of the device through the correction of chemically induced diabetes in C57BL/6 mice using rat islets for 3 months as well as in immunodeficient SCID-Beige mice using human islets for 4 months. I further showed, as a proof of concept, the scalability and retrievability of the device in dogs. In general, these projects may contribute to a cellular therapy for T1D.

BIOGRAPHICAL SKETCH

Duo An was born in Shijiazhuang, Hebei, China. He had a joyful childhood living with his parents. At the age of eleven, his family moved to Beijing, China where he continued his education in Beijing No.166 Middle School and Beijing No.5 high school. At the age of 18, Duo went to the University of Science and Technology of China (USTC) in Hefei, Anhui, China studying Chemistry. During his four-year college life in USTC, Duo has been actively exploring his research interests. He joined the USTC iGEM team and learned and practiced in a synthetic biology lab for his freshman year. In 2010, he went to the US for the first time as one of the USTC iGEM team representatives and gave a presentation at the Tang Center at MIT. After coming back to USTC, Duo joined Professor Shu-Hong Yu's group conducting research in synthesizing novel nanomaterials for bioimaging applications. In 2013, Duo was luckily admitted to the Ph.D. program in the Department of Biological and Environmental Engineering at Cornell University. Duo was fortunate to have two wonderful advisors, Professor Dan Luo and Professor Minglin Ma. Under their supportive guidance, Duo's research focused on developing novel cell encapsulation systems for type 1 diabetes treatment. Besides devoting himself to this exciting research, Duo lived a happy life in Ithaca enjoying the gorgeous natural scenery and extra-long winter at Cornell for five years. He is now ready to move on to start his new journey.

To my parents

ACKNOWLEDGMENTS

I would like to express my special appreciation to my Ph.D. advisors Professor Dan Luo and Professor Minglin Ma, for their great guidance and valuable advice throughout my dissertation, as well as my professional development. Both Dan and Minglin are greatly helpful and supportive, even though they are very busy, they are always there to help me whenever needed. They are always ready to give suggestions and share their experiences not only in research, but also in general life. I felt very lucky to have Dan and Minglin as my advisors, and I could not have imagined having better advisors and mentors for my Ph.D. study. I am also very indebted to my other committee member Professor Ulrich Wiesner for his constructive advice on my research projects.

In addition, I would like to acknowledge my lab mates and my collaborators, especially Yen-Chun Lu, Alan Chiu, Songming Peng, Thomas Derrien, Wei Song, Qingsheng Liu, Longhai Wang, Yu Zhang, Yehudah Pardo, Shogo Hamada, Ken Yancy, Yue Hu, Dong Wang, Alex Warning, Chun-Ti Chang, Yewei Ji, Fredrik Wolfhagen Sand, Louise Winkel for their help, suggestions and discussions in both my profession and my life.

Furthermore, I would like to thank my parents, Jinghui An and Jinhuan Duo, for their endless love, which helped me get through the difficulties and devote myself to the research.

TABLE OF CONTENTS

CHAPTER 1: INTRODUCTION.....	2
1.1 Cell therapy for type 1 diabetes.....	2
1.2 Microencapsulation system	7
1.3 Macroencapsulation systems.....	14
1.4 Mass transport kinetics and transplantation sites.....	20
1.5 Significance of this dissertation	24
CHAPTER 2: DEVELOPING MICROENCAPSULATION SYSTEM WITH SHAPED PARTICLES	26
2.1 Introduction	26
2.2 Materials and Methods.....	29
2.2.1 Materials.....	29
2.2.2 Preparation of VRP and microVRP.....	29
2.2.3 Characterizations	30
2.2.4 Cell encapsulation	30
2.2.5 Cell-free production of model protein	30
2.3 Results and Discussions	31
2.3.1 Fabrication of VRP by freezing vortex rings.....	31
2.3.2 Mass production of microVRP	37
2.3.3 Theoretical analyses and simulation.....	40
2.3.4 MicroVRP formed with other materials and reactions	44
2.3.5 Hydrogel donut-microVRP for bio-encapsulation	50
2.3.6 Composite, compartmentalized or directionally assembled donut-microVRP	55
2.4 Conclusion.....	58
CHAPTER 3: DEVELOPING ROBUST, HYDROGEL-BASED, NANOFIBER-ENABLED ENCAPSULATION DEVICES FOR CELL THERAPIES	59
3.1 Introduction	59
3.2 Materials and Methods.....	62
3.2.1 Chemicals	62
3.2.2 Animals	62
3.2.3 Fabrication of electrospun nanofiber tubes or chambers	62
3.2.4 Fabrication of NEEDs.....	63

3.2.5 Characterizations	64
3.2.6 Cell viability assay-MTT	64
3.2.7 Rat islet isolation and purification	64
3.2.8 Islets encapsulation	65
3.2.9 Insulin secretion from encapsulated islets on glucose stimulation	66
3.2.10 Transplantation	67
3.2.11 Blood glucose monitoring.....	67
3.2.12 Histological analysis	68
3.3. Results and Discussion.....	68
3.3.1 Fabrication and characterization of NEEDs.....	68
3.3.2 Cell encapsulation and culture.....	76
3.3.3 Islet encapsulation and transplantation	80
3.3.4 Discussion.....	84
3.4. Conclusion.....	86
CHAPTER 4: DEVELOPING A RETRIEVAL AND SCALABLE CELL ENCAPSULATION DEVICE FOR POTENTIAL TREATMENT OF TYPE 1 DIABETES	87
4.1 Introduction	87
4.2 Materials and Methods.....	88
4.2.1 Chemicals	88
4.2.2 Animals	89
4.2.3 Characterizations	89
4.2.4 Fabrication of modified threads.....	90
4.2.5 Rat islet isolation and purification	90
4.2.6 Cell encapsulation	91
4.2.7 Static glucose-stimulated insulin secretion (GSIS) assay.....	92
4.2.8 Perfusion test.....	93
4.2.9 Implantation and retrieval in mice	93
4.2.10 Laparoscopic implantation and retrieval in dogs	95
4.2.11 Blood glucose monitoring.....	96
4.2.12 Histological analysis and immunostaining.....	96
4.2.13 Statistical Analysis.....	98
4.3. Results and Discussion.....	98
4.3.1 Design and Fabrication of the Device.....	98

4.3.2 Characterizations of the Mechanical Robustness, Mass Transfer Property and Biocompatibility.....	102
4.3.3 Diabetes Correction in Mice	111
4.3.4 Scale-up and Test of Retrievability in Dogs	120
4.3.5 Discussion.....	125
4.4 Conclusion.....	125
CHAPTER 5: CONCLUSION AND FUTURE PERSPECTIVE.....	127
5.1 Conclusion.....	127
5.2 Future perspective	129
BIBLIOGRAPHY	131

LIST OF FIGURES

Figure 1.1. Schematic of cell encapsulation system.....	5
Figure 1.2. Schematics of different materials and devices for encapsulation of cells or cell aggregates	5
Figure 1.3. Increasing alginate sphere size results in reduced cellular deposition and fibrosis formation on the spheres	11
Figure 1.4. Combinatorially modified hydrogels with reduced subcutaneous inflammation and fibrosis.....	12
Figure 1.5. hESCs-derived β -cells encapsulated with modified alginate sustain normoglycemia in STZ-treated immune-competent C57BL/6J mice	13
Figure 1.6. Schematic illustration of an intravascular device	17
Figure 1.7. Schematic of the ViaCyte device	17
Figure 1.8. PDMS-CaO ₂ prevents hypoxia-induced cell death for pancreatic rat islets	18
Figure 1.9. Image and schematic of the Beta-O ₂ device demonstrating the ports for recharging oxygen and the encapsulation device	19
Figure 1.10. Laparoscopic images showing the microcapsules in the intraperitoneal space	23
Figure 1.11. Design and characteristics of the subcutaneous device-less cellular transplant site.....	23
Figure 2.1. A comparison of a sphere and a donut (torus)	28
Figure 2.2. Vortex ring formation by droplet dripping	33

Figure 2.3. Characterizations of nanoclay hydrogel donut-microVRP	34
Figure 2.4. Nanoclay hydrogel VRP formed by free-fall dripping	35
Figure 2.5. High speed camera images of the formation processes of the nanoclay hydrogel VRP	36
Figure 2.6. Mass production and size control of nanoclay hydrogel donut-microVRP	38
Figure 2.7. Shape control of the nanoclay hydrogel microVRP.....	39
Figure 2.8. Mechanistic study of the VRP formation process.....	42
Figure 2.9. The axisymmetric simulation results of the vortex ring formation over time for five situations	43
Figure 2.10. High speed camera images of an alginate solution impacting the conventional crosslinking buffer (100 mM CaCl ₂ solution).	45
Figure 2.11. MicroVRP fabricated from alginate and chitosan hydrogel	46
Figure 2.12. MicroVRP fabricated from nanosilica	47
Figure 2.13. DNA encapsulation and cell-free production using nanoclay hydrogel donut micro-VRP.....	52
Figure 2.14. Cell encapsulation using donut-micro-VRP	53
Figure 2.15. Mass transport property study	54
Figure 2.16. Composite and assembly of donut-microVRP.....	57
Figure 3.1. Design and fabrication of NEEDs.....	72
Figure 3.2. Microscopic images and digital photos of various electrospun nanofibers and nanofibrous tubes.....	73
Figure 3.3. Characterizations of NEEDs (bottom)	74

Figure 3.4. NEEDs with different hydrogel chemical compositions and their robust mechanical properties	75
Figure 3.5. <i>In vitro</i> model cell encapsulation and culture using NEEDs	78
Figure 3.6. <i>In vitro</i> cell encapsulation and viability test	79
Figure 3.7. Islet encapsulation and transplantation using NEEDs	82
Figure 3.8. Histology study of the retrieved NEEDs.....	83
Figure 4.1. Schematics and fabrication of the TRAFFIC device.	101
Figure 4.2. Characterizations of the mechanical robustness of TRAFFIC.....	105
Figure 4.3. <i>In vivo</i> mechanical stability test	106
Figure 4.4. 2-week fibrosis study	106
Figure 4.5. 3-month fibrosis study.	107
Figure 4.6. Characterizations of the biocompatibility of TRAFFIC	108
Figure 4.7. Characterizations of the mass transfer property of TRAFFIC	109
Figure 4.8. Permeability measurement of the TRAFFIC	110
Figure 4.9. Demonstration of therapeutic potential of TRAFFIC using rat islets	115
Figure 4.10. Transplantation of rat islets encapsulated in neat alginate fiber/TRAFFIC and allogenic mouse islets encapsulated with TRAFFIC.....	116
Figure 4.11. Long-term study of the transplantation of the rat islet encapsulated in TRAFFIC.....	117
Figure 4.12. Transplantation of human islets encapsulated in TRAFFIC into healthy mice	118
Figure 4.13. Demonstration of therapeutic potential of TRAFFIC using human islets	119

Figure 4.14. Scalability of TRAFFIC and laparoscopic retrieval 122

Figure 4.15. Weak mechanical stability of the device made from a “beads-on-a-string”
thread 123

Figure 4.16. Demonstration of rapid device retrieval and cell survival in a dog model
..... 124

LIST OF TABLES

Table 1.1. Islet and β -cell encapsulation systems currently in clinical trails	6
Table 2.1. Different shapes of the electrosprayed alginate hydrogel microparticles using different crosslinking buffers.....	48
Table 2.2. Different shapes of the electrosprayed chitosan hydrogel microparticles using different crosslinking buffers.....	49

CHAPTER 1: INTRODUCTION

1.1 Cell therapy for type 1 diabetes

Type 1 diabetes (T1D; also known as juvenile diabetes) represents 5-10% of the total diabetes population¹. It is estimated that in the US alone, there are as many as three million people with T1D with approximately 80 newly diagnosed patients every day². One in every 400 children and adolescents in the US has T1D and the rate of T1D incidence among children under the age of 14 is estimated to increase by 3% annually worldwide³. T1D is an autoimmune disease in which the patient's overactive immune system attacks and destroys the insulin-producing β -cells in the pancreas. Current standard treatments include injections or infusion of exogenous insulin, requiring constant attention and strict compliance. However, this treatment does not perfectly simulate insulin secretion from β -cells; consequently, a patient's blood glucose levels fluctuate despite close monitoring and frequent adjustments of insulin doses⁴, leading to many devastating effects such as blindness, neuropathy, amputations, heart disease and stroke⁵.

The transplantation of pancreases or islets offers a better alternative and has been shown to restore normglycemia^{6, 7}, allowing for tighter blood glucose control. For each transplant infusion, researchers use specialized enzymes to remove islets from the pancreases of donors. The islets are purified and counted in a lab. Patients typically receive two infusions with an average of 400,000 to 500,000 islets per infusion^{8, 9}. Once implanted, the beta cells in these islets begin to make and release insulin. The goal of the islets transplants are to help those patients who have difficulty in controlling their

blood glucose levels to achieve normal blood glucose levels with or without daily injections of insulin and to reduce or eliminate hypoglycemia unawareness¹⁰. It was reported that transplanted human pancreatic islets provide glycemic control, restoration of hypoglycemia awareness and protection from severe hypoglycemic events at 2 years in more than 70% of patients with previous hypoglycemia unawareness⁴.

Unfortunately, the scarcity of donor organs and requirement of life-long immunosuppression significantly compromise the widespread application of islet transplantation. The required chronic systemic immunosuppression puts patients at risk of organ damage, infection and malignancies¹¹. The recent development of human embryonic stem cell (hESC) stepwise differentiation leads to an efficient way to provide an unlimited supply of β -cells for transplantation. However, there is a concern that hESC-derived β -cells may contain undifferentiated stem cells, which may pose some regulatory concerns in terms of teratoma formation¹². These barriers may be overcome by encapsulating islets or hESC-derived β -cells inside an encapsulation device which provides physical barriers between transplanted cells and their recipients. These barriers permit the bidirectional diffusion of molecules such as the influx of oxygen, nutrients and growth factors and the outward diffusion of cell waste products and therapeutic proteins (insulin). At the same time, the device prevents immune cells and antibodies from destroying the encapsulated cells (Figure 1.1). An ideal islet encapsulation system should not only provide ample supply of nutrients and oxygen to sustain survival and function of sufficient amount of islets for the maintenance of normal glycaemia, but also serve as an immune barrier to prevent sensitization and rejection, and contain any potentially tumorigenic cells.

One of the first examples of using encapsulated cells for treatment of diabetes involved using semi-permeable membrane bags to encapsulate human insulinoma tissue and transplant them into rats in 1933¹³. Since then, extensive works have been done, and the field of immune-isolated transplantation became established¹⁴⁻¹⁶. Recently, researchers have successfully demonstrated that hESC can be differentiated to pancreatic progenitors or even β -cells *in vitro*¹⁷⁻¹⁹, which attracted more attention to the cell encapsulation field. A great deal of effort has focused on investigating the ideal cell encapsulation system from many approaches, such as encapsulation materials, site of transplantation, configuration of encapsulation device, and methods to improve vascularization and immune modulation²⁰. To date, a small number of encapsulation systems have been developed and applied clinically; some examples are summarized in Table 1.1⁴. Currently there are two major types of islets encapsulation systems: microencapsulation and macroencapsulation systems. In this thesis, I will discuss my approaches in developing novel cell encapsulation systems in both categories.

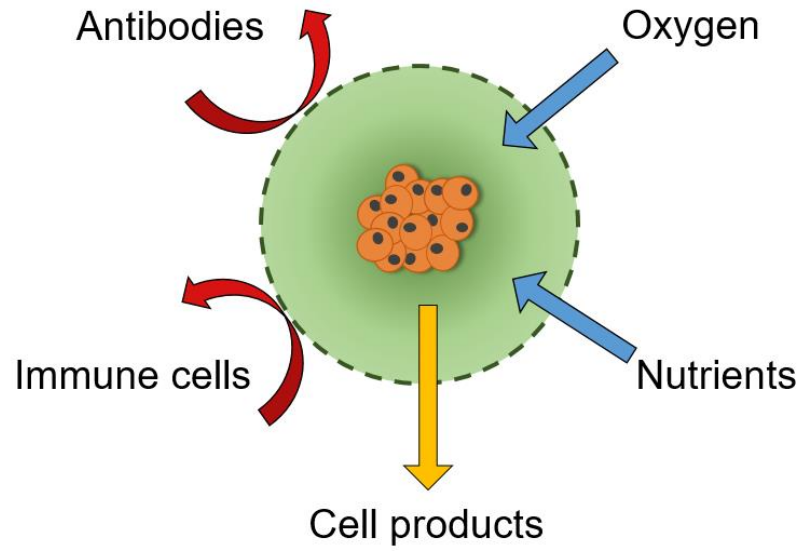


Figure 1.1. Schematic of cell encapsulation system.

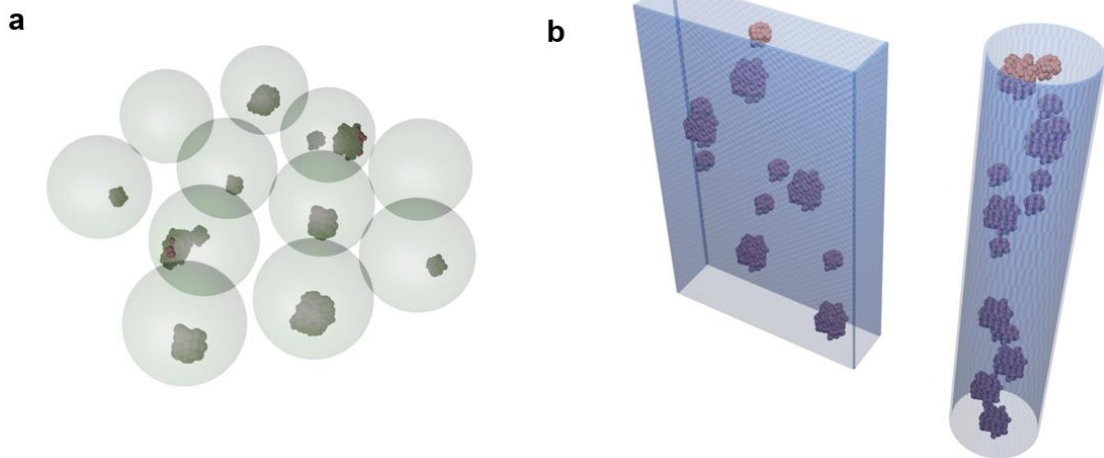


Figure 1.2. Schematics of different materials and devices for encapsulation of cells or cell aggregates. a, Microcapsules; b, Devices made of porous polymer membranes.

Device or method	Experimental intervention	Properties	Trial phase	Ref
Sernova Cell Pouch	Implantation of allogeneic islets into the Sernova Cell Pouch following pre-vascularization	<ul style="list-style-type: none"> • Subcutaneous • 2-12 weeks of pre-vascularization 	I/II	21
Diabecell	Laparoscopic delivery of alginate encapsulated porcine islets	<ul style="list-style-type: none"> • Peritoneal cavity • Immune suppression: no • 2×10,000 IEQ per kg deliveries 12 weeks apart; (total 20,000 IEQ per kg) 	II	22
Monolayer alginate encapsulation	A monolayer patch of alginate encapsulated allogeneic islets	<ul style="list-style-type: none"> • Subcutaneous • Immune suppression: phase IA=yes; phase IB=no • One 1-3 cm² patch 	I	23
Alginate encapsulation	Implantation of alginate encapsulated allogeneic islets	<ul style="list-style-type: none"> • Peritoneal cavity • Immune suppression: yes 	II	24
ViaCyte Encaptra	Encaptra containing allogeneic hESC-derived pancreatic progenitors	<ul style="list-style-type: none"> • Subcutaneous • 2, 4 or 6 Encaptra implants 	I/II	25
βAir artificial pancreas	Macroencapsulation of allogeneic islets in βair that provides oxygen to the cells	<ul style="list-style-type: none"> • Peritoneal cavity • Immune suppression: no • Daily O₂ injection 	I/II	26
Thrombin plasma gel	Allogeneic islets are suspended in a gel formed from autologous plasma and recombinant thrombin	<ul style="list-style-type: none"> • Omentum • Immune suppression: yes • 5,000 IEQ per kg 	I/II	27

Table 1.1. Islet and β-cell encapsulation systems currently in clinical trials.⁴

1.2 Microencapsulation system

Microencapsulation is a process by which small droplets or particles of liquid or solid materials are surrounded or coated with a continuous film of polymeric material. Capsules in the 0.3-1.5 mm range have been traditionally referred to as microcapsules in the cell encapsulation field²⁸. Microencapsulation of islets involves the envelopment of one to a few islets within their own individual capsule. The spherical shape of microcapsules offers a better diffusion capacity due to the greater surface-to-volume ratio. Microcapsules are generally mechanically stable and do not require complex or expensive manufacturing procedures. The most common implantation site is the peritoneal cavity²⁹. In most cases, microcapsules can be implanted into the patient by a simple injection procedure.

The first described cell microencapsulation dates back to 1964³⁰. The first attempt of using microcapsules to treat diabetes was made in 1980 by Lim and Sun³¹, where they used alginate-polylysine-polyethyleneimine capsules to encapsulate islets and demonstrated the prolonged isograft islet survival up to 3 weeks. In 1984, O'Shea et al. improved the microcapsule material by removing the polyethyleneimine component³². The use of alginate demonstrated substantial improvement by showing that the encapsulated islets remained viable for 1 year in one of the five animals used in the experiment. Numerous microencapsulation strategies have been shown to be effective in rodent diabetes models^{33, 34}. However, successful large animal and clinical trials are limited. In recent years, Living Cell Technologies has been conducting clinical trials on xenotransplantation of encapsulated porcine islets. However, there has always

been concerns about the overall safety of this xenotransplantation approach since efficacy data failed to achieve the desired success.

Researchers have always considered insufficient biocompatibility to be a major threat for clinical application of microcapsules. Insufficient biocompatibility of the materials applied is the most interpreted cause of the failure of the microencapsulated islets graft, where a nonspecific foreign body reaction against the microcapsules results in progressive fibrotic overgrowth of the capsules³⁵. This cellular overgrowth interferes with the mass transport of the oxygen and nutrient inside the microcapsules and causes islet cell death. Consequently, many efforts have been made to identify factors that are involved in determining the biocompatibility of microcapsules.

Many modifications of the encapsulation technology have been reported to reduce the host response against alginate-based microcapsules. Over a decade ago, researchers found that crude alginate was associated with the cellular overgrowth (mostly macrophages and fibroblasts)³⁶. As a consequence, the enveloped therapeutic cells experience necrosis due to the insufficient diffusion of the nutrients and oxygen. Since then, many efforts have been paid to purify the crude alginate and ultra-pure sodium alginate is now commercially available.

Not only the purity of the alginate but also the composition of the alginate has been studied. Alginate molecules are composed of mannuronic (M) and guluronic acids (G) and can be crosslinked by divalent ions (such as Ca^{2+} and Ba^{2+}) through the binding of consecutive blocks of G-molecules. By tuning the G/M ratio, some basic properties of the resulting hydrogel will change. Theoretically, high-G alginate hydrogel is more durable and associated with less islet protrusion^{37, 38}. However, it was found that high-

G alginate hydrogel microcapsules are associated with more inflammatory reactions than intermediate-G alginate hydrogel microcapsules^{38, 39}.

The size of the microcapsules also plays a significant role in determining the success of the encapsulation systems. There has been concern that the conventional size of the capsules (600-1,000 μm in diameter) may lead to diffusional limitations, which results in core hypoxia and delayed insulin secretion in response to glucose⁴⁰. Thus, a significant amount of effort has been devoted to reducing the size of the encapsulating capsules, with the aim of maximizing the surface-to-volume ratio⁴⁰. As a consequence, the conformal coating has arisen as a new encapsulation model for the immunoprotection of islets of Langerhans. Various fabrication procedures have been developed, including the alginate emulsification method, layer-by-layer assembly and the flow-focusing approach⁴⁰⁻⁴². However, although most of the conformal coating studies show some success *in vitro*, most technologies have not achieved success as immune barriers in preclinical and clinical models, still requiring systemic immunosuppression⁴³.

Recently, Veiseh et al. found that the overall sizes of the implanted microcapsules affect the host recognition and foreign body response. They showed that in rodent and non-human primate animal models, implanted spheres 1.5 mm and above in diameter significantly abrogate foreign body reactions and fibrosis when compared with smaller spheres (Figure 1.3). By using 1.5 mm alginate capsules encapsulating rat islets, they were able to restore blood glucose control of streptozotocin (STZ)-treated diabetic C57BL/6 mice for up to 180 days, five times longer than the control group with 0.5 mm alginate capsules⁴⁴. Moreover, these groups of researchers created a large

library of chemically modified alginate and tested the foreign body response of these alginate *in vivo*. It showed that three triazole-containing analogs substantially reduce foreign body reactions in both rodents and in non-human primates (Figure 1.4). It is claimed that the distribution of the triazole modification creates a unique hydrogel surface that inhibits recognition by macrophages and fibrosis deposition⁴⁵. These foreign-body response mitigating alginate derivatives were used to encapsulate human embryonic stem cells (hESCs) derived β -cells in capsules and transplanted in STZ treated C57BL/6 mice. The implants induced glycemic correction without immunosuppression for up to 174 days before retrieval (Figure 1.5)⁴⁶.

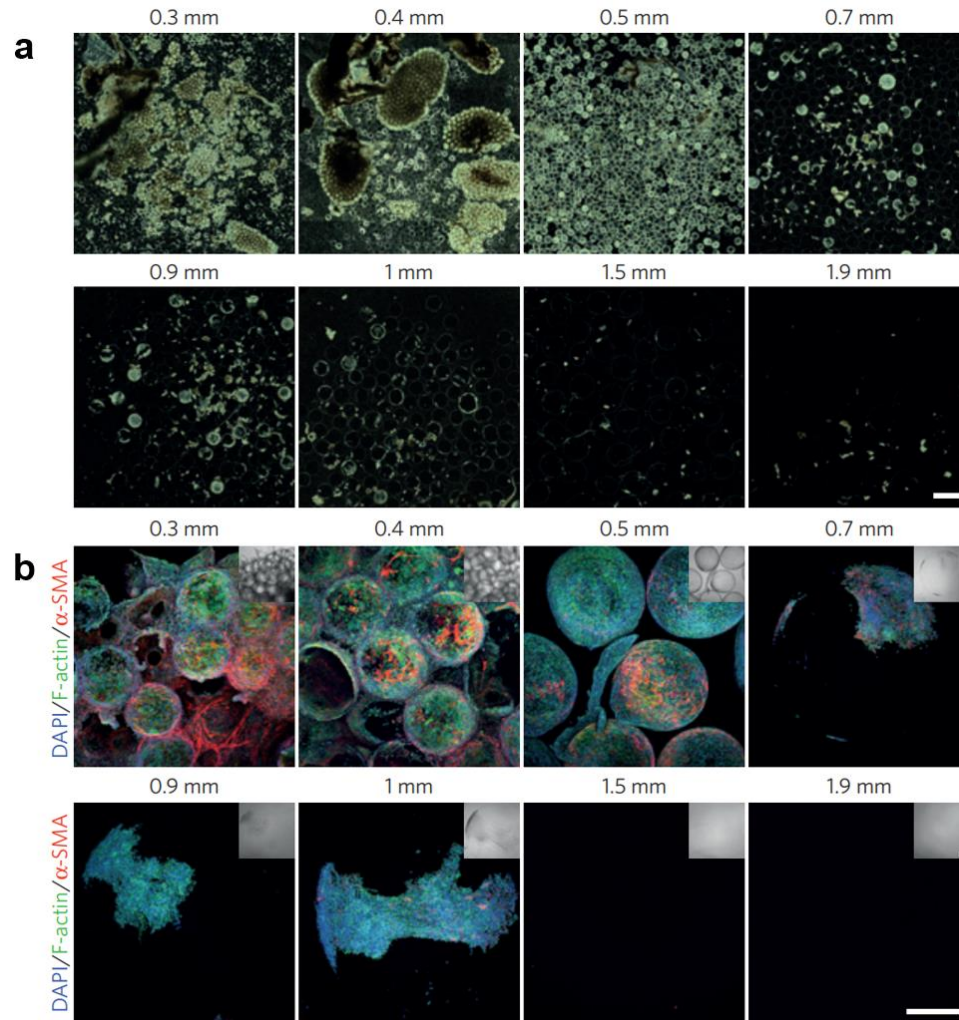


Figure 1.3. Increasing alginate sphere size results in reduced cellular deposition and fibrosis formation on the spheres. a, Dark-field phase contrast images obtained from retrieved spheres reveal a significant decrease in level of cellular overgrowth with increase in sphere size. Scale bar, 2 mm. b, Z-stacked confocal images of retrieved spheres immunofluorescence stained with DAPI (highlighting cellular nuclei), phalloidin (highlighting F-actin) and α -SMA (highlighting myofibroblast cells). Scale bar, 300 μ m.⁴⁴

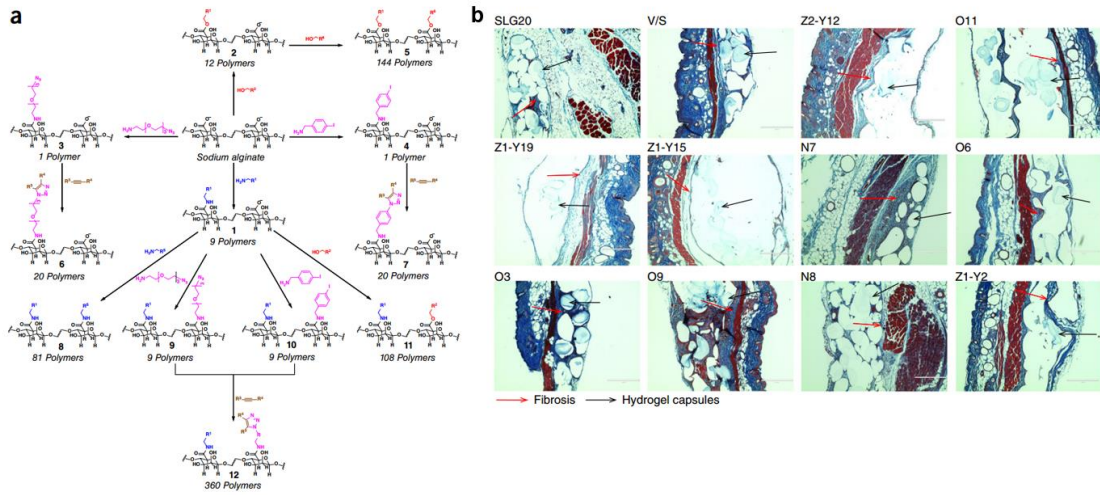


Figure 1.4. Combinatorially modified hydrogels with reduced subcutaneous inflammation and fibrosis. a, Scheme for the synthesis of 774 alginate analogs. b, Masson's trichrome (MT) 28-day subcutaneous histology of the top ten alginate analog microcapsules and the ultrapure control alginate microcapsules (SLG20, V/S = UPVLVG/SLG100 blend); n = 10 (controls) and n = 3 (experimental). Abnormal microcapsule morphology is caused by histological processing (dehydration) of the tissue. Scale bars, 400 μm .⁴⁵

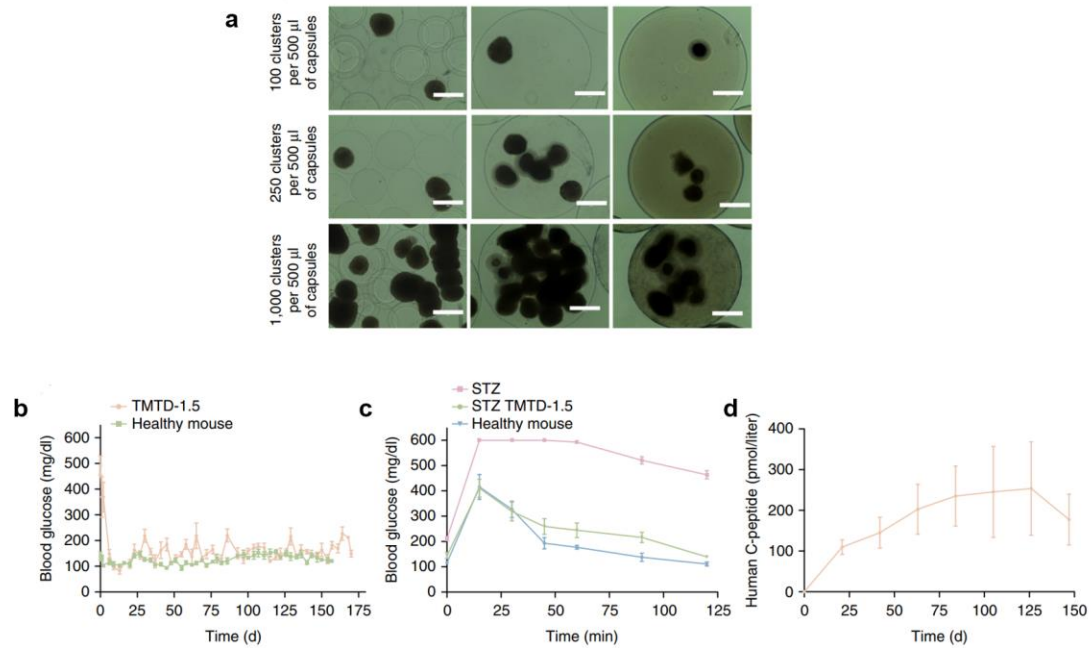


Figure 1.5. hESCs-derived β -cells encapsulated with modified alginate sustain normoglycemia in STZ-treated immune-competent C57BL/6J mice. a, Blood glucose levels in STZ-treated C57BL/6 mice implanted with hESCs-derived β -cells encapsulated with modified alginate at a dose of 250 clusters/mouse or healthy and non-transplanted C57BL/6 mice. b, Blood glucose levels of the mice shown in a together with a cohort of STZ-treated non-implanted mice that were subjected to an intravenous glucose tolerance test (IVGTT) 174 d after implantation. c, Human C-peptide levels in the blood of the STZ-treated C57BL/6 mice implanted with hESCs-derived β -cells (used in a).⁴⁶

1.3 Macroencapsulation systems

Macroencapsulation systems are generally much larger devices compared to microcapsules. They typically have a planar or cylindrical geometry, and a relatively smaller surface-to-volume ratio. In macroencapsulation systems, cells are physically isolated from directly interacting with the host tissues by the membrane of the encapsulation devices⁴. These devices rely on the host animal's own homeostatic mechanisms for the control of pH, metabolic waste removal, electrolytes, and nutrients²⁸. Macroencapsulation systems can be categorized into two general categories based on their association with the host vasculature: intravascular devices and extravascular devices.

Intravascular devices are connected or anastomosed directly to the existing host vasculature (Figure 1.6). The islets in these devices are in close contact with the blood stream which implies a fast exchange of glucose and insulin and a strict regulation of glucose levels^{47, 48}. Although the intravascular devices have shown some degree of success in various animal models^{49, 50}, there are some drawbacks (for instance, thrombosis, defects of the device, or potential infections) for wide applications in large numbers of diabetic patients³³.

The first reported extravascular macroencapsulation devices were developed by Algire and co-workers in the 1950s^{15, 16, 51}. Although most of the animal trials using these devices were compromised by insufficient oxygen and nutrient diffusion into the device, these early works emphasized the importance of the membrane biocompatibility, host cell membrane overgrowth, delays in immune rejection of encapsulated tissues and prevention of allograft rejection^{15, 52}. Later, in the early 1990s, Baxter healthcare

developed a planer cell encapsulation device, which consisted of encapsulated islets immobilized in flat membranes fastened to make a sealed chamber^{53,54}. The membrane was designed to encourage host vascularization to resolve the critical issue of oxygenation. Similar designs of the planer devices have been investigated by different research and pharmaceutical groups⁵². ViaCyte is currently using a similar device called Encaptra (Figure 1.7), which has a single membrane that is immunoisolating to protect the transplanted cells from direct interaction with immune cells, while allowing oxygen and nutrients to diffuse. ViaCyte is carrying out a phase I/II clinical trial for the delivery of hESC-derived pancreatic progenitors²⁵. Another approach associated with vascularization is the Sernova Cell Pouch⁵⁵, which aims to pre-vascularize a subcutaneous site before the administration of the islets into the pouch⁵⁶. Sernova is doing a phase I/II clinical trial on the implantation of allogeneic islets²¹.

It is well known that inadequate oxygen delivery due to a lack of immediate angiogenesis after implantation is the key factor limiting the functionality of cell-based devices⁵⁷⁻⁵⁹. Insufficient oxygen levels lead to cell apoptosis, particularly for high metabolic cells such as β -cells^{20, 60}. Even though vascularization of the implant may improve the oxygen concentration within the device, the time required for the formation of a fully functional vascularization is too long to maintain islet viability. Recently, Stabler and co-workers developed a novel oxygen-generating biomaterial in the form of polydimethylsiloxane (PDMS)-encapsulated solid calcium peroxide, PDMS-CaO₂⁵⁷. It is reported that a single PDMS-CaO₂ disk could enhance survival of rat pancreatic islets under hypoxic culture conditions (Figure 1.8)⁵⁷. Since 2005, Beta-O₂ has been exploring methods to provide exogenous oxygen to the encapsulated islets (Figure 1.9). The

device is implanted subcutaneously, with access ports used for daily filling with oxygen⁶¹. These Beta-O₂ studies have been successful in rodents and in large animals⁶¹.⁶² More recently, a case reported for this device in a single patient reported persistent islet graft function for 10 months with regulated insulin secretion and preserved islet morphology without immunosuppression⁶³.

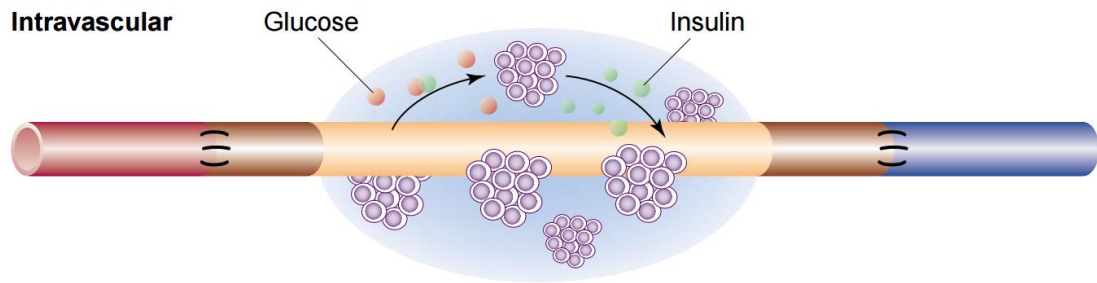


Figure 1.6. Schematic illustration of an intravascular device. Islets are enclosed in a chamber surrounding a selectively permeable membrane. The device is implanted as a shunt in the vascular system.³³

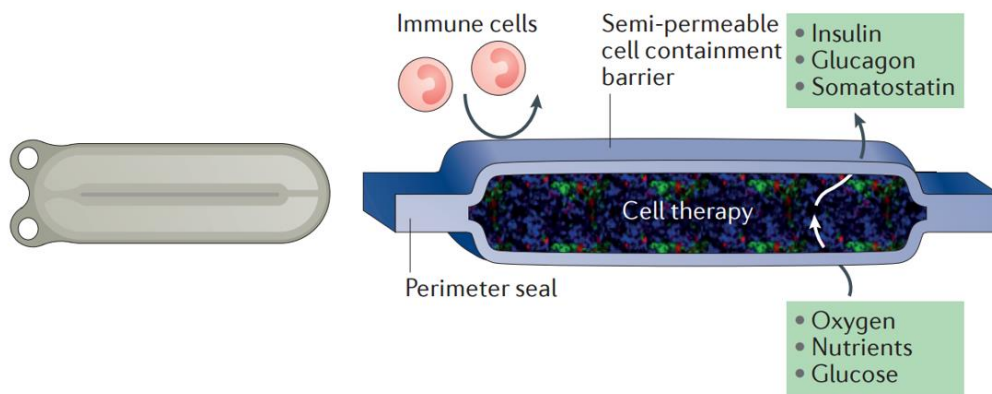


Figure 1.7. Schematic of the ViaCyte device.⁴

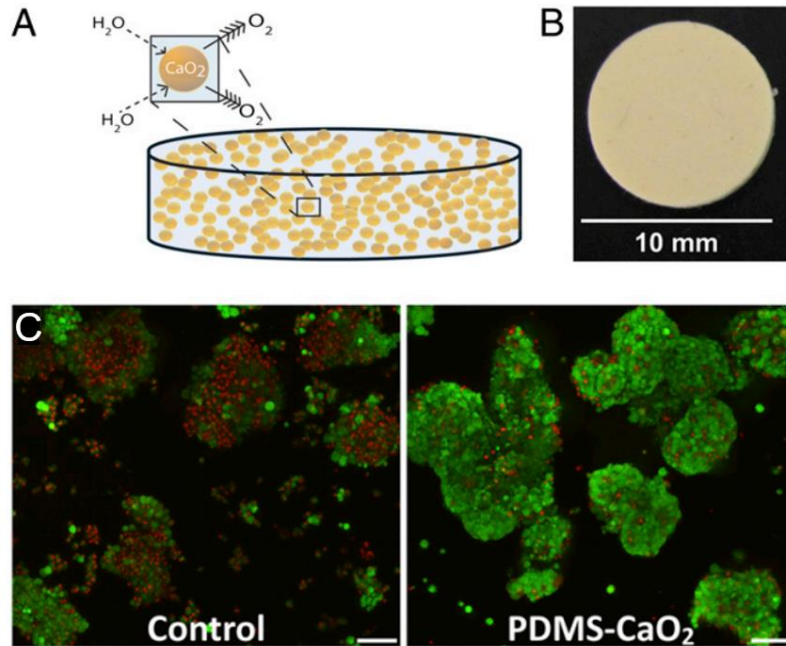


Figure 1.8. PDMS-CaO₂ prevents hypoxia-induced cell death for pancreatic rat islets. **a**, Schematic of oxygen-generating biomaterials, fabricated using PDMS-CaO₂. **b**, Photograph of PDMS-CaO₂ disk (10-mm diameter; 1-mm height). **c**, Representative confocal z-stacked culture at 0.05 mM oxygen without (control) or with a PDMS-CaO₂ disk. (Scale bars, 100 μ m.)⁵⁷

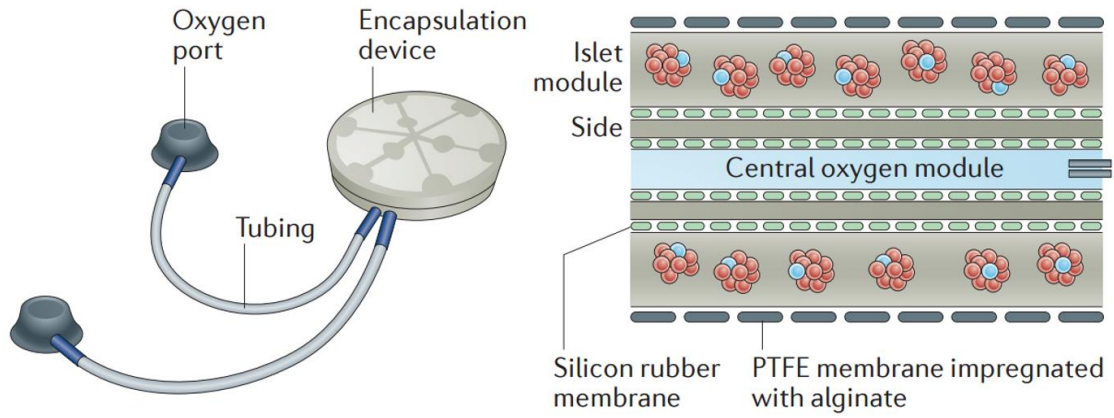


Figure 1.9. Image and schematic of the Beta-O2 device demonstrating the ports for recharging oxygen and the encapsulation device.⁴

1.4 Mass transport kinetics and transplantation site

The goal of islets transplantation is to reconstitute the physiological glucose homeostasis autonomously by the transplanted pancreatic β -cells. Although many hormones and neurotransmitters can induce insulin release, glucose is the main physiological insulin secretagogue⁶⁴. It has been shown that in healthy β -cells the release of insulin is oscillatory with relatively stable pulses of variable amplitude^{65, 66}. It is very challenging to maintain this subtle regulation by using encapsulated islets, since the production, secretion and diffusion of insulin through an encapsulation device is affected by various biological and physio-chemical factors^{67, 68}. It is reasonable to speculate that a larger surface-to-volume ratio is highly desired in any cell encapsulation system. In this regard, microencapsulation may naturally be superior to most of the macroencapsulation devices. However, the mass transport property is also affected by many other complications such as the size of the capsules/devices, the composition of the encapsulation materials, the fibrotic overgrowth, and transplantation site. It has been shown that insulin infusion into the peritoneal cavity causes a markedly delayed and reduced increase in peripheral blood insulin levels when compared to intraportal insulin infusion⁶⁹.

Besides insulin diffusion, inadequate oxygen delivery due to a lack of immediate angiogenesis after implantation is another very important factor which greatly limits the functionality of cell encapsulation devices⁵⁷⁻⁵⁹. Insufficient oxygen levels will cause cell apoptosis, especially for highly metabolic cells such as β -cells, which will reduce insulin production under low oxygen levels^{70, 71}. In a cell encapsulation system, oxygen diffuses from the surrounding blood vessels to the device, across the immunobarrier membrane

and then diffuse into the encapsulated cells⁴. Some studies have shown that the diffusion distance of the oxygen within the encapsulation materials has to be limited to within a few hundred microns⁷². Given the fact that in order to cure a human T1D patient, ~500,000 IEQs may be needed⁷³, the loading capacity of the cell encapsulation device remains a great challenge.

The transplantation site for encapsulation device is a controversial and highly critical issue to be considered⁷⁴. The site chosen will not only affect the mass transport kinetics mentioned above, but also determine the surgical complications and affect patients' acceptance of the treatment. In clinical islets transplantation, free islets are infused into the liver through the portal vein⁷⁵. In this case, the mass transport, including the diffusion of nutrients, oxygen and insulin, matches the physiological route. In the case of microencapsulation, the intraperitoneal space is the most popular site for transplantation, due to the ease of access via laparoscopy and less restriction of the volume to be transplanted (Figure 1.10). Moreover, there are much more body fluids in the intraperitoneal space compared to other transplantation sites. It is assumed that the deficiency of nutrients and oxygen is less severe when the cells are transplanted intraperitoneally. However, in contrast to the situation in rodent and pig models, microencapsulated islets transplanted into the peritoneal cavity show a tendency to clump in upright nonhuman primates and man due to gravity⁷⁶. An alternative transplantation site for microcapsules is a surgically created omental pouch⁷⁷. When transplanted into the omental pouch, the encapsulated cells are closer to pre-existing extensive vasculature and it is relative easy to retrieve the grafted capsules.

For macroscopic cell encapsulation devices, the most favorable transplantation site is the subcutaneous space. The implantation procedure is less invasive compared to implantation in the intraperitoneal space. However, due to the rare vascularization in the subcutaneous area, the transplanted cells usually experience poor oxygen supply. When encapsulation devices are placed under the skin, they may require an enhanced oxygen supply from an external source, as they are impermeable to vascular growth⁷⁶. There are a few studies show beneficial effects of neovascularization pretreatment using basic fibroblast growth factors (FGF) in islet transplantation, and demonstrated reversal of hyperglycemia up to 3 months in rodents^{78, 79}. Encapsulation devices developed by Theracyte and Sernova have a membrane or catheter that can promote vascularization. In the Sernova system, a catheter was implanted subcutaneously to induce vascularization, upon removal, a prevascularized subcutaneous site was created (Figure 1.11). Mouse syngeneic islets were transplanted into this prevascularized site and normoglycemia was maintained for >100 days.

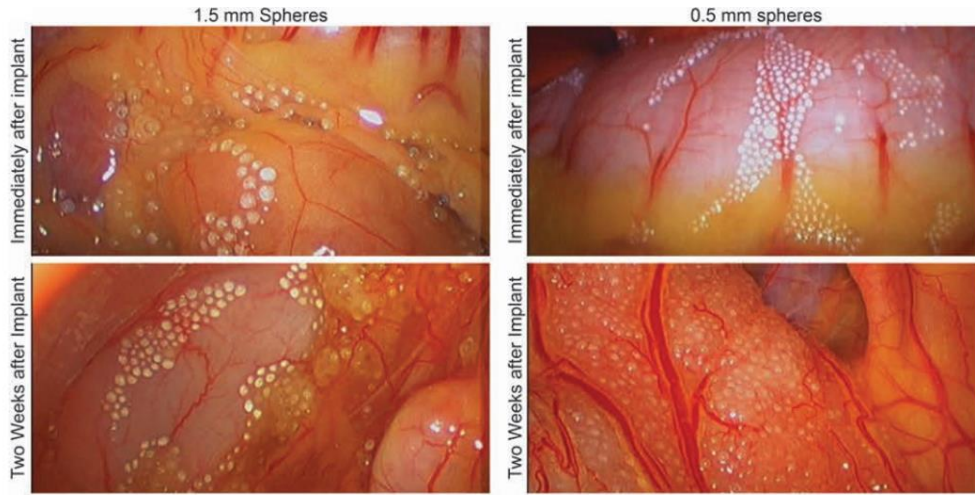


Figure 1.10. Laparoscopic images showing the microcapsules in the intraperitoneal space.⁴⁴

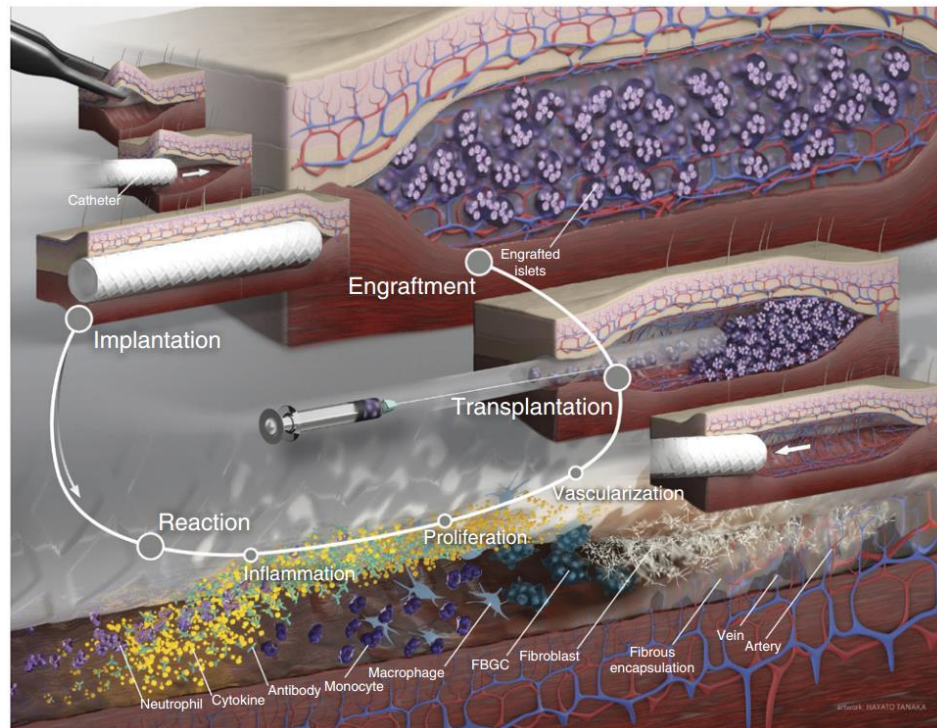


Figure 1.11. Design and characteristics of the subcutaneous device-less cellular transplant site.⁵⁵

1.5 Significance of this dissertation

Cell encapsulation holds great potential as a better treatment for type 1 diabetes. Even though extensive efforts have been made in various aspects, and some encapsulation systems are already in clinical trials, there are still many challenges remaining. For instance, there is an unmet need for an effective way to improve the mass transport property of the encapsulation materials, a secured encapsulation device that can ensure no cell penetration, and a system that is capable of delivering sufficient cell mass while still allowing convenient retrieval or replacement. In this dissertation, I will introduce three individual but correlated projects in which I studied the cell encapsulation from three different aspects. Firstly, I developed a novel fabrication method to prepare non-spherical particles by combining vortex ring formation process and gelation/precipitation reactions. Especially, by combining the vortex ring freezing method with the electrospray process, I was able to produce toroidal hydrogel particles at large scale. These toroidal hydrogel particles, compared to conventional spherical particles used in cell encapsulation, have several advantages such as shorter diffusion distance within, better deformability and larger surface/volume ratio. Secondly, I developed a robust hydrogel-based, nanofiber-enabled encapsulation device (NEED). This cell encapsulation device retained the properties of both the hydrogel (e.g. the biocompatibility) and the nanofibers (e.g. the mechanical robustness). The facile mass transfer was confirmed by encapsulation and culture of different types of cells. Additional compartmentalization of the devices enabled paracrine cell co-culture in single implantable devices. Lastly, I engineered a retrievable and scalable device termed as TRAFFIC (thread-reinforced alginate fiber for islets encapsulation). The mechanical

property of the device, critical for handling and retrieval, was much more robust than the neat alginate fibers due to the reinforcement of the central thread. I demonstrated the therapeutic potential of the device through the correction of chemically induced diabetes in C57BL/6 mice using rat islets for 3 months as well as immunodeficient SCID-Beige mice using human islets for 4 months. I further showed the scalability and retrievability in dogs.

CHAPTER 2: DEVELOPING MICROENCAPSULATION SYSTEM WITH SHAPED PARTICLES

2.1 Introduction

Hydrogel-based microcapsules, due to their large surface to volume ratio, is considered advantageous from a mass transport perspective. This microencapsulation system has been studied for many years and hundreds of publications with multiple successes having been produced in various animal models⁷⁴. Fibrotic overgrowth is one of the most significant challenges limiting the further clinical application of the hydrogel microcapsules⁸⁰. Standard alginate microcapsules are 500-1000 microns in diameter²⁸. However, recent studies have shown that increasing the size of intraperitoneally implanted alginate capsules from $\sim 500 \mu\text{m}$ to $\sim 1.5 \text{ mm}$ reduced fibrosis⁴⁴. Unfortunately, for the large, spherical particles, mass transfer becomes a problem (e.g., the cells in the center of the spheres can experience a lack of nutrients and oxygen).

Herein, I proposed an alternative way to increase the overall size of the capsules and increase the surface to volume ratio at the same time, which is to break the geometry topologically. A torus is a surface of revolution made by revolving a small circle, diameter d , about an axis. The center of the small circle is displaced by $D/2 > d/2$ from the axis. By this construction, the torus is the Cartesian product of two circles of radius d and D (Figure 2.1). The solid whose surface is the torus is called a toroid. Advantages of toroidal over spherical geometry derived from surface area to volume ratios (Figure 2.1). For the toroid, the surface area to volume ratio depends only on the small diameter d . Hence, surface area for mass transfer can be controlled independently of the toroid

size D . Furthermore, for the same volume, the toroid has greater surface area provided $d/D < 2/3$ (i.e. $4/d > 6/D$). In this case, the surface area advantage of a donut translates into a mass transfer advantage has been shown in the context of cell microencapsulation³³.

A vortex ring is a torus shaped, fluidic region where the fluid spins around an imaginary axis line, and vortex rings exist almost ubiquitously in nature and have stimulated numerous studies for decades⁸¹⁻⁸⁴. One simple way to generate a vortex ring is to have a droplet impacting the surface of a miscible liquid. When hitting the surface, the nearly spherical droplet deforms; during this deformation, many fluid intermediates with various intriguing, non-spherical shapes appear, including those resembling teardrops, jellyfishes, caps and donuts.

However, vortex rings rapidly evolve and are often short-lived⁸⁵, making it almost impossible to harvest and utilize them as materials. I hypothesized that if a proper “freezing event” exists, it will be possible to fix the unstable liquid vortex rings into stable hydrogel or solid microparticles of a defined shape. Through a fine-tuned gelation or precipitation process, I showed that I could freeze vortex rings using various materials such as nanoclay, alginate, chitosan and nanosilica. I termed these uniform and sometimes unprecedented shaped particles *vortex ring-derived particles* (VRP).

Among the different shapes of the microVRP, the donut (or toroidal) one is of special interests in the cell encapsulation field. Compared to the conventional spherical shapes, donut ones have several prominent advantages including a higher surface to volume ratio, a shorter diffusion path within, and a better deformability. In this part, I demonstrated the several applications of these donut-microVRP including bio-

encapsulation, 3-D cell culture, and cell free protein production. In addition, I showed the successful fabrication of more complicated Janus and core-shell donut-microVRP by engineering the electrospray nozzle. The donut-microVRP can also be directionally and orderly organized in either linear or planer fashion by taking advantages of their unique geometry, paving the way for future assembly of more sophisticated hierarchical materials.

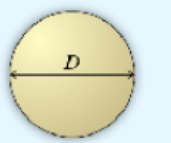
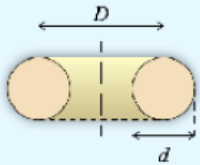
		Surface Area	Volume	Area/Volume
Sphere		πD^2	$\pi D^3/6$	$\frac{6}{D}$
Donut (Torus)		$\pi^2 Dd$	$\frac{\pi^2}{4} Dd^2$	$\frac{4}{d}$

Figure 2.1. A comparison of a sphere and a donut (torus).

2.2 Materials and Methods

2.2.1 Materials

All chemicals were used as received. Nanoclay powders (Laponite XLG) were received from Southern Clay Products, Inc. Sodium alginate (PRONOVA UP VLVG) was purchased from FMC Corporation. Colloidal silica (LUDOX TM HS-40), chitosan (low molecular weight), Sodium tripolyphosphate, CaCl₂, MgCl₂ and acetic acid were purchased from Sigma-Aldrich Co. LLC. NaH₂PO₄ was purchased from J.T. Baker, Inc.

2.2.2 Preparation of VRP and microVRP

For nanoclay hydrogel VRP, typically, a droplet of 2% (w/v) nanoclay solution was extruded from a syringe needle. The droplet fell from a certain height into a 100 mM CaCl₂ buffer. The viscosity of the nanoclay solution was tuned by changing the CaCl₂ concentration in the nanoclay solution. For nanoclay hydrogel donut-microVRP, a 2% (w/v) nanoclay solution was electrosprayed into the 100 mM CaCl₂ solution at a voltage of 7.3 kV with a pumping rate of 0.06 mL min⁻¹. The working distance between the nozzle and collecting buffer surface was fixed at 4 cm. For typical alginate hydrogel donut-microVRP, 2% (w/v) sodium alginate solution was electrosprayed into an aqueous buffer of 5 mM CaCl₂ and 95 mM MgCl₂ at 4.7 kV with a pumping rate of 0.06 mL min⁻¹. For typical chitosan hydrogel donut-microVRP, 0.5% (w/v) chitosan/acetic acid solution was electrosprayed into acetic acid buffer containing 13.6 mM sodium tripolyphosphate and 50 mM KH₂PO₄. Voltage was fixed at 4.8 kV and the pumping rate was 0.3 mL min⁻¹. For nanosilica donut-microVRP, silica nanocolloidal solution was directly electrosprayed into a 100 mM CaCl₂ aqueous buffer at 4.6 kV with a pumping rate of 0.06 mL min⁻¹. Other microVRP shapes were obtained by tuning the

nanoclay/alginate/chitosan/silica nanocolloidal solution viscosity or electrospaying voltage.

2.2.3 Characterizations

The samples were characterized by different analytical techniques. Scanning electron microscopy (SEM) and energy dispersive spectrometer (EDS) element mapping were performed by using a field emission scanning electron micro-analyzer (LEO 1550). Optical and fluorescent microscopic images were observed by a digital inverted microscope (EVOS fl). Confocal laser scanning microscopy (CLSM) images were taken by confocal laser scanning microscope (ZEISS LSM710). High speed camera images were captured by a high-speed camera (RedLake HG-XL, Integrated Design Tools, Inc.).

2.2.4 Cell encapsulation

For cell encapsulation, MDA-MB-231 cells, isolated rat pancreatic islets or *E.coli* were collected by centrifugation, after removing the supernatant, cells or cell aggregates were re-suspended into a 2% sodium alginate solution. This cell/alginate solution was electrospayed into the 95 mM MgCl₂/ 5 mM CaCl₂ buffer. Then, the donut-microVRP were collected and washed by PBS for 3 times to remove excess crosslinking buffer and transferred into corresponding culture medium.

2.2.5 Cell-free production of model protein

In order to produce green fluorescent protein (GFP), 1.4 µg of expression plasmid (PIVEX 2.4 containing GFP (5PRIME)) was added to a solution containing 5 mg of nanoclay hydrogel donut-microVRP, 37.8 µl of cell-free lysate, and 15 µl of nuclease free water. Samples were then placed in a BioTek fluorescent plate reader and

measured every 30 minutes with an excitation of 488 nm and an emission of 509 nm. In order to determine the effect of nanoclay hydrogel donut-microVRP on protein expression, samples were done in triplicate and side by side with control samples. All samples were then imaged at the 24-hour time point.

2.3 Results and Discussions

2.3.1 Fabrication of VRP by freezing vortex rings

A simple way to form a vortex ring is to drop a droplet into a miscible liquid. In a typical process, when a droplet hits the free surface of a miscible liquid at a sufficient impact speed, the droplet starts to deform in order to dissipate the energy by curling back (see Figure 2.2a for the time sequence). As the edge continues to curl, the center of the droplet becomes thinner and thinner. Eventually, when the center is too thin to withstand the surface tension, it breaks and a donut-shape is formed (Figure 2.2b).

To more precisely visualize the vortex ring formation and investigate whether it is possible to utilize this process to fabricate novel particles, we need a material that allows controllable “freezing” of the vortex ring. We discover that a nanoclay system is ideal here because of its unique, controllable gelation properties. The nanoclay (Laponite XLG) possess a disk-like structure with a non-homogeneous charge distribution: negative charges on the disk surface and positive charges on the rim⁸⁶. This special structure endows nanoclay with unique properties: in deionized water, the nanoclay disks are homogeneously distributed; whereas, in the presence of certain ionic species, the nanoclay disks pack together to generate a “house-of-cards” structure, forming a hydrogel⁸⁷ (Figure 2.3a). Importantly, the viscosity (~1.7 cP) and surface tension (~72 mN·m⁻¹) of the nanoclay solution are well suited for the formation of

vortex rings within the crosslinking buffer, since the gelation speed can be precisely controlled. We used a high-speed camera to capture a series of images of vortex rings formed by a drop of nanoclay solution impacting an aqueous bath, with or without gelation reaction (Figure 2.2c). In the case of no gelation (i.e. in a deionized water), the droplet moves along while spreading out with the front edges curling back. The shape of the droplet is constantly changing, experiencing in order: a teardrop-, jellyfish-, cap- and donut-shape. This whole process lasted for a mere 100 milliseconds, and the nanoclay solution finally dispersed homogeneously (see the upper row of Figure 2.2c). In contrast, in the presence of gelation (i.e., in a 100 mM CaCl₂ solution), the vortex ring maintains its shape (i.e. formed a VRP) starting from 36 milliseconds (see the bottom row of Figure 2.2c). As a result, by tuning the viscosity and impact speed of the droplet, we successfully captured the intermediates and produced VRP with various intriguing shapes (Figure 2.4a, b). Some of these VRP may be difficult to fabricate using other traditional methods such as soft lithography^{88, 89}, microfluidics⁹⁰ or self-assembly⁹¹. The formation of each of the VRP was also captured *in situ* and in real time by high-speed camera images (Figure 2.5). Moreover, their unique shapes allow us to assemble the VRP in an ordered fashion, for example, into an orientated, close-packed monolayer via a strategy similar to a Langmuir-Blodgett deposition (Figure 2.4c).

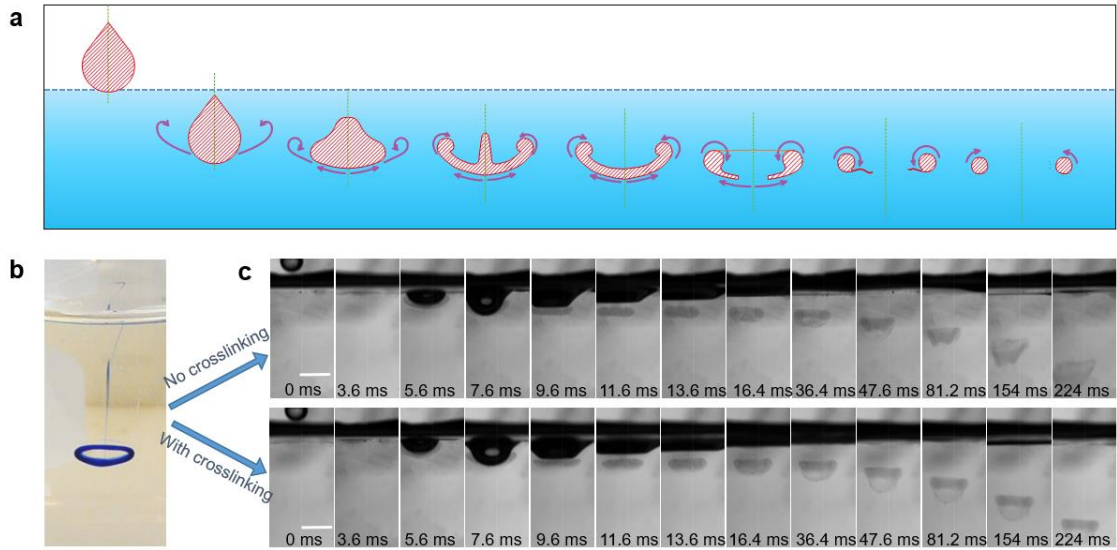


Figure 2.2. Vortex ring formation by droplet dripping. **a**, Schematic illustration of the vortex ring formation process (a water drop striking a water surface). **b**, Digital image of a vortex ring formed by dripping a drop of ink into a water pool. **c**, High-speed camera images of the vortex ring formation process by dripping a drop of nanoclay solution into a water pool (upper) and into a crosslinking buffer pool (lower). Scale bars, 3mm (**c**).

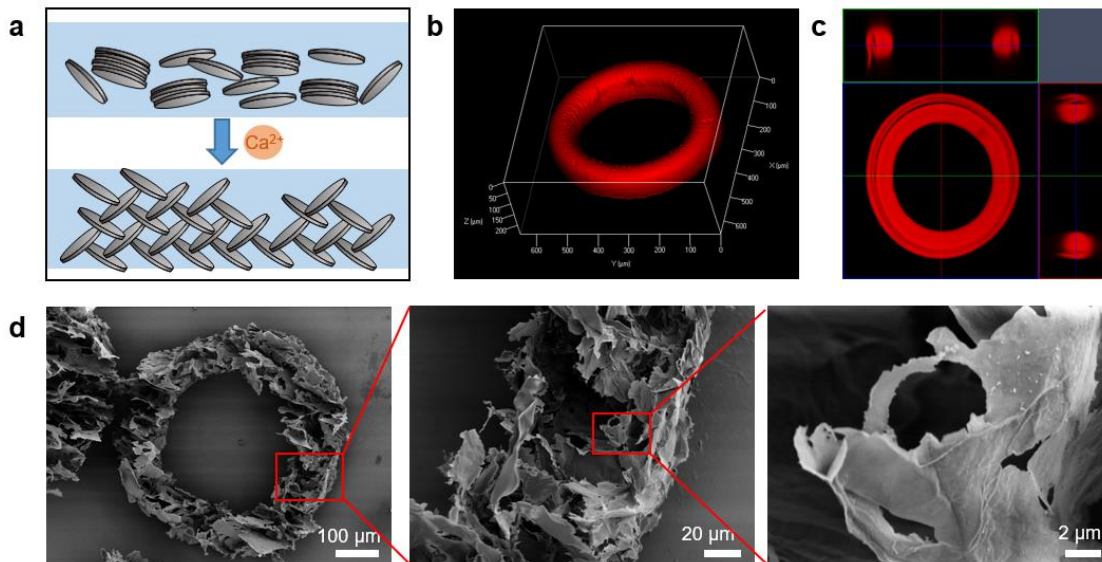


Figure 2.3. Characterizations of nanoclay hydrogel donut-microVRP. **a**, Schematic illustration of the gelation process of nanoclay hydrogel. **b**, **c**, Confocal microscope images of a nanoclay hydrogel donut-microVRP: 3-D reconstruction (**b**) and a cross-sectional image(**c**). **d**, SEM images of a freeze-dried nanoclay hydrogel donut-microVRP at different magnifications. Scale bars in (**d**) (from left to right): 100 μm , 20 μm , 2 μm .

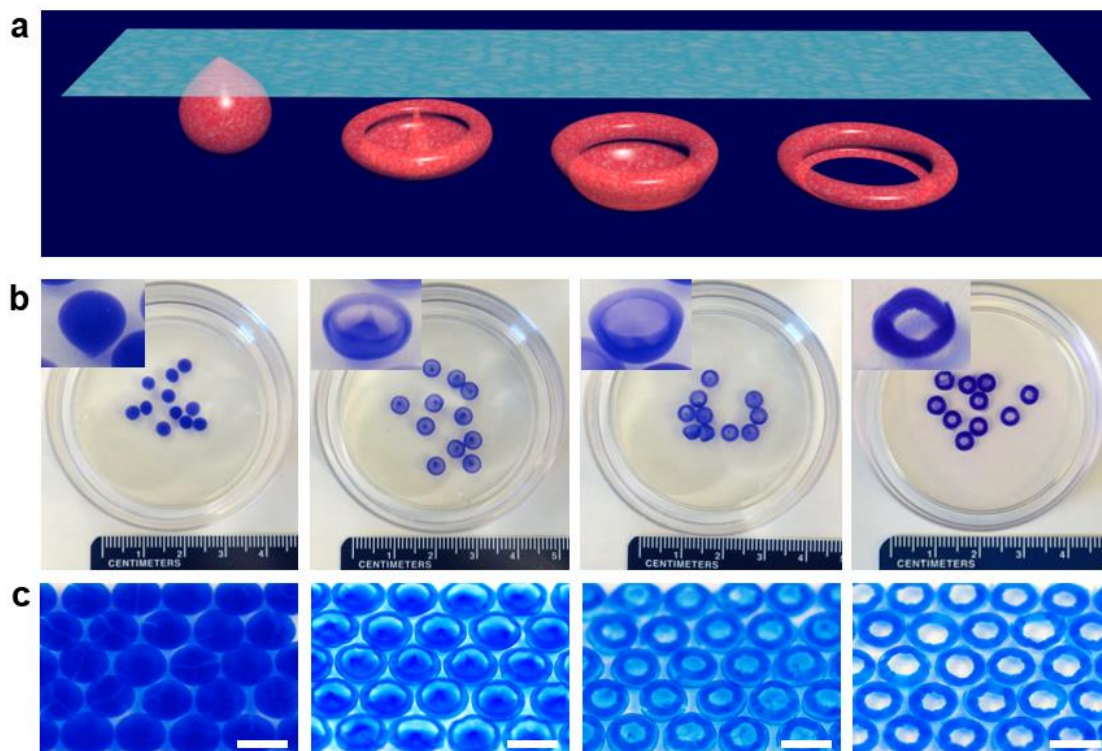


Figure 2.4. Nanoclay hydrogel VRP formed by free-fall dripping. **a-c**, Four typical VRP: teardrop-, jellyfish-, cap- and donut-ones. 3-D illustration (**a**), digital images (**b**) and close-packed monolayers (**c**). Scale bars, 6 mm (**f**).

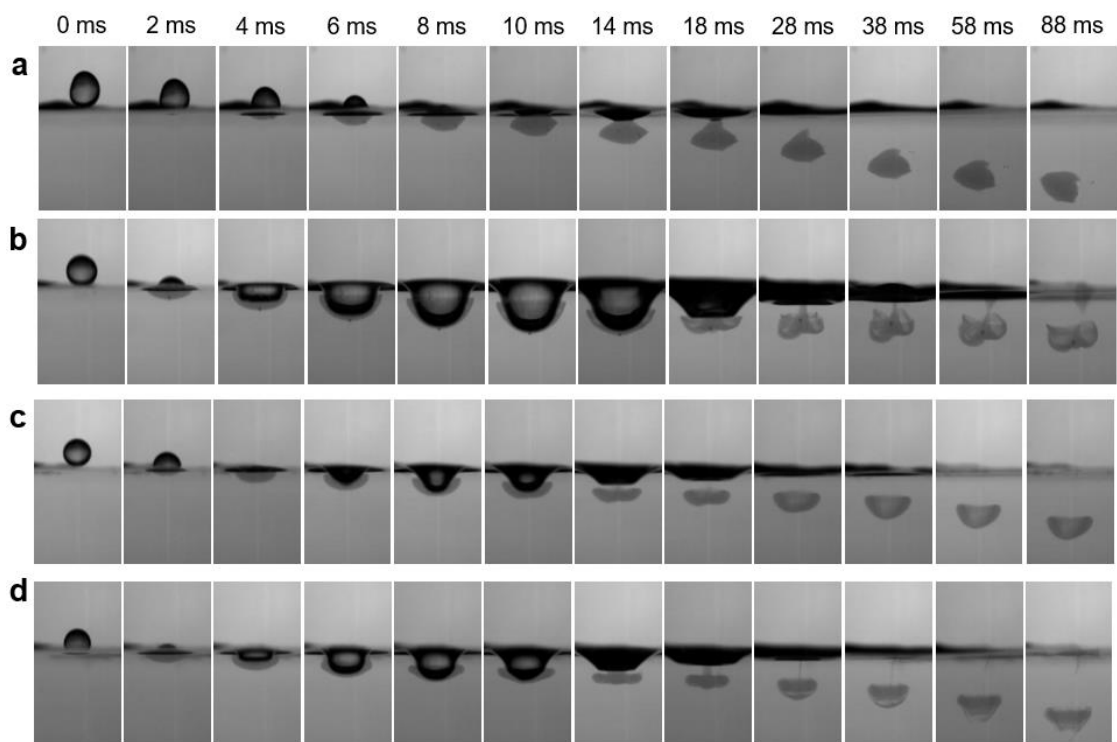


Figure 2.5. High speed camera images of the formation processes of the nanoclay hydrogel VRP. (a) teardrop- (b) jellyfish- (c) cap- and (d) donut-VRP.

2.3.2 Mass production of microVRP

The aforementioned simple dripping experiment proves the feasibility of freezing vortex rings at different stages to form various VRP. To reduce their dimensions and increase their production rate, we employ an industrially scalable electrospaying technique (Figure 2.6a). Briefly, by adding a high voltage electric field between the nozzle and the collector, the liquid jet is charged and breaks up into much smaller droplets⁹². Interestingly, the fluid dynamic behavior of smaller droplets impacting the crosslinking buffer remains similar to the “simple dripping” case. As a result, we easily fabricated nanoclay microVRP (e.g. with the donut shape) at a very high rate ($> 15,000$ VRP min^{-1}) (Figure 2.6b). Both the micro-scale torus shape and the nano-scale porous network structure of these donut-microVRP are characterized and confirmed (Figure 2.3b-d).

Importantly, we discovered that the size and shape of the electrospayed VRP can be well controlled. By simply tuning the voltage, the outer diameter of the donut-microVRP can be controlled, from around $280\ \mu\text{m}$ to over $1.5\ \text{mm}$ (Figure 2.6c). The microVRP dimensions are also controllable by tuning the working distance between the nozzle and the collecting buffer surface. Moreover, we can control the shapes of the microVRP by adjusting the viscosity of the nanoclay solution. Similar to the dripping method, we obtained, in addition to the donut-microVRP, three other types including teardrop-, jellyfish- and cap-shaped ones, all made with high uniformity and in mass numbers (Figure 2.7).

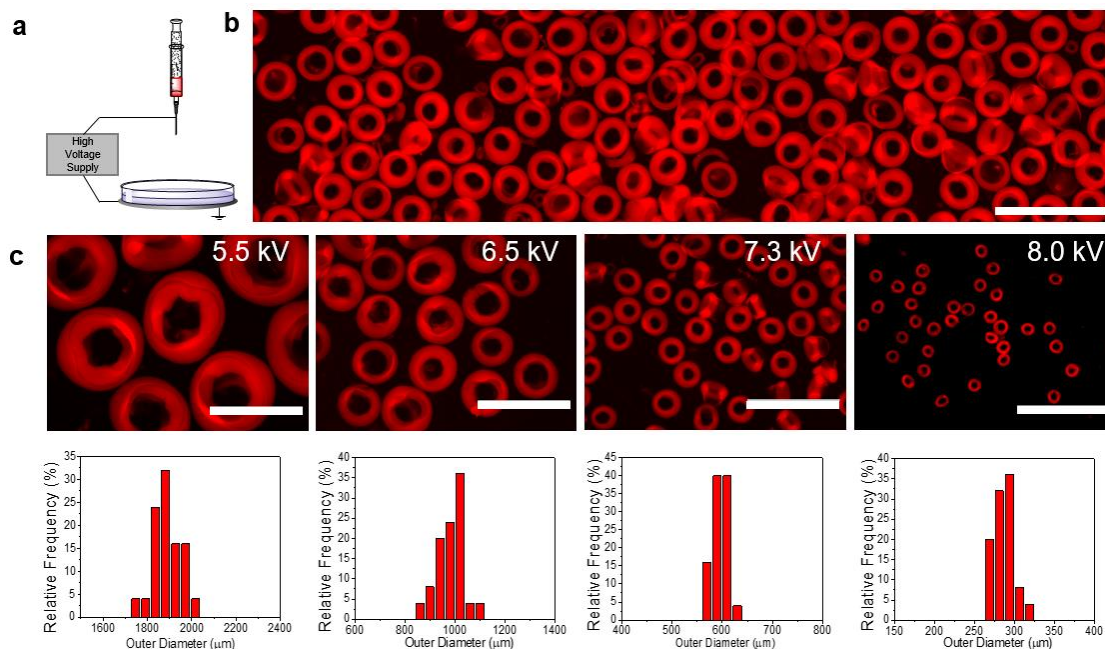


Figure 2.6. Mass production and size control of nanoclay hydrogel donut-microVRP. **a**, Schematic illustration of the electrospay setup. **b**, Microscopic fluorescent images of the nanoclay hydrogel donut-microVRP fabricated by electrospaying. For better visualization, a fluorescent dye Rhodamine B was mixed in the nanoclay solution. **c**, Size control of the nanoclay hydrogel donut-microVRP: microscopic images and corresponding size distribution plots. Scale bars, 2 mm (**b**); 1 mm (**c**).

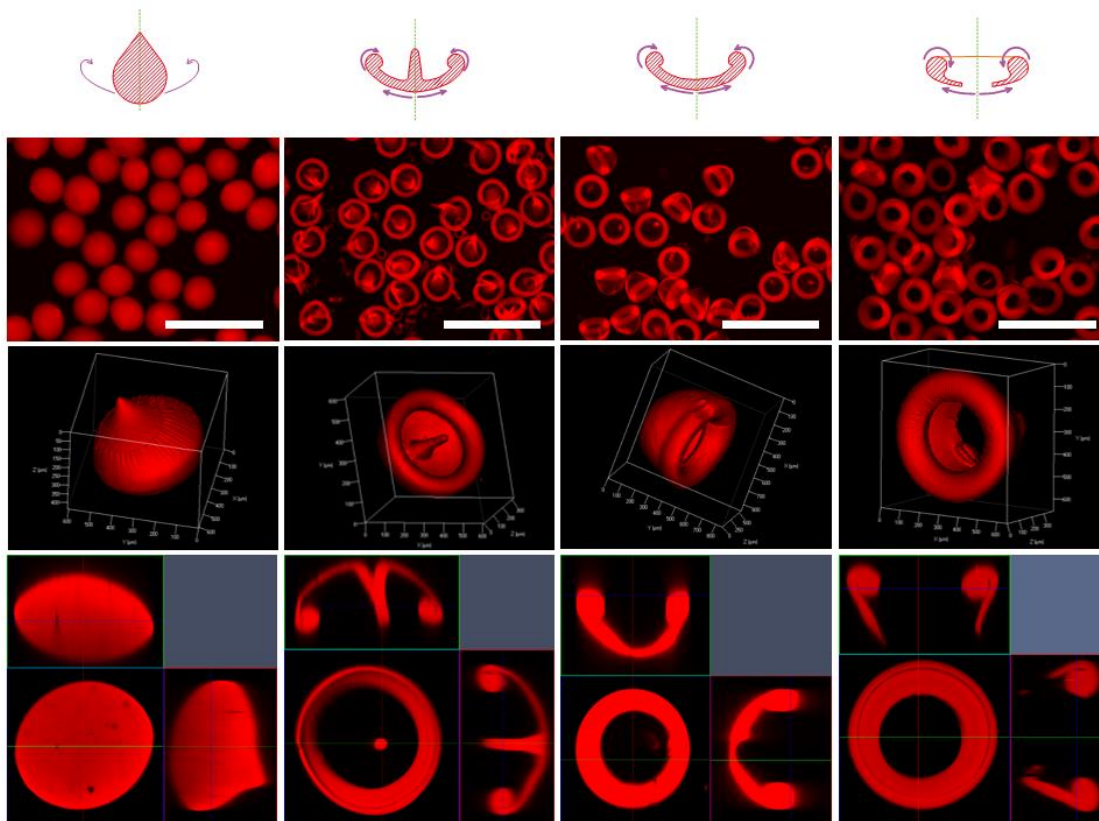


Figure 2.7. Shape control of the nanoclay hydrogel microVRP. (From top to bottom) schematic illustrations, microscopic images, 3-D confocal microscopic images and cross-sectional images. Scale bars: 1 mm.

2.3.3 Theoretical analyses and simulation

To better understand the control of size and shape of the nanoclay microVRP, we investigate theoretically how the size of the donut-microVRP or droplets is affected by the processing parameters in electro spraying such as the voltage. A classic scaling law which is valid for liquids with relatively low viscosities and electrical conductivities indicates the relationship between droplet size (D) and voltage (V)⁹²:

$$D \sim V^{-1/3} \quad (1)$$

This scaling law suggests that the droplet size will decrease as the voltage increases. As shown in Figure 2.8a, experimental data are plotted and fitted in this relationship assuming the droplet size is proportionally related to the VRP size. The fitting result indeed shows a linear relationship with a Coefficient of Determination $R^2 \approx 0.9816$.

Next, to understand the controllability of the VRP shape, we conducted a series of experiments and simulations to study how the properties of the drop before impact and after immersion dictated the development of vortex rings. On impact, drop deformation is resisted by interfacial tension while, after immersion, VRP formation depends on the rate of mixing by invasion of vorticity into vorticity-free regions relative to the rate of reaction. Pre-impact ballistics is controlled by Weber (We) and Ohnesorge (Oh) numbers while post-impact vortical invasion and reaction is controlled by Reynolds (Re) and Damköhler (Da) numbers^{93,94}, defined as

$$We \equiv \frac{\rho v^2 r}{\sigma} \quad (2)$$

$$Oh \equiv \frac{\mu}{\sqrt{\rho r \sigma}} \quad (3)$$

$$Re \equiv \frac{\rho a \gamma}{\mu} \quad (4)$$

$$Da \equiv \frac{kC}{\gamma} \quad (5)$$

where ρ is the drop's density, v is the impact velocity, r is the radius, μ is the dynamic viscosity, σ is the surface tension, k is the reaction rate constant, C is the concentration of binding sites, and $a\gamma$ is the rate of formation of interfacial area a between regions with and those without vorticity. Rate γ is estimated as a shear rate, from the simulation results. We and Oh numbers respectively characterize the strength of inertia and viscosity relative to surface tension of the impacting drops. Re and Da numbers respectively characterize rates of vorticity generation $a\gamma$ relative to resistance to invasion of vorticity by viscosity μ/ρ and rate of cross-linking kC relative to shear rate γ .

The results from all experiments and simulations are summarized in Figure 2.8b and Figure 2.9. According to our experimental and simulation results, with low- We , high- Oh and high- Da (i.e. reaction dominates mass transport), the droplet is “frozen” at the early stage of vortex ring development and forms a teardrop-VRP. While increasing We or decreasing Oh in the intermediate Da range (i.e. reaction and mass transport are commensurate), cap- or jellyfish-VRP are obtained. Further increasing We created rotating vortices that punctures the cap's central part to produce a donut-VRP. When the We is large (or Oh low) and the Da sufficiently low (i.e. mass transport dominates reaction), the particle cannot maintain its shape as a whole due to the reaction rate being much slower than the transport, the particle ends up fracturing. Normally, unconstrained liquid tori are very unstable and hence difficult to preserve. However, our method points out a simple approach of preserving any shape that a drop may form while impacting

the free surface of a crosslinking agent. We , Oh , Re and Da are the lumped control parameters of solution properties and process. Our work suggests that, regardless what materials are used, an appropriate prescription of the four dimensionless numbers in principle will allow us to obtain a continuously deformed family of all the shapes spanning the developing process of a vortex ring.

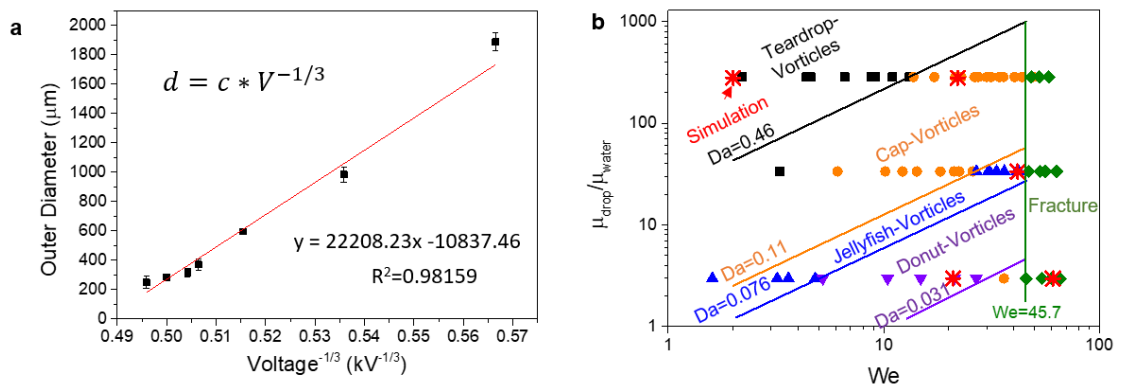


Figure 2.8. Mechanistic study of the VRP formation process. **a**, MicroVRP sizes controlled by tuning voltage. Error bars in **(a)** represent one standard deviation of the data away from the mean. **b**, Experimental results and theoretical analysis of the VRP shapes for different parameters.

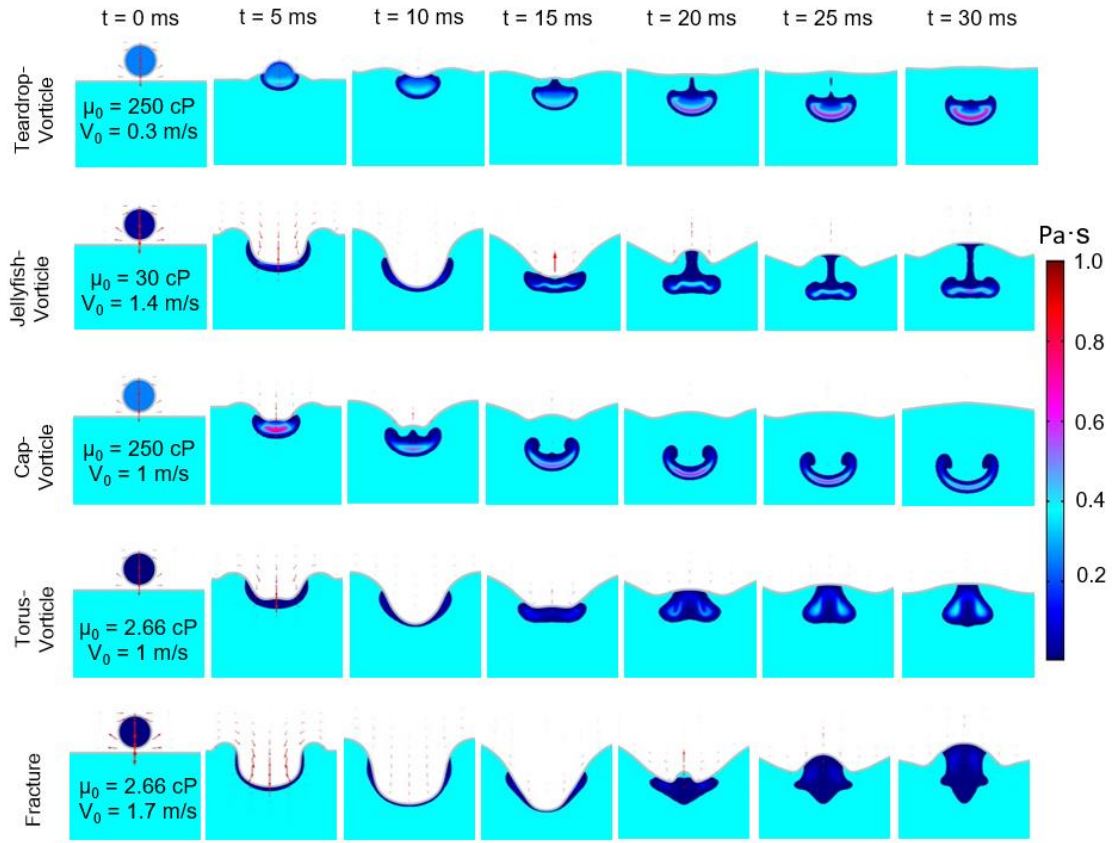


Figure 2.9. The axisymmetric simulation results of the vortex ring formation over time for five situations. The light blue is the crosslinking bath and the droplet above is the nanoclay solution where the color represents the viscosity difference. The nanoclay solution is only plotted where there is at least 0.2 wt% nanoclay particles and the grey line at the air/solution interface represents where there is equal air-water volume fraction.

2.3.4 MicroVRP formed with other materials and reactions

Our modeling and simulation suggests that microVRP can be fabricated from other materials as long as the deformation and “freezing” of vortex rings can both be controlled. To experimentally test this conclusion, we first chose two popular, crosslinkable biopolymers, alginate and chitosan. These two materials have been processed into hydrogel particles via electrospraying and they have been extensively used for drug and cell deliveries⁹¹. However, as in almost all previous studies, electrosprayed hydrogel microparticles have been spherical^{95, 96}. This is as expected according to our mechanistic studies due to the fact that their gelation reactions are relatively fast and that there is no time for the droplets to evolve into vortex rings. For instance, alginate droplet stops changing shape 20 milliseconds after impacting a conventional crosslinking buffer (Figure 2.10). Decreasing the crosslinking buffer concentration may slow down the gelation, but the low concentration ion buffers cannot completely crosslink the hydrogel, resulting in fractures (Table 2.1, Table 2.2,).

Here, in order to control the freezing event, we developed a novel ion-competing crosslinking solution containing a primary crosslinking agent (calcium ions for alginate or tripolyphosphate for chitosan) and a competing agent (magnesium ions or dihydrogen phosphate ions). Since the competing agent has a strong resemblance to the primary one but a much weaker crosslinking ability, when the droplet enters the ion-competing crosslinking solution, the competing agent competes with the primary one and hence slows down the reaction (Figure 2.11a, c). Indeed, using the ion-competing crosslinking solutions we successfully created microVRP from both alginate (Figure 2.11b) and chitosan (Figure 2.11d).

More interestingly, we can fabricate microVRP from inorganic colloidal nanoparticles as well. Silica nanocolloidal solution (ca. 50 nm in diameter) is initially stabilized in sodium chloride buffer. When the ionic strength is changed, the electrostatic homeostasis among the silica nanoparticles is broken, causing the nanoparticles to aggregate and precipitate (Figure 2.12a). This precipitation event is akin to the gelation event. As a result, by electrospraying the silica nanocolloidal solution into an ionic buffer, we also achieved mass production of uniform nanosilica jellyfish-, cap- and donut-microVRP (Figure 2.12b). These microVRP have excellent stability and rigidity; they remain almost intact after air-drying (Figure 2.12c).

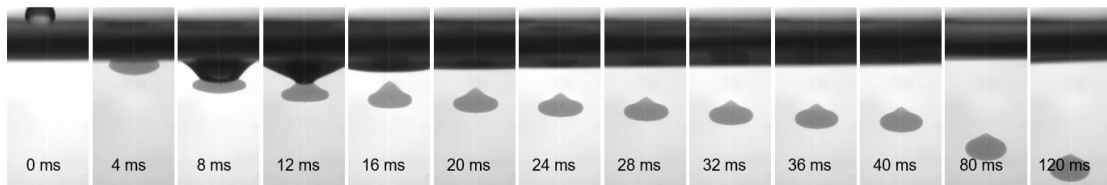


Figure 2.10. High speed camera images of an alginate solution impacting the conventional crosslinking buffer (100 mM CaCl_2 solution).

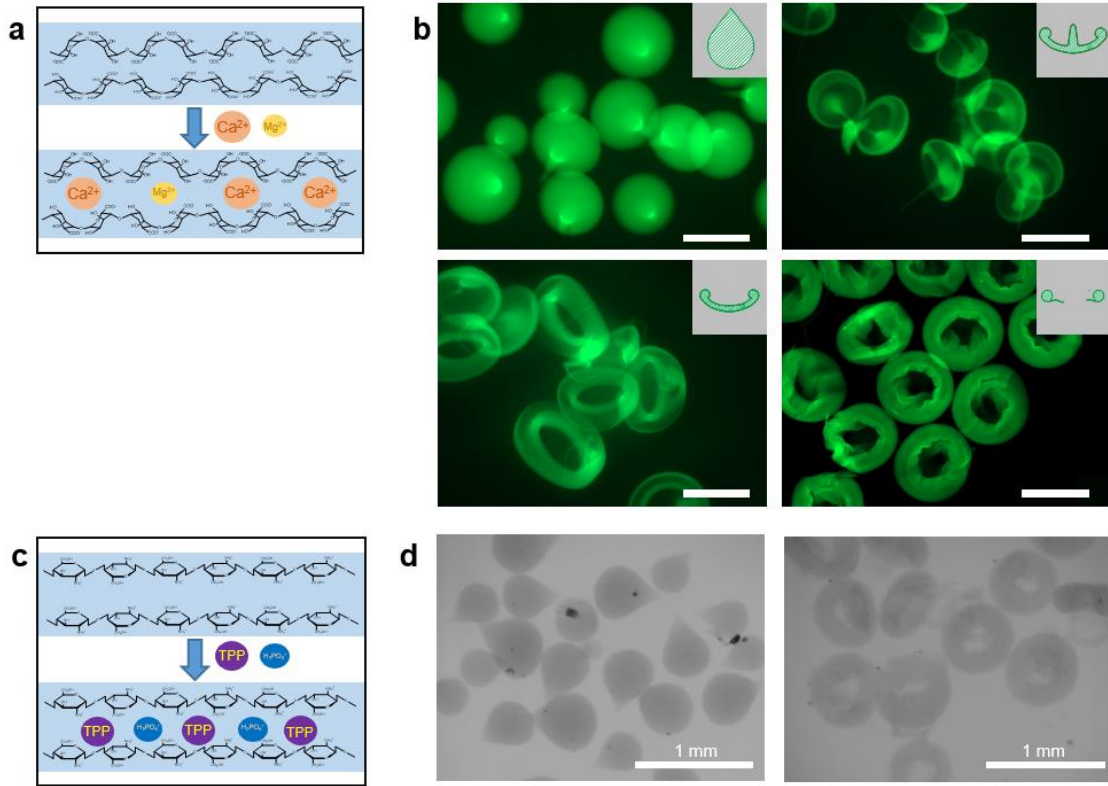


Figure 2.11. MicroVRP fabricated from alginate and chitosan hydrogel. **a**, Scheme of the modified gelation process in the ion-competing crosslinking buffer for alginate. **b**, Alginate hydrogel microVRP, alginate labeled with Alexa Fluor® 488 dye. **c**, Scheme of the modified gelation process for chitosan with the ion-competing crosslinking buffer. **d**, Chitosan hydrogel microVRP. Scale bars, 500 μm (**b**); 1 mm (**d**)

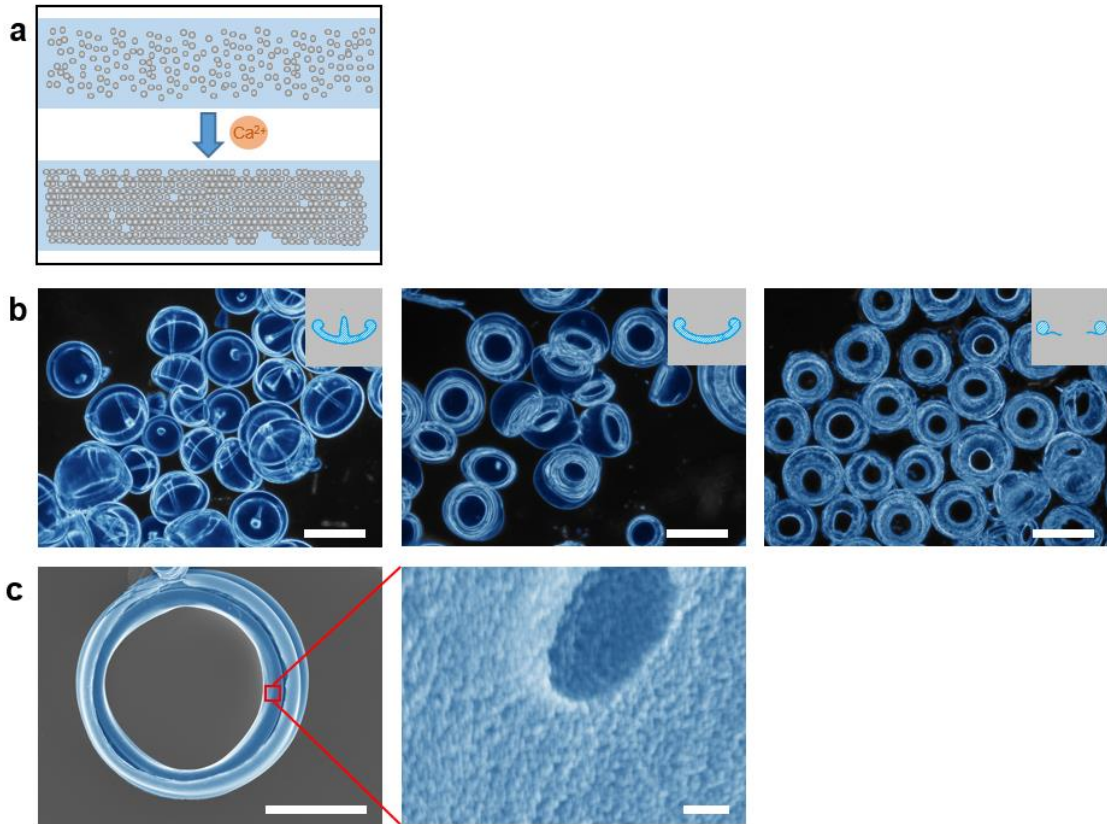


Figure 2.12. MicroVRP fabricated from nanosilica. **a**, Scheme of the silica nanocolloidal precipitation process. **b**, Microscopic images of the nanosilica microVRP (false-colored). **c**, SEM images of a dried nanosilica donut-microVRP (false-colored). Scale bars, 500 μm (**b**); 60 μm (**c** left panel); 100 nm (**c** right panel).

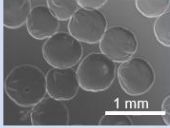
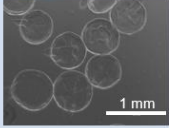
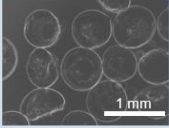
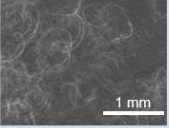
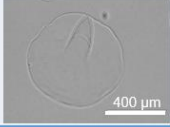
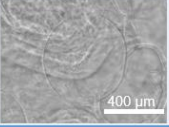
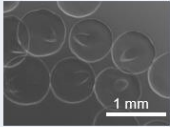
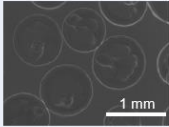
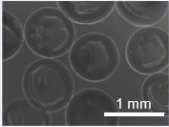
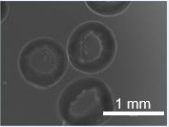
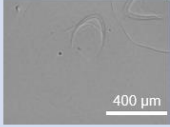
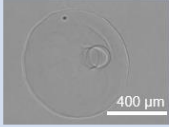
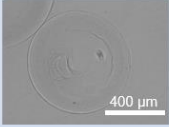
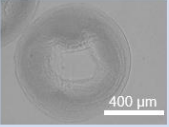
Concentration (mM)	CaCl ₂ (50)	CaCl ₂ (20)	CaCl ₂ (10)	CaCl ₂ (5)
2% VLVG 4.7 kV 0.6 mL/min				
				
Concentration (mM)	CaCl ₂ (50)/MgCl ₂ (100)	CaCl ₂ (20)/MgCl ₂ (100)	CaCl ₂ (10)/MgCl ₂ (100)	CaCl ₂ (5)/MgCl ₂ (100)
				
				

Table 2.1. Different shapes of the electrospayed alginate hydrogel microparticles using different crosslinking buffers.

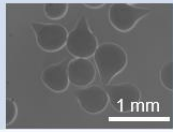
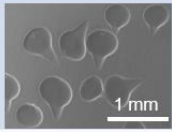
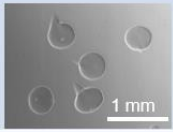
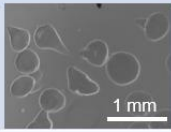
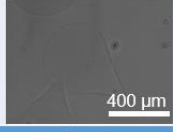
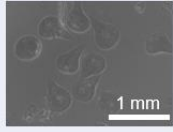
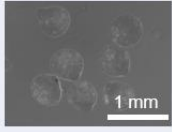
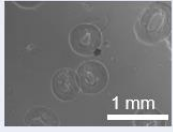
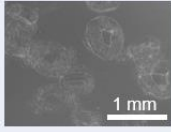
Concentration (mM)	tripolyphosphate(54)	tripolyphosphate(27)	tripolyphosphate(13.6)	tripolyphosphate(6.8)
0.5% Chitosan/acetic acid 4.8 kV 0.3 mL/min				
				
Concentration (mM)	TPP(54)/KH ₂ PO ₄ (50)	TPP(27)/KH ₂ PO ₄ (50)	TPP(13.6)/KH ₂ PO ₄ (50)	TPP(6.8)/KH ₂ PO ₄ (50)
				
				

Table 2.2. Different shapes of the electrospayed chitosan hydrogel microparticles using different crosslinking buffers.

2.3.5 Hydrogel donut-microVRP for bio-encapsulation

The fact that non-spherical, microVRP can be produced from a wide range of materials makes them not only fundamentally intriguing but also practically useful for real-world applications. For example, the donut-microVRP have several advantages over the spherical particles such as a larger surface area per volume, a shorter diffusion pathway within and sometimes a better deformability. These unique advantages combined with the tunable chemical composition make the donut-microVRP an interesting class of material for bio-encapsulation applications.

As a first proof-of-concept, we employed the nanoclay hydrogel donut-microVRP to encapsulate DNA molecules (Figure 2.13a) for improved cell-free protein production. Our previous work shows that the bulk nanoclay hydrogel protects DNA from DNase and hence enhance the cell-free protein production yield⁸⁷. Compared to bulk nanoclay hydrogel, the donut-microVRP have a much higher surface area for mass transfer and are therefore ideal for protein production applications. Here, using a green fluorescent protein (GFP) as a reporter, the nanoclay donut-microVRP-DNA group produces more than three times the amount of GFP than the conventional solution-phase system (SPS) (Figure 2.13b, c).

Next, we demonstrate efficient encapsulation of cells (both prokaryotes and eukaryotes) in hydrogel donut-microVRP. GFP-expressing *E.coli* cells were encapsulated in the nanoclay hydrogel donut-microVRP (Figure 2.14a). Additionally, we encapsulated mammalian cells or cell aggregates in alginate hydrogel donut-VRP (Figure 2.14b, c). Alginate hydrogel has been widely used for cell encapsulation for various applications such as type 1 diabetes treatment⁹⁷⁻⁹⁹. The hydrogel provides an

immuno-isolated environment for cells while allowing nutrients, oxygen and therapeutics to freely diffuse in and out. For decades, almost all previous works have used spherical alginate particles, typically with a diameter of 500-600 μm . However, recent studies have shown that it is actually more desirable to use larger size particles (about 1.5mm or larger in diameter) for cell delivery because these larger particles generate less foreign body responses upon implantation⁴⁴. Unfortunately, for the large, spherical particles, mass transfer becomes a real problem (e.g., the cells in the center of the spheres can experience the lack of nutrients and oxygen). The non-spherical, donut-VRP, on the other hand, are promising candidates to replace the spherical particles due to their larger surface area and shorter diffusion pathway within (i.e. decoupling of the overall dimension and the diffusion distance). To prove the concept, we encapsulated MDA-MB-231 cells, a human breast cancer cell line, in both alginate hydrogel spherical particles and donut-VRP. After four days of culture, the cells in the center of the spherical particles started to die, while the cells in the donut-VRP remained mostly alive (Figure 2.15). Encouraged by this result, we further demonstrate the feasibility of encapsulating rat pancreatic islets in the alginate hydrogel donut-VRP. The encapsulated islets again showed promising viability after 2 days *in vitro* culture (Figure 2.14c).

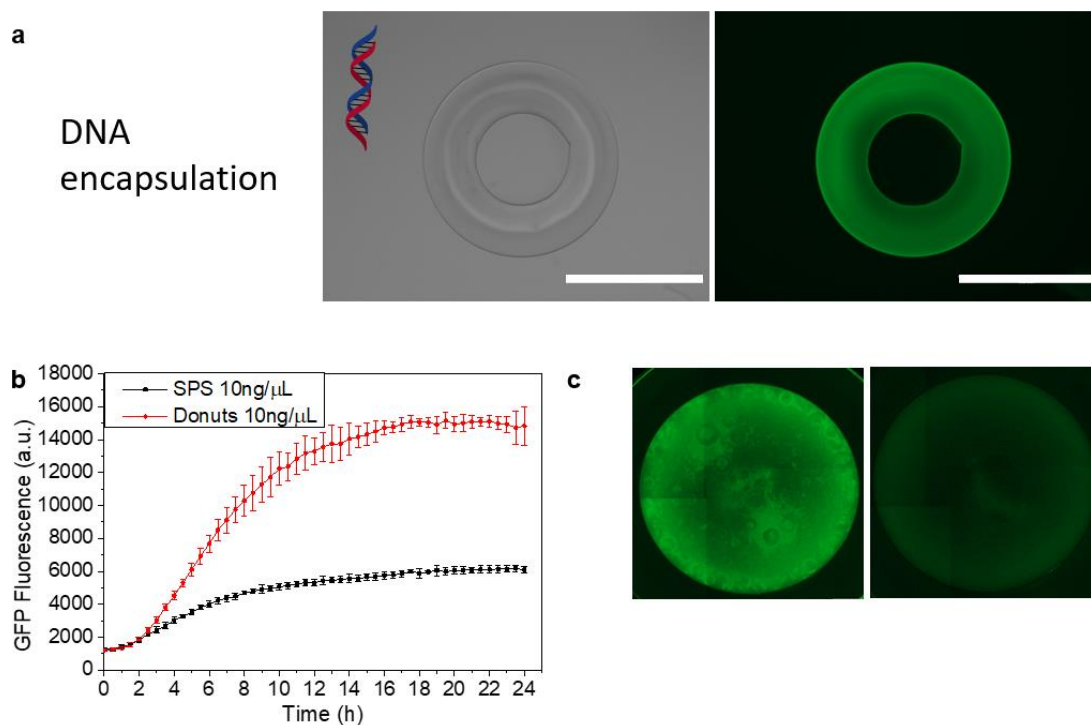


Figure 2.13. DNA encapsulation and cell-free production using nanoclay hydrogel donut micro-VRP **a**, A nanoclay hydrogel donut-microVRP encapsulating plasmid DNA: bright-field image and fluorescent image (stained with GelGreen™). **b**, Kinetic curve of the GFP fluorescence from cell-free protein production. Error bars in **(b)** represent one standard deviation of the data away from the mean. **c**, Fluorescent images of the reaction wells of cell-free protein production with (left) or without (right) nanoclay donut-microVRP. Scale bars, 400 μm .

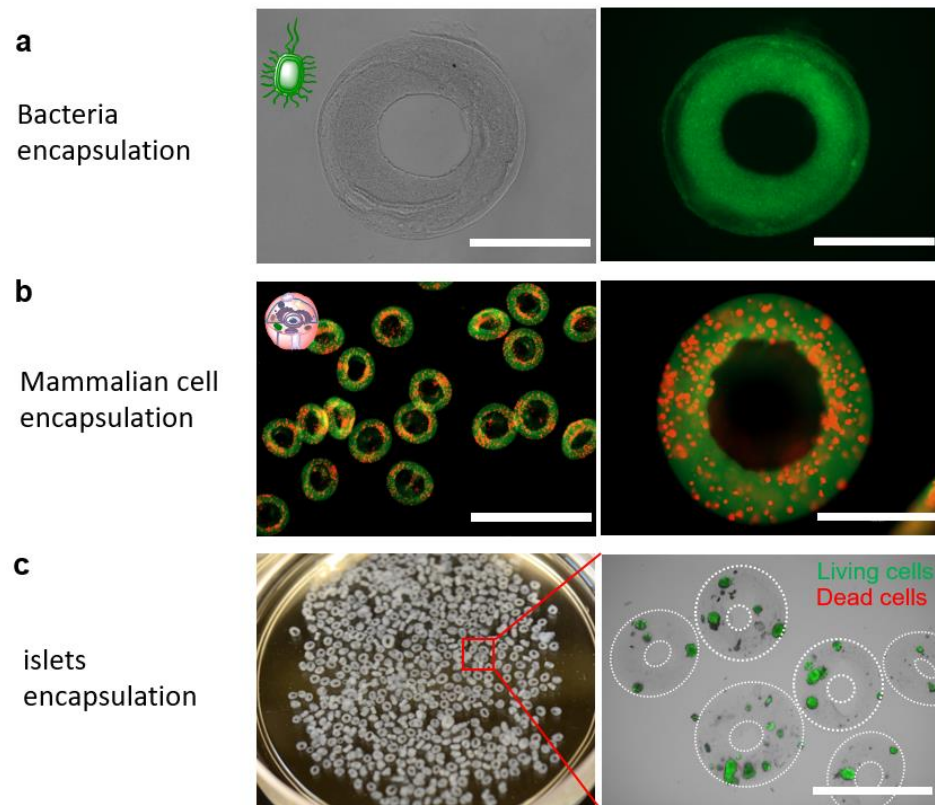


Figure 2.14. Cell encapsulation using donut-micro-VRP. **a**, A nanoclay hydrogel donut-microVRP encapsulating bacteria: bright-field image and fluorescent image (GFP expressing *E.coli*). **b**, Alginate hydrogel donut-microVRP encapsulating MDA-MB-231 cells that express Tomato red. **c**, Rat pancreatic islets encapsulated in the alginate donut-VRP. Scale bars, 400 μm (**a**, **b** right panel); 2 mm (**b** left panel, **c**)

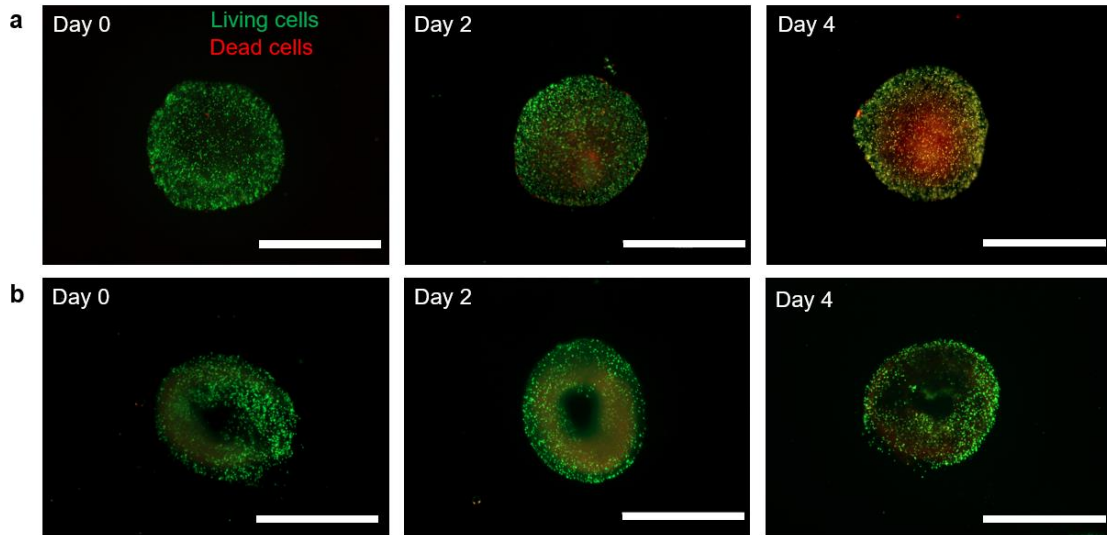


Figure 2.15. Mass transport property study. MDA-MB-231 cells were encapsulated in (a) a spherical alginate particle and (b) an alginate donut-VRP. Cells were stained with calcium-AM (green, live) and ethidium homodimer (red, dead).

2.3.6 Composite, compartmentalized or directionally assembled donut-microVRP

Composite materials often possess unique properties due to synergistic combination of the characteristics of the components. They have been widely used in applications such as catalysis, sensing, actuation, computation and communications¹⁰⁰. To further enhance and diversify the properties and functionalities of the donut-microVRP, we applied the approach of “freezing” to make VRP with even more complicated compositions and structures. First, we demonstrate two different kinds of donut-microVRP made from composite materials: nanoclay/nanosilica and nanoclay/alginate (Figure 2.16a). Addition of nanosilica or alginate improves the mechanical strength of the microVRP while maintaining the special characteristics of the nanoclay hydrogel such as enhancement of cell-free protein production. This combination can potentially make the nanoclay/nanosilica donut-microVRP applicable for packing a packed bed reactor for continuous cell-free protein production. In addition, we also doped other materials into the current donut-microVRP to introduce new properties. For examples, Fe₃O₄ nanoparticles were doped in the nanosilica or nanoclay matrix to prepare magnetic donut-microVRP (Figure 2.16b), which can be manipulated using an external magnetic field and potentially used as building blocks for novel stimuli-response materials¹⁰¹.

Next, by taking advantage of the unique donut-shape, we directionally assembled the donut-microVRP in either one or two dimensions into supra-structures. For 1-D assembly, we made use of the holes of the donut-microVRP. As shown in the scheme in Figure 2.16c, several Nylon short strings were fixed perpendicular to the air-solution interface. When the donut-microVRP formed, they were threaded into Nylon

strings and captured *in situ* into 1-D assemblies (Figure 2.16c). For 2-D assembly, we assembled the magnetic donut-microVRP into a close-packed monolayer with hexagonal packing symmetry by a combination of magnetic field and a monolayer assembly strategy similar to that used in making Langmuir-Blodgett films (Figure 2.16d).

Moreover, by engineering the nozzle used in electrospraying, we fabricated donut-microVRP with compartmentalized structures. As shown in Figure 2.15e, the Janus alginate hydrogel donut-microVRP are produced by using a side-by-side nozzle. Core-shell alginate hydrogel donut-microVRP are also successfully prepared by using a core-shell nozzle (Figure 2.16f). These bi-compartmental donut-microVRP may find a wide range of applications in biomedical applications, such as co-culture and co-delivery of different types of cells. Additionally, we show another example of magnetic field-assisted directional assembly of Janus donut-microVRP. Janus donut-microVRP with half nanosilica and half nanosilica/Fe₃O₄ nanoparticles are prepared using a side-by-side nozzle. They are aligned under an external magnetic field. Due to their asymmetric magnetic property, all the donut-microVRP are oriented in the same direction with the magnetic field (Figure 2.16g).

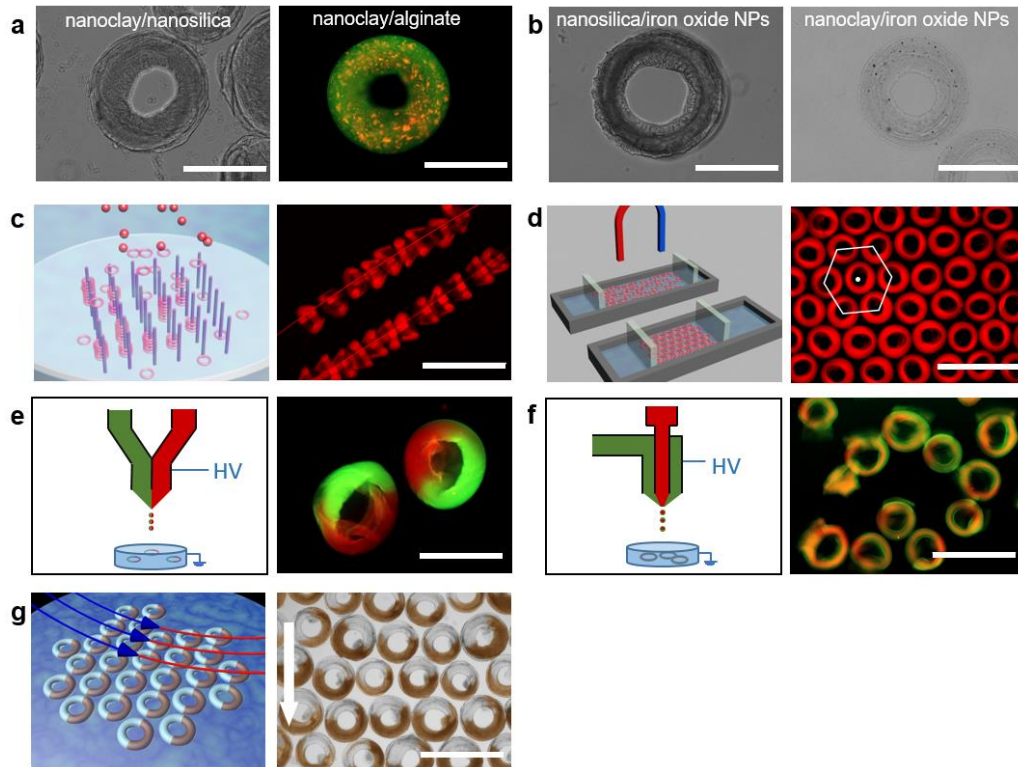


Figure 2.16. Composite and assembly of donut-microVRP. **a**, Donut-microVRP made from composite materials: nanoclay/nanosilica, nanoclay/alginate. **b**, Magnetic donut-microVRP: nanosilica/ Fe_3O_4 nanoparticles and nanoclay/ Fe_3O_4 nanoparticles. **c**, Schematic illustration of the assembly process and a microscopic image of the 1-D structure made from nanoclay hydrogel donut-microVRP. **d**, Schematic illustration of the assembly process and a microscopic image of the 2-D structure made from magnetic nanoclay hydrogel donut-microVRP. **e**, Schematic illustration of the nozzle design and a microscopic image of the Janus donut-microVRP. **f**, Schematic illustration of the nozzle design and a microscopic image of the core-shell donut-microVRP. **g**, Directional assembly of the Janus magnetic nanosilica donut-microVRP; the arrow indicating the direction of the magnetic field. Scale bars, 400 μm (**a**, **b**); 2 mm (**c**, **d**, **f**); 1 mm (**e**, **g**).

2.4 Conclusion

Compared with spherical particles, non-spherical particles have received much less attention in the materials community. However, non-spherical particles such as the donut-shaped ones are often advantageous due to their larger surface areas and shorter diffusion distances. Therefore, mass production of non-spherical particles with controlled dimensions and geometries from different materials will have important implications in fields ranging from catalysis to therapeutic delivery. Here, we report, for the first time, the creation of a new class of non-spherical particles, vortex ring-derived particles. By combining the ubiquitous vortex ring phenomenon with rationally designed freezing events, we develop a universal, robust and scalable method to produce uniform VRP from a variety of materials. Mechanistic studies reveal two critical timescales that determined the VRP shape: the timescale of the vortex ring development and the timescale of the gelation or precipitation process. In order for the VRP to form, the solution properties and process parameters must be well tuned such that the fast evolving vortex rings can be frozen at different stages. Among the various VRP, the donut-VRP are of particular interest and their diverse applications in bio-encapsulation and cell-free protein production are demonstrated. Further engineering of donut-VRP to include compartmentalization and directional assembling are all achieved, creating opportunities to design and engineer VRP-based novel materials that have not been attainable using conventional methods.

CHAPTER 3: DEVELOPING ROBUST, HYDROGEL-BASED, NANOFIBER-ENABLED ENCAPSULATION DEVICES FOR CELL THERAPIES

3.1 Introduction

Even though microcapsules are easy to implant and have large surface areas for mass transfer, and tremendous promising results have been reported. One concern is that after these microcapsules are implanted, often in the peritoneal cavity in large numbers (~100,000 for a human)^{52, 102}, it is difficult or nearly impossible to completely retrieve or replace them in the event of transplant failure or medical complication^{4, 52, 103}. In addition, it is challenging to control the locations of the cells within the microcapsules, leading to incomplete encapsulation and inadequate immunoprotection. Lastly, the microcapsules sometimes tend to clump over time in the body, deteriorating the mass transfer³⁷.

To this end, macroscopic hydrogel devices such as long fibers¹⁰⁴ and thin sheets¹⁰⁵ have recently been proposed as alternative formats for cell encapsulations. However, the intrinsic softness of hydrogels due to the large water content (>95%) and the high aspect ratios of these macrodevices make the mechanical durability a potential concern for long-term clinical uses. In fact, most hydrogels that are suitable for cellular engineering applications^{106, 107} (i.e. with large water contents and high diffusion rates) tend to have relatively low mechanical strength, as compared to typical plastics or rubbers^{108, 109}. Robust mechanical properties are particularly desirable for cell encapsulation because the devices are intended for long-term use in the body. Numerous approaches have been reported to improve the mechanical properties of hydrogels, most

commonly through increase of crosslinking densities¹¹⁰ or incorporation of additional chemically crosslinked networks^{109, 111, 112}.

Here, we report a physical approach to fabricate robust hydrogel-based, *nanofiber-enabled encapsulation devices* (or NEEDs) for cell encapsulation. To make the NEEDs, we make use of the capillary-driven wicking phenomenon and infiltrate the nanofibrous walls of pre-made electrospun tubes or chambers with hydrogel precursor solutions. The precursors are held in place by the capillary force and the NEEDs, either tubular or planer, are obtained by a subsequent hydrogel crosslinking. This approach is simple, broadly applicable and does not alter the water content or the intrinsic chemistry of the hydrogels.

The NEED design takes advantages of the mechanical strength and the unique, fine pore structures of the electrospun nanofiber membranes. Electrospun nanofibers are a versatile class of material that have various attractive properties for use as biomaterials^{113, 114} such as small fiber size (~ 10 nm – 10 μ m), high porosity ($>90\%$), large surface area (~ 10 m²/g), and interconnected pore structures (~ 1 μ m). Depending on the chemical compositions, they also have tunable material properties including mechanical strength, biodegradability and wettability¹¹³⁻¹¹⁵. It has been shown that by controlling how they are collected during the electrospinning process it is possible to engineer the nanofibers into macroscopic devices such as microwell chips¹¹⁶ or microtubes^{117, 118}. Given these unique properties, electrospun nanofibers provide an enabling platform to engineer the next generation of hydrogel-based cell encapsulation devices.

The NEEDs have several advantages for cell encapsulation. First, the nanofiber

membranes as the scaffolds of the device walls provide the necessary mechanical strength and prevent any potential breakage or cell leakage while still allowing adequate mass transfer. Second, the hydrogel as the device exterior reinforced by the nanofibers through mechanical interlocking provide the necessary biocompatibility and immunoprotection. Third, the NEEDs can be pre-fabricated and the cells can be loaded in a custom designed fashion, for example, by dispersing the cells in physiologically relevant extracellular matrices (ECM)¹¹⁹. This way, the device exterior hydrogel that interacts with the body when transplanted and the ECM hydrogel in the internal compartment that interacts with the cells can be decoupled and independently designed. Finally, multiple compartments can be engineered into a single NEED, which can then be used for complex cell encapsulation, co-culture and delivery.

In this work, we successfully fabricated the NEEDs with different hydrogel chemistries and compartmentalizations. Through tensile tests, we confirmed their robust mechanical properties. Using model cells, we demonstrated the facile mass transfer and flexible cell loading in single or multiple compartments with control over the cell-dispersing matrix. Lastly, we evaluated the potential application of the devices by encapsulating and delivering insulin-producing rat pancreatic islets into a chemically-induced diabetic mouse model. The diabetes was corrected for the duration of the experiment (8 weeks) right before the implants were retrieved. The retrieved devices showed minimal fibrosis according to histological studies and as expected, live and functional islets were observed within the devices. This work provides a proof of concept for the NEEDs as a new platform for potential cell encapsulation therapies.

3.2 Materials and Methods

3.2.1 Chemicals

Poly (caprolactam) (Nylon 6), polysulfone (PSU), polyacrylonitrile (PAN) and polycaprolactone (PCL) were purchased from Scientific Polymer Products, Inc. (Ontario, NY). Formic acid, N,N-Dimethylformamide (DMF), dichloromethane(DCM), N,N-Dmethylacetamide(DMAc), poly(ethylene glycol) diacrylate (PEG-DA), 2-hydroxy-2-methylpropiophenone, CaCl₂ and BaCl₂ were purchased from Sigma-Aldrich Co. (St. Louis, MO). Sodium alginate was purchased from FMC BioPolymer Co. (Philadelphia, PA). All reagents were purchased and used as received without further purification.

3.2.2 Animals

Immune-competent male C57BL/6 mice were obtained from Jackson Lab and Sprague-Dawley rats were obtained from Charles River Laboratories. All animal procedures were approved by the Cornell Institutional Animal Care and Use Committee.

3.2.3 Fabrication of electrospun nanofiber tubes or chambers

In a typical procedure for electrospinning, a solution of 20% (w/v) Nylon 6 in formic acid was used. The nanofibers were spun at 20 kV (Gamma High Voltage, Ormand Beach, FL) with a pumping rate of 0.001 mL/min (Harvard Apparatus, MA) and with a 16G 1” blunt needle as the spinneret. Working distance was fixed at 25 cm. A rotating target (i.e. aluminum rods with diameters ranging from 0.32 mm to 2.41 mm or aluminum plates with various dimensions) was placed in the path of the polymer solution jet. The rod was connected to an AV motor controlled by rheostat (VWR) and rotated at 400~500 rpm. After electrospinning process, the nanofibrous tubes or

chambers were removed from the template and cut into desired lengths, or placed in a hydrogel precursor solution to make NEEDs (see 2.4 below). For other polymer nanofibers, the solutions and electrospinning conditions are summarized in Table 1. To fabricate the multi-compartmental nanofiber tubes; firstly, nanofibers were collected on several rotating targets. Then, these collecting targets were bundled together and used to collect electrospun nanofibers again. When finished, nanofiber devices with multiple compartments were removed from the collecting target and cut into desired lengths.

3.2.4 Fabrication of NEEDs

The as-prepared electrospun nanofiber device (tubular or planar, in the presence of the template) was submerged in a 2% (w/v) solution of SLG20 alginate dissolved in 0.8% (w/v) NaCl solution. The whole setup was put in a vacuum chamber for degasing for 15 min to ensure the full impregnation of the alginate solution into the interstitial space of the nanofiber membrane. The alginate was then cross-linked by submerging the device into a BaCl₂/Mannitol/HEPES solution (BaCl₂: 20mM, D-Mannitol: 250mM, KCl: 2mM, HEPES: 10mM). The NEEDs were washed with 1X PBS for 3 times and were ready to use. Devices based on chitosan and collagen hydrogels were similarly prepared. The chitosan was crosslinked with a triphosphate solution and the collagen by neutralizing the pH and incubation at 37 °C. For PEG hydrogel device, a PEG precursor solution composed of 2-hydroxy-2-methylpropiophenone: PEG-diacrylate (PEG-DA): water (0.5:50:50 wt:wt:wt) was prepared first. Then a nanofiber tube was submerged in the PEG-DA solution and degased in a vacuum chamber for 15 min. The device with impregnated PEG precursor was put in the UV crosslinker (Spectronics, XL-1000) and exposed to UV radiation (325nm) for 300 mJ/cm².

3.2.5 Characterizations

The samples were characterized by different analytical techniques. Scanning electron microscopy (SEM) was performed by using a field emission scanning electron micro-analyzer (LEO 1550). Optical and fluorescent microscopic images were observed by a digital inverted microscope (EVOS fl). Conventional macro-tensile measurements were performed using a dynamic mechanical thermal analysis (DMA Q800). All samples were mounted between holders at a distance of ~1.5 cm. Tensile testing was conducted at a rate of 0.5 N/min at room temperature (23° C). Stress (MPa) and strain (%) were automatically calculated by the software.

3.2.6 Cell viability assay-MTT

Cell proliferation analysis was performed using a colorimetric methyl thiazolyl tetrazolium (MTT) assay. Cells were seeded in a 24-well plate at a density of 1×10^4 cells per well. Same amount of cells was encapsulated in NEEDs. When performing the assay, the medium was removed. Cells were washed 3 times with PBS (pH = 7.4) and then 5 mg/mL MTT was added to each well and incubated for 4h. The formazan product was dissolved in 200 μ L detergent reagent for 4h and the absorbance was read at 570nm with Absorbance Microplate Reader (BioTek Synergy 4).

3.2.7 Rat islet isolation and purification

Sprague-Dawley rats from Charles River Laboratories weighing approximately 300 grams were used for harvesting islets. All rats were anesthetized using 3% isoflurane in oxygen and maintained at the same rate throughout the procedure. Isolation surgeries were performed as described by Lacy and Kostianovsky¹²⁰. Briefly, the bile duct was cannulated and the pancreas was distended by an in vivo injection of

0.15% Liberase (Research Grade, Roche) in RPMI 1640 media solution. The pancreas was digested a 37 °C water bath for 30 minutes. The digestion was stopped by adding 10–15 mL of cold M199 media with 10% heat-inactivated fetal bovine serum and a slight shaking. Digested pancreases were washed twice in the same aforementioned M199 media, filtered through a 450 µm sieve, and then resuspended in a Histopaque 1077 (Sigma)/M199 media gradient and centrifuged at 1,700 RCF at 4 °C. Depending on the thickness of the islet layer that was formed within the gradient, this step was repeated for higher purity islets. Finally, the islets were collected from the gradient and further isolated by a series of gravity sedimentations, in which each supernatant was discarded after four minutes of settling. Purified islets were hand-counted by aliquot under a light microscope and then washed three times in sterile 1X phosphate-buffered saline. Islets were then washed once in RPMI 1640 media with 10% heat-inactivated fetal bovine serum and 1% penicillin/streptomycin, and cultured in this medium overnight for further use.

3.2.8 Islets encapsulation

Immediately prior to encapsulation, the cultured islets were centrifuged at 1400 rpm for 1 minute and washed with Ca-Free Krebs-Henseleit (KH) Buffer (4.7 mM KCl, 25 mM HEPES, 1.2 mM KH₂PO₄, 1.2 mM MgSO₄ × 7H₂O, 135 mM NaCl, pH ≈ 7.4, osmotic pressure ≈ 290 mOsm). After the wash, the islets were centrifuged again and all supernatant was aspirated. The islet pellet was then re-suspended in Matrigel (TM) (BD Biosciences) solution at desired islet number density. The islet suspended Matrigel (TM) solution was injected into NEEDs by using a precooled syringe, then the open end of the device was sealed by adding a small drop of Nylon 6/formic acid solution and

further coated with alginate hydrogel. Then the NEEDs were washed 4 times with HEPES buffer and 2 times with RPMI Medium 1640 and cultured overnight at 37 °C for transplantation. As the islets had variable sizes (50 – 400 µm) and the total number of encapsulated islets were converted into islet equivalences (IE, normalized to 150 µm size) based on a previously published method¹²¹.

3.2.9 Insulin secretion from encapsulated islets on glucose stimulation

Functional assessment of encapsulated islets was tested via static glucose-stimulated insulin secretion (GSIS) assay. The Krebs Ringer Bicarbonate (KRB) buffer (2.6 mmol/l CaCl₂/2H₂O, 1.2 mmol/l MgSO₄/7H₂O, 1.2 mmol/l KH₂PO₄, 4.9 mmol/l KCl, 98.5 mmol/l NaCl, and 25.9 mmol/l NaHCO₃ (all from Sigma-Aldrich, St. Louis, MO) supplemented with 20 mmol/l HEPES/Na-HEPES (Roche, Indianapolis, IN) and 0.1% BSA (Serological, Norcross, GA), was prepared beforehand. Islets encapsulated in NEEDs were incubated for 2h in KRB buffer at 37°C, 5% CO₂, and then incubated for 75 min with 2.8 mM or 16.7 mM glucose in the same conditions. Insulin concentration in the buffer solutions was determined by using ultrasensitive mouse/rat insulin ELISA kit (Crystal Chem) per supplier's protocols. Briefly, 5µl of the sample (or mouse insulin standard) together with 95µl diluent buffer was put into the wells of insulin-capture-antibody pre-coated plates, and incubated for 2 hours at 4°C. After a thorough wash, 100µl of anti-insulin enzyme conjugate was applied to each well for a 40-minute incubation. Then 100µl of enzyme substrate solution per well was added into the washed plate to develop an optimal blue color. Absorbance of reaction solution at 450 nm was measured in the Synergy plate reader (Biotek). Data were plotted against the standard curve of serial dilutions of insulin.

3.2.10 Transplantation

Immuno-competent male C57BL/6 mice were utilized for transplantation. To create insulin-dependent diabetic mice, healthy C57BL/6 mice were treated (50 mg/kg mouse) with freshly prepared Streptozocin (STZ) (Sigma-Aldrich) solution (7.5 mg/ml in sodium citrate buffer solution) for 5 consecutive days. The blood glucose levels of all the mice were retested prior to transplantation. Only mice whose non-fasted blood glucose levels were above 300 mg/dL were considered diabetic and underwent transplantation. The mice were anesthetized using 3% isoflurane in oxygen and maintained at the same rate throughout the procedure. Preoperatively, all mice received 0.3 mL of 0.9% saline subcutaneously to prevent dehydration. The abdomens of the mice were shaved and alternately scrubbed with betadine and isopropyl alcohol to create a sterile field before being transferred to the surgical field. A ~1 mm incision was made along the midline of the abdomen and the peritoneum was exposed using blunt dissection. The peritoneum was then grasped with forceps and a ~1 mm incision was made. The device was then inserted into the peritoneal cavity through the incision. The incision was closed using 5-0 taper tipped polydioxanone (PDS II) absorbable sutures. The skin was then closed over the incision using a wound clip.

3.2.11 Blood glucose monitoring

Blood glucose levels were monitored three times a week following the transplant surgery. A small drop of blood was collected from the tail vein using a lancet and tested using a commercial glucometer (Clarity One, Clarity Diagnostic Test Group, Boca Raton, FL). Mice with unfasted blood glucose levels below 200 mg/dL were considered normoglycemic.

3.2.12 Histological analysis

The retrieved devices were fixed in 4% paraformaldehyde, embedded in paraffin, and sectioned by the Cornell Histology Core Facility. Ten-micrometer-thick paraffin sections were stained with hematoxylin/eosin. For staining of insulin with immunofluorescence, paraffin-embedded sections were rehydrated by sequentially washing in xylene, 100%, 95%, 75% ethanol and water. Then slides were boiled in 1mM EDTA for antigen exposure. After blocking, primary Guinea pig anti-rat insulin antibody (Linco, 1:200) were applied and incubated overnight at 4°C, followed with wash and incubation with FITC-conjugated Donkey anti-Guinea pig IgG (Jackson ImmunoResearch, 1:200). Slides were washed twice with water, applied with antifade/DAPI and covered with coverslips. Fluorescence Images were captured under a Zeiss LSM710 confocal microscope at Cornell Biotechnology Resource Center Imaging Facility.

3.3. Results and Discussion

3.3.1 Fabrication and characterization of NEEDs

To fabricate the tubular NEEDs, we first electrospun nanofibers directly onto a rotating aluminum rod, as shown in Figure 3.1a, to form nanofibrous tubes^{117, 118}. Different polymers (Figure 3.2) could be spun, and we chose Nylon due to its excellent mechanical property and wide usage as a clinically approved suture material. The tubes in the presence of the rod template were then placed in a hydrogel precursor solution such as alginate in a vacuum chamber for wicking (see Figure 3.1b for a schematic). The vacuum could remove any air trapped in the viscous solution and the nanofiber membrane, and therefore facilitate the wicking. The wicking of liquid into a porous

medium is a well-studied phenomenon. For example, when a porous medium is assumed to consist of a bundle of parallel capillary tubes of diameter D in which the liquid follows the Hagen-Poiseuille flow and the effect of gravity is neglected, then how far the liquid can penetrate the porous medium (L) at time t is described by the Washburn equation¹²²: $L = [\gamma D \cos(\theta) t / (4\mu)]^{1/2}$ where γ is the liquid surface tension, θ is the contact angle of the liquid on a smooth surface made of the medium material, and μ is the liquid viscosity. From this equation, it is obvious that the wicking occurs when $\theta < 90^\circ$. With a water contact angle of $\sim 60^\circ$ on smooth Nylon polymer surface, the surface tension-driven wicking enables the infiltration of alginate solution into the porous walls of the nanofibrous devices. To confirm the infiltration and visualize the hybrid structures of NEEDs, we incorporated a Rhodamine (red) fluorescent dye into the Nylon nanofibers and covalently labeled alginate with an Alexa Fluor (green) dye, as shown in Figure 3.1c-e. Similarly and more interestingly, NEEDs with more complex, multicompartmental structures (Figure 3.1f) can be fabricated by wrapping several tubes together through an additional nanofiber deposition. The different compartments in the NEEDs are separated by robust nanofiber/hydrogel hybrid membranes that prevent the direct cell contacts but allow chemokine/cytokine exchanges. Therefore, these devices may find applications for paracrine cell co-cultures and co-delivery of multiple types of cells.

The thickness of the nanofibrous walls of the electrospun tubes can be tuned by adjusting the deposition time, while the inner diameter of the tubes can be controlled by changing the diameter of the rod template. Nanofibrous Nylon tubes with different diameters ranging from 300 μm to 3 mm and wall thickness of $\sim 20 \mu\text{m}$ were fabricated

and shown in Figure 3.3a. The devices with multiple (2 to 4) compartments were also demonstrated. Figure 3.3b shows scanning electron microscopy (SEM) images of an electrospun Nylon tube and its nanofibrous walls. The average diameter of individual Nylon fibers was around 200 nm. Although the exact pore structures of the nanofiber nonwoven walls were difficult to quantify, they were sufficiently tight so that the cells could not escape¹²³, while oxygen, nutrients, metabolic wastes and therapeutic products were able to diffuse in and out freely. Based on these nanofibrous tubes, tubular NEEDs were made by wicking an alginate solution into the tube walls. The tubes holding alginate were dipped into a BaCl₂ solution to finish the crosslinking. NEEDs with different sizes and compartmentalizations are shown in Figure 3.3c, where the watery hydrogel surface can be seen. To confirm that the alginate hydrogel indeed penetrated the nanofiber membrane and that they were mechanically interlocked by the nanofiber structure, we freeze-dried a NEED and observed the lyophilized structures under a SEM. As shown in Figure 3.3d, the dehydrated alginate attached to the Nylon fibers and was uniformly distributed within the interstitial space. The inset digital photo and confocal image further revealed the watery appearance of the NEED at hydrated state and the thin (green) alginate hydrogel exterior, respectively. This composite structure brings together the advantages of both the nanofibers and the hydrogel to the NEED. On one hand, the nanofibers are coated with more biocompatible alginate hydrogel; on the other hand, the soft hydrogel is reinforced by the tough Nylon nanofibers, making it easier to handle and less likely to break or leak.

The NEED design can be applied to different hydrogel chemistries. In addition to the alginate, we demonstrated the fabrication of NEEDs with a photo-crosslinked

polyethylene glycol diacrylate (PEG-DA), an ionically crosslinked chitosan and a thermally crosslinked collagen. (Figure 3.4a-d). We quantified the mechanical enhancement by comparing the elastic moduli of the nanofiber-reinforced hydrogel sheet and the sheet made of the corresponding hydrogel alone. The stress-strain curves in Figure 3.4e-g clearly show that the mechanical properties of the hydrogels were greatly improved by Nylon nanofiber reinforcement. This is expected from the general rule of mixtures: $E_{total} = a_1E_1 + a_2E_2$, Where E_{total} , E_1 , E_2 are the Young's modulus of the composite material and the two different components, respectively; and a_1 , a_2 are their respective cross-sectional area fractions. With the enhancement of the mechanical properties, the handleability of NEEDs was also greatly improved as compared to the devices made of hydrogels alone. For example, an alginate fiber which appeared normal in a solution (Figure 3.4h) was difficult to handle by tweezers outside the solution (Figure 3.4i). In contrast, a tubular alginate NEED with similar dimensions was much more robust and easier to handle (Figure 3.4j).

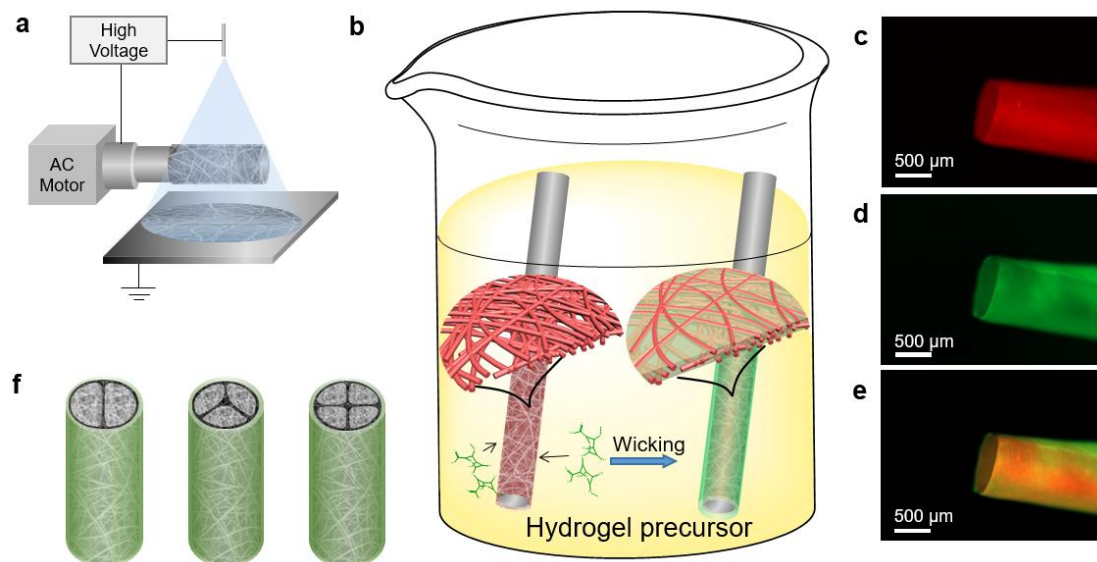


Figure 3.1. Design and fabrication of NEEDs. **a**, A schematic of the electrospun nanofibers being collected on a rotating template. (Planar devices can be fabricated by changing the rod to a sheet as the template.) **b**, A schematic of the wicking process. **c-e**, Fluorescent microscope images of a NEED where the nanofibers and the hydrogel (alginate) were labeled with different colors; Red: Nylon nanofibers (**c**), Green: alginate hydrogel (**d**), Merge (**e**). **f**, Schematics of the compartmentalized NEEDs.

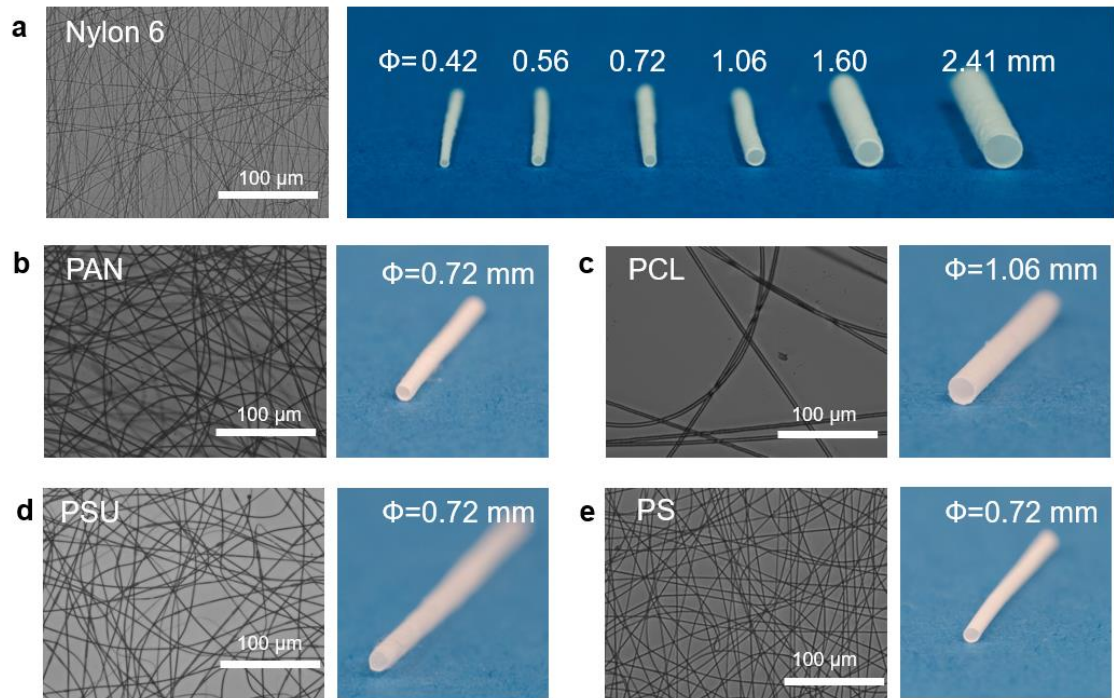


Figure 3.2. Microscopic images and digital photos of various electrospun nanofibers and nanofibrous tubes. **a**, Nylon 6. **b**, Polyacrylonitrile. **c**, Polycaprolactone. **d**, Polysulfone. **e**, Polystyrene.

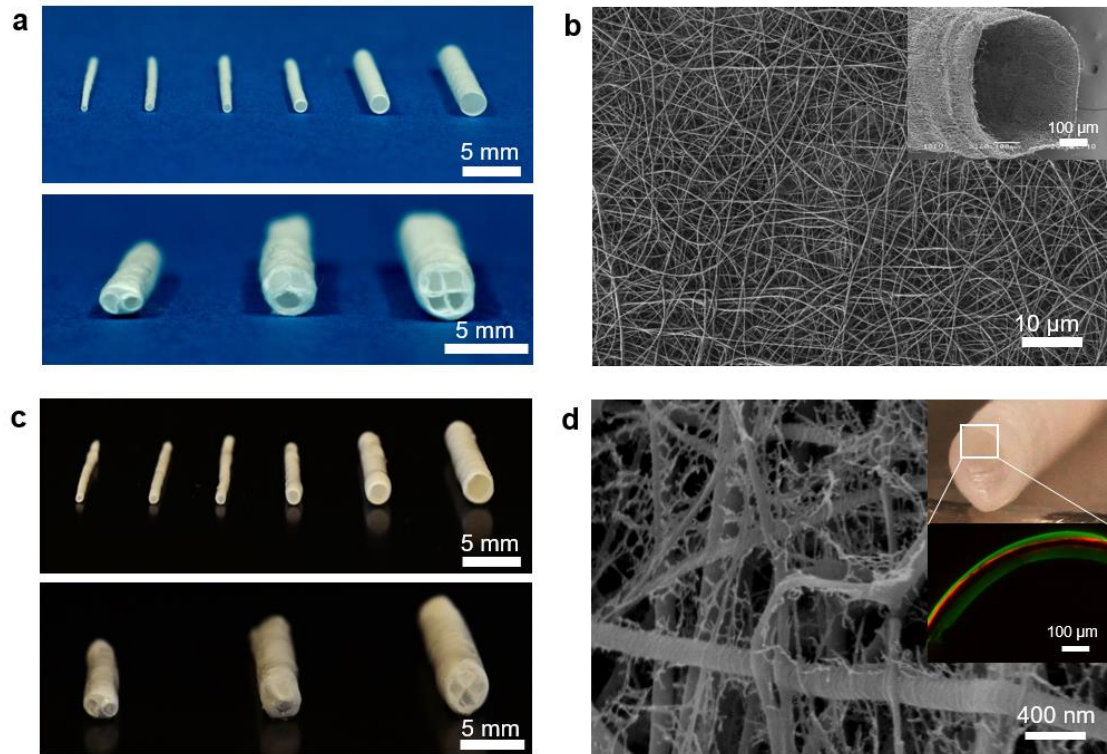


Figure 3.3. Characterizations of NEEDs. **a**, Digital images of the electrospun Nylon nanofiber tubes with different sizes or capacities (top) and multi-compartments (bottom). **b**, SEM images of a nanofibrous tube with the inset showing the open end. **c**, Digital images of different alginate NEEDs. **d**, A SEM image of the wall of a freeze-dried NEED; insets: a digital image of the NEED (top) and a confocal image (bottom) of the cross section of the NEED (red: nanofibers; green: alginate).

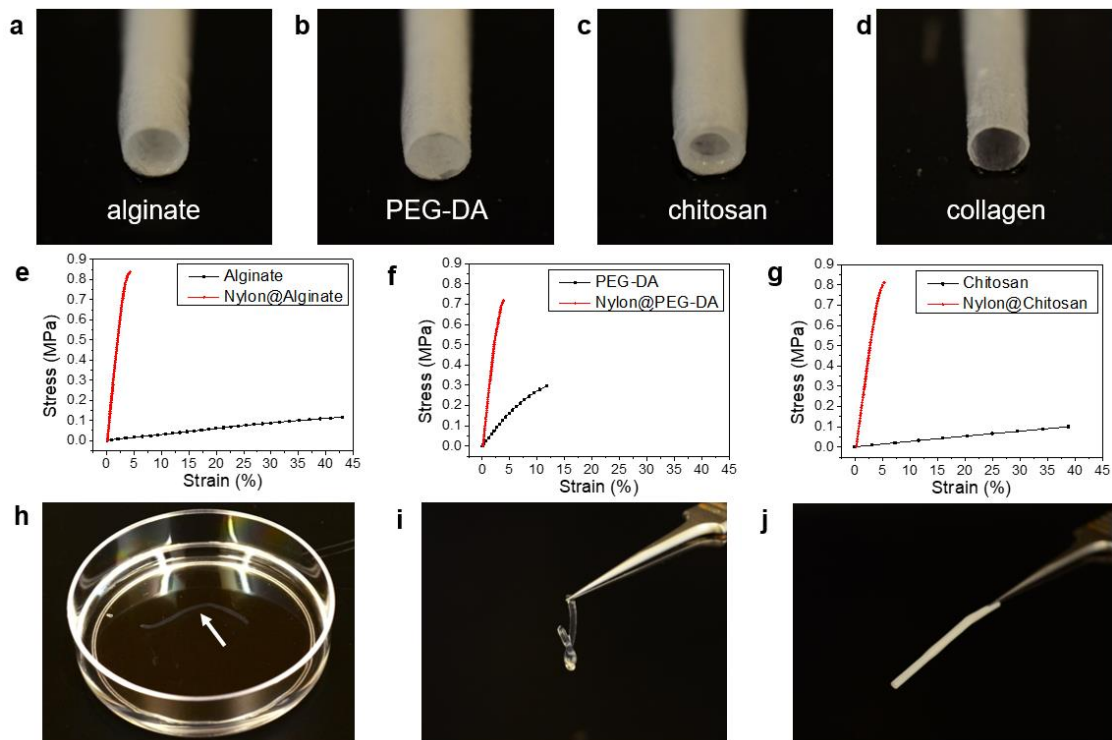


Figure 3.4. NEEDs with different hydrogel chemical compositions and their robust mechanical properties. **a-d**, Digital images of alginate, PEG, chitosan and collagen NEEDs. **e-h**, Comparisons of stress-strain curves of different hydrogel sheets and the corresponding nanofiber-reinforced ones with similar dimensions. (Due to the difficulties of fabricating tubular devices with hydrogels alone, a sheet format was used for the measurements and the demonstration of the mechanical property enhancement. The collagen sheet or fiber was too weak to measure and therefore not shown here.) **h-j**, A comparison of handleability between an alginate hydrogel fiber and an alginate NEED with the same outer diameter and length: the alginate fiber placed in a petri dish (**h**) and handled by tweezers (**i**); the NEED handled by tweezers (**j**).

3.3.2 Cell encapsulation and culture

The application of NEEDs for cell encapsulation and culture was demonstrated first by using a model cell line, MDA-MB-231 cells. The cells were dispersed in Matrigel™, a commercially available extracellular matrix favored by many cell types, and then injected into an alginate NEED. After sealing the open end with a drop of electrospinning solution and an additional alginate coating, the NEED was put into culture and the cells were characterized. Figures 3.5a and Figure 3.5b show cell viabilities right after encapsulation and cultured for 5 days. The growth curves were obtained using MTT (methyl thiazolyl tetrazolium) assays (Figure 3.5c) where the control group was the same number of MDA-MB-231 cells seeded onto petri dishes. Both the cell viability and the growth comparison confirmed that the NEED had sufficient mass transfer to support cell survival and proliferation. Another cell line GATA6WT was utilized as an additional example of cell encapsulation where the cells were encapsulated in both tubular and planer NEEDs. Similarly, high cell viability was observed (Figure 3.6). A unique feature in the NEED design is the compartmentalization which enables co-encapsulation of different types of cells in individualized compartments, rather than a simple, random mixture. The cells are physically separated but soluble factors (chemokines and cytokines) are essentially interchangeable due to the high permeability of the membranes and the proximity of the cells located in different compartments. Such a system may find applications as a novel, implantable platform for studying cell co-cultures, and paracrine signaling¹²⁴ under both in vitro and in vivo environments. To provide a proof of concept, MDA-MB-231-EGFP (green) cells and MDA-MB-231-dTomato (red) cells were used as model cells for co-

encapsulation. The two types of cells were seeded into the two compartments within one single alginate NEED as shown by the 2D and 3D fluorescent images in Figure 3.5d-f. In principle, more types of cells can be readily encapsulated, co-cultured and even delivered, all in a single device.

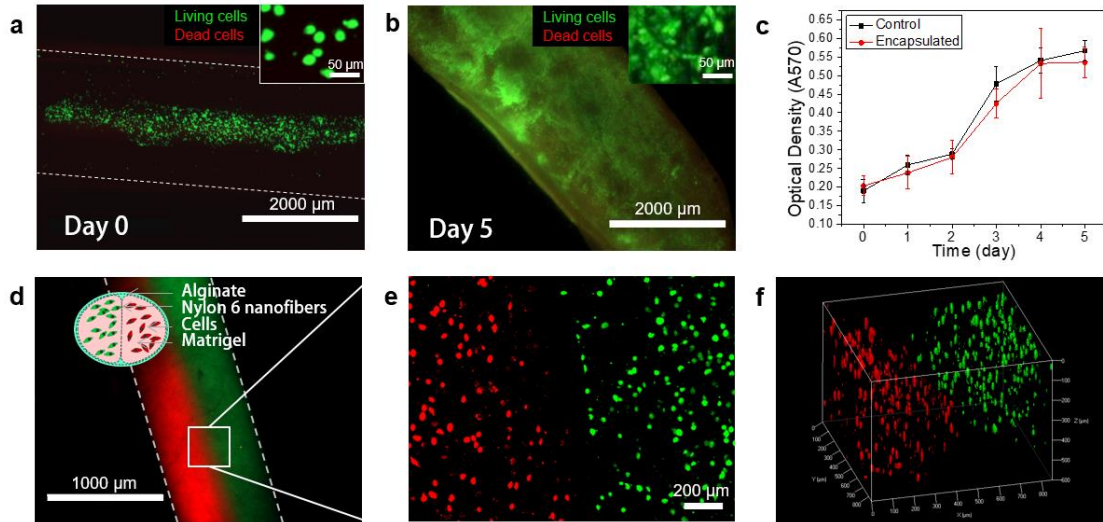


Figure 3.5. *In vitro* model cell encapsulation and culture using NEEDS. **a, b**, Images of encapsulated MDA-MB-231 cells stained with calcium-AM (green, live) and ethidium homodimer (red, dead) 0 day (**a**) and 5 days (**b**) after encapsulation in alginate NEEDS. **c**, Growth curves of the encapsulated MDA-MB-231 cells by MTT analysis (mean \pm s.d., n=3). **d-f**, Images of the MDA-MB-231-EGFP and MDA-MB-231-dTomato cells encapsulated in a compartmentalized NEED: a fluorescent microscope image with the inset illustrating of the cross-section of the device (**d**); a confocal image of the encapsulated cells at a higher magnification (**e**); and a 3-dimensional fluorescent image showing the relative localizations of the encapsulated cells (**f**).

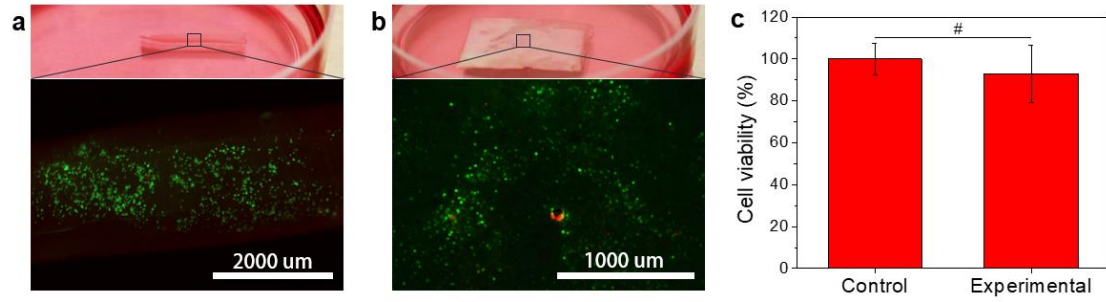


Figure 3.6. *In vitro* cell encapsulation and viability test. Digital photos and live (green) / dead (red) staining images of tubular (a) and planar (b) NEEDs encapsulating keratinocytes. c, Quantitative comparison (n=3) of the cell viability between encapsulated cells (in tubular NEEDs) and un-encapsulated ones (control).

3.3.3 Islet encapsulation and transplantation

Next, we tested the potential applications of NEEDs for cell therapies using a type 1 diabetic model. Pancreatic islets isolated from Sprague-Dawley rats were encapsulated in tubular alginate NEEDs. Both the viability staining (Figure 3.7a, b) and the immunostaining of the insulin (Figure 3.7c) of the encapsulated islets after overnight culture confirmed that NEEDs supported the survival of islets. More importantly, the glucose-stimulated insulin secretion (GSIS) assay (Figure 3.7d) indicated approximately the same level of insulin secretion upon glucose stimulation between the encapsulated islets and the control (islets cultured in medium), pointing to the facile mass transfer of not only nutrients but also the secreted insulin. Encouraged by these results, we transplanted the encapsulated rat islets into immunocompetent, streptozocin (STZ)-induced diabetic mice. We chose C57BL/6 mice as the donor because they were a challenging strain known to develop more fibrosis against alginate than other models such as BALB/c mice¹²⁵. For each mouse, we implanted intraperitoneally a ~1 inch long NEED with ~500 islet equivalences (IE's; see Materials and method section for details). Figure 3.7e shows the blood glucose concentrations (BG) over time post-transplantation. The diabetes was reversed 2 days after the implantation and remained cured (i.e. BG < 200 mg/dL) for at least 8 weeks when the experiment was ended. The devices were then retrieved and all the mice went back to a diabetic state, confirming the effectiveness of NEEDs in regulating blood glucose levels and controlling diabetes. The retrieved devices had no visible tissue adhesion or extensive fibrosis (Figure 3.8a). Histological studies (Figure 3.8b, c) revealed only a very thin (about one layer of cells) layer of cellular overgrowth and more interestingly the alginate hydrogel was still firmly

attached to the nanofiber membranes, consistent with the mechanical characterization. The islets observed from the retrieved devices appeared to have distorted morphology, suggesting those islets might have experienced certain stress in this non-native environment. However, importantly the islets seemed to still be functional after 8 weeks of implantation, as indicated by positive insulin staining (Figure 3.7f). Taken together, the data obtained from this in vivo experiment suggested that the NEEDs were mechanically robust, biocompatible, retrievable and had sufficient mass transfer for potential therapeutic applications.

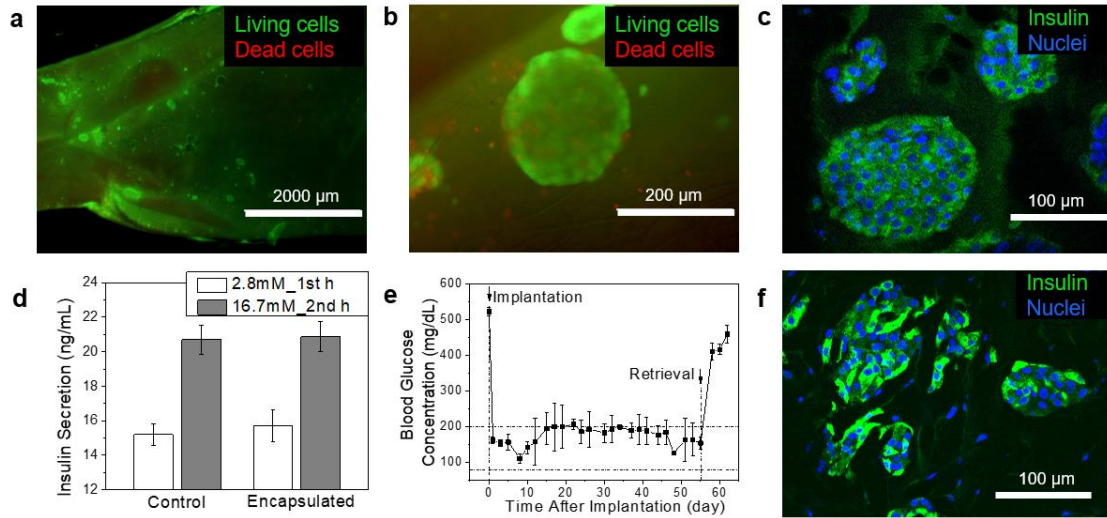


Figure 3.7. Islet encapsulation and transplantation using NEEDs. **a, b**, Fluorescent Images of the encapsulated islets stained with calcium-AM (green, live) and ethidium homodimer (red, dead) after overnight culture. **c**, Images of immunostaining of the encapsulated islets (green: insulin, blue: nuclei). **d**, Glucose stimulated insulin secretion of the islets cultured in medium (control) and encapsulated in NEEDs (mean \pm s.d., n=3). **e**, Blood glucose concentrations (mean \pm s.d., n=3) of STZ-induced diabetic mice after the transplantation of encapsulated rat islets; the devices were retrieved after 8 weeks of implantation. **f**, Immunohistochemical staining of the islets in a retrieved device (green: insulin, blue: nuclei).

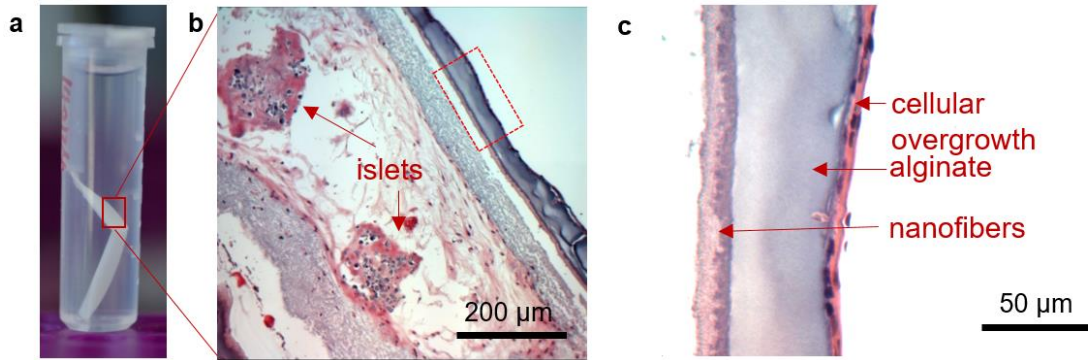


Figure 3.8. Histology study of the retrieved NEEDs. **a**, A representative digital image of the retrieved devices. **b**, Histology analysis of the retrieved devices. Sections were stained with H&E and observed under a light microscope. **c**, A magnified image of the wall of the retrieved device shown in (b) where the nanofibers, alginate hydrogel and cellular overgrowth are indicated by arrows.

3.3.4 Discussion

Cell encapsulation has been investigated for decades, but clinical application has remained elusive, partially because of the lack of an appropriate, translatable encapsulation material or device⁵². There are currently two major types of encapsulation systems: microscopic capsules and macroscopic devices. The microcapsules, typically made of alginate, have many advantages for cell encapsulation. They are relatively biocompatible, easily implantable and have large surface area for mass transfer¹²⁶. Numerous research groups have made tremendous progress including both animal studies and clinical trials^{97, 127}. However, the inconvenience of retrieving the microcapsules after transplantation may become a concern for eventual clinical uses⁸⁰. The retrievability is particularly desirable if stem cell-derived cells are used due to the risk of potential teratoma formation. On the other hand, the macroscopic devices can potentially be retrieved (if there is no tissue adhesion or ingrowth), but other challenges exist. For example, the devices made of porous polymer membranes have potential issues with fibrosis⁵². Alginate hydrogel sheets or fibers, although presumably more biocompatible, have potential problems with mechanical robustness. In addition, they do not allow for flexible cell loading. Thus, new encapsulation devices with robust biocompatibility, superior mechanical and mass transfer properties that allow for flexible cell loading, easy implantation, and convenient retrieval are highly desirable. In this work, we developed nanofiber-enabled hydrogel encapsulation devices that combined the properties of nanofiber membranes (e.g. mechanical strength, fine and interconnected pore structures, and tunable wettability) and those of hydrogels (e.g. facile mass transfer and biocompatibility^{106, 107}) The success of cell encapsulation

materials are coupled to the appropriate transport of gases, nutrients, proteins, cells and waste products into and out of the scaffold¹²⁸. Electrospun nanofiber scaffolds contain pores on the nanometer size scale, which can limit cell migration. While due to their high porosity, these nanofiber scaffolds can overcome mass transfer limitations associated with other polymeric systems¹²⁹. On the other hand, the diffusional properties of hydrogels are already well studied and modeled previously¹³⁰. In this work, we demonstrated that mass transport of NEED is not an issue, since encapsulated cells live and proliferate normally and the desired cell secretion product (insulin) can diffuse out freely. In addition, the fact that the cells can be loaded in a custom designed way with controlled extracellular matrix and space makes it possible to deliver cells that have certain proliferation potential. We are currently applying the NEEDs to studying the cell-autonomous effect of certain gene knockouts on beta cell proliferation *in vivo*.

Since the fabrication is based on a simple capillary action, the design of NEEDs is not limited to any polymer or hydrogel. For example, biodegradable polymer (e.g. polycaprolatone) nanofibers can be combined with non-degradable, tough (e.g. Nylon) nanofibers to make nanofibrous devices where the biodegradable component may release anti-inflammatory drugs to mitigate the fibrosis¹³¹. Similarly, the hydrogels can have almost any chemical compositions, either bio-inert (e.g. ultra-compatible, chemically modified alginates and foreign body response-resistant zwitterionic polymers¹³²) or bioactive (e.g. collagen and fibrin). The NEEDs may be further coated with polyelectrolytes to control permselectivity¹³³ or biocompatibility¹³⁴. In addition to the diverse chemical compositions, it is also possible to design NEEDs with multicompartments. Compared with the single-compartment devices, the

multicompartmental ones are particularly interesting because they may provide a novel, implantable platform for cell co-culture, migration and paracrine signaling assays that have typically been studied at present in Transwell™ systems. Though NEEDs have several advantages mentioned above and have demonstrated good performance, there are still some improvements that need to be addressed to make these cell encapsulation devices work better. For instance, more work is required to deal with the fibrosis problem, and the feasibility of implantation and retrieval in large animals is another key issue for the cell encapsulation devices.

3.4. Conclusion

A new type of cell encapsulation device, NEED, is described. The mechanical strength and unique micro/nano structures of electrospun fibers enabled the development of robust encapsulation devices from hydrogels that may not be able to form mechanically stable devices (such as small diameter tubes) on their own. We demonstrated encapsulation and culture of several different types of cells including both single cells and cell aggregates (islets). Further compartmentalization of the NEEDs provides opportunities for cell co-encapsulation, co-culture and co-delivery. Lastly, we demonstrated the therapeutic potential of the NEEDs through a type 1 diabetic model using primary islets. We expect this encapsulation design will be applicable to other types of cells particularly those stem cell-derived ones^{135, 136} because of its relative biocompatibility of the hydrogel and the mechanical robustness of the nanofiber membranes. This proof-of-concept study suggests that the NEEDs can potentially overcome some of the challenges in the cell encapsulation field and may therefore contribute to the development of cell therapies in future.

CHAPTER 4: DEVELOPING A RETRIEVAL AND SCALABLE CELL ENCAPSULATION DEVICE FOR POTENTIAL TREATMENT OF TYPE 1 DIABETES

4.1 Introduction

There have been huge research efforts worldwide to develop a functional and durable cell encapsulation system for clinical uses, from animal studies¹³⁷⁻¹³⁹ to human trials¹⁴⁰. However, the lack of a suitable immunoisolation device has prevented this approach from being clinically used¹⁴⁰. The devices used to date (e.g. TheraCyte®, Encaptra® and Neurotech devices) are predominantly made from phase-inverted membranes, polyethylene netting meshes, and expanded Teflon. These materials were originally designed for filtration and the textile industry and suffered serious problems when used for immunoisolation including insufficient biocompatibility and suboptimal wettability, permselectivity, and mass transport properties. Moreover, these macroscopic devices have a small surface area for mass transfer and consequently low encapsulation capacity^{52, 80, 141-143}. Even though the capacity problem may be addressed by increasing the cell packing density, dense packing will also inevitably lead to a hypoxic environment and associated impairment in insulin secretion¹⁴⁴. Thus, the scale-up to a capacity sufficient to cure a human patient has been challenging^{4, 52, 80, 141, 143, 145}. Retrievability is another very important factor affecting a successful cell encapsulation device. Unable to completely retrieve the device will raise significant risks and concerns in the event of transplant failure or medical complications^{4, 52, 56, 103, 146}. Retrievability is also an important issue associated with the regulatory approval process¹⁴⁷.

To address these challenges, here we report a simple and translatable cell encapsulation design that is both scalable and retrievable. The design involves a one-step *in situ* crosslinking of an alginate hydrogel around a nanoporous, wetttable, Ca²⁺-releasing polymer thread. We term the design as TRAFFIC (Thread-Reinforced Alginate Fiber For Islets enCapsulation). In TRAFFIC, the hydrogel encapsulating the cells provides the necessary mass transfer and biocompatibility similar to conventional hydrogel capsules, while the polymer thread imparts mechanical strength and enables easy handling, implantation, and retrieval. The device may be extended to meters long and still be entirely retrievable through a minimally invasive laparoscopic procedure. To demonstrate the therapeutic potential of the device, we encapsulated and transplanted rat islets into diabetic C57BL/6 mice or human islets into SCID-Beige mice and obtained diabetes correction for up to several months. As a proof of concept, we scaled up the device and showed its retrievability in dogs. Given its simplicity and translatability, this device may contribute significantly to a cell encapsulation therapy for T1D and potentially many other diseases.

4.2 Materials and Methods

4.2.1 Chemicals

Calcium chloride (CaCl₂), barium chloride (BaCl₂), sodium chloride (NaCl), poly(methyl methacrylate) (PMMA), N,N-dimethylformamide (DMF), Glucose stock solution, HSA, and IBMX were purchased from Sigma-Aldrich Co. (St. Louis, MO). Forskolin was purchased from Tocris Bioscience. Glutamax was purchased from Life Technologies. KRBH was purchased from VWR. Glucose was purchased from Mallinckrodt Pharmaceuticals (Dublin, Ireland). Ultrapure, sterile sodium alginate

(SLG100) was purchased from FMC BioPolymer Co. (Philadelphia, PA). (Note that alginates used in this study had no significant amount of endotoxin according to a previous publication⁴⁶) Water was deionized to 18.2 M Ω -cm with a Millipore purification system.

4.2.2 Animals

C57BL/6 and BALB/c mice were purchased from The Jackson Laboratory (Bar Harbor, ME). SCID-Beige mice for transplantation experiments were obtained from Taconic Farms (Hudson, NY) and Taconic, Denmark. Sprague-Dawley rats for isolation of pancreatic islet cells were obtained from Charles River Laboratories (Wilmington, MA). Beagle dogs for implantation were obtained from Marshall Bioresources (Clyde, NY). All animal procedures were approved by the Cornell Institutional Animal Care and Use Committee. Transplantation of encapsulated human islets in diabetic SCID-Beige mice was performed at Novo Nordisk A/S and the protocols were approved by the Danish Animal Experimentation Inspectorate and carried out by trained and licensed personnel.

4.2.3 Characterizations

The samples were characterized by different analytical techniques. Scanning electron microscopy (SEM) and energy dispersive spectrometer (EDS) element mapping were performed by using a field emission scanning electron micro-analyzer (LEO 1550). Optical and fluorescent microscopic images were observed using a digital inverted microscope (EVOS fl). Conventional macro-tensile measurements were performed using a dynamic mechanical analysis (DMA Q800). All samples were mounted between holders at a distance of ~1.5 cm. Tensile testing was conducted at a

rate of 0.5 N/min at room temperature (23 °C). Stress (MPa) and strain (%) were automatically calculated by the software. Confocal images were taken by using a Laser Scanning Confocal Microscope (LSM 710).

4.2.4 Fabrication of modified threads

Typically, two sterile sutures (Ethilon ® nylon suture, 5-0, monofilament, Ethicon, Inc. KRUUSE nylon suture, 5-0, Jørgen Kruuse A/S) were twisted together to accumulate some torsion. Then, the twisted sutures were folded in the middle which causes the sutures to self-twist again to release the torsion. Knots were made at the end of the twisted sutures to prevent the sutures from un-twisting. Then, the sutures were submerged into 7% (w/v) PMMA/DMF solution, containing 2.5% (w/v) CaCl₂, for approximately 3 seconds. The sutures were taken out from the polymer solution and air dried. After the modification was finished, all the sutures were sterilized by ethylene oxide or by autoclave in dry mode before use.

4.2.5 Rat islet isolation and purification

Sprague-Dawley rats from Charles River Laboratories weighing approximately 300 g were used for harvesting islets. All rats were anesthetized using 3% isoflurane in oxygen and maintained at the same rate throughout the procedure. Isolation surgeries were performed as described by Lacy and Kostianovsky¹²⁰. Briefly, the bile duct was cannulated and the pancreas was distended by an *in vivo* injection of 0.15% Liberase (Research Grade, Roche) in RPMI 1640 media solution. The pancreas was digested a 37°C water bath for 30 min. The digestion was stopped by adding 10-15 mL of cold M199 media with 10% heat-inactivated fetal bovine serum and a slight shaking. Digested pancreases were washed twice in the same aforementioned M199 media,

filtered through a 450 μm sieve, and then suspended in a Histopaque 1077 (Sigma)/M199 media gradient and centrifuged at 1,700 RCF at 4°C. This gradient centrifugation step was repeated for higher purity islets. Finally, the islets were collected from the gradient and further isolated by a series of gravity sedimentations, in which each supernatant was discarded after 4 min of settling. Purified islets were hand-counted by aliquot under a light microscope and then washed three times in sterile PBS. Islets were then washed once in RPMI 1640 media with 10% heat-inactivated fetal bovine serum and 1% penicillin/streptomycin, and cultured in this medium overnight for further use.

4.2.6 Cell encapsulation

For a typical mouse device, the modified thread was inserted into a polyethylene tube (~1.5 mm inner diameter). A pre-determined amount of cell-loaded alginate solution (e.g. ~500 IEQ's dispersed in ~60 μL 2% w/v alginate solution) was filled into the tube using a micropipette and left for 4 min. Then, the TRAFFIC device was carefully pulled out of the tube using tweezers. Most alginate and cells were incorporated into the device and the leftover alginate in the tube was usually unnoticeable with a small number of islets adhered to the tube wall. It was estimated from multiple observations that the encapsulation efficiency was at least 90% (data analyzed and estimated from 5 isolations with ~30 independent trials). Given the ~500 IEQ's we started with, we determined the actual IEQ for transplantation was 475 ± 25 . The device was further crosslinked by a crosslinking buffer containing 95mM CaCl_2 and 5mM BaCl_2 . Next, the device was washed three times with 0.9% (w/v) saline and transferred into corresponding cell culture medium. Islets were typically treated as

following for encapsulation. Immediately prior to encapsulation, the cultured islets were centrifuged at 1,400 rpm for 1 minute and washed with Ca-free Krebs-Henseleit (KH) Buffer (4.7 mM KCl, 25 mM HEPES, 1.2 mM KH₂PO₄, 1.2 mM MgSO₄·7H₂O, 135 mM NaCl, pH ≈ 7.4, osmotic pressure ≈ 290 mOsm). After the wash, the islets were centrifuged again and all supernatant was aspirated. Then, the collected islets were encapsulated following the procedure described above. The TRAFFIC devices encapsulating cells were checked under microscope to ensure that no cells were exposed on the hydrogel surface. Since the islets had variable sizes (50 – 400 μm), the total number of encapsulated islets were converted into islet equivalences (IEQ's, normalized to 150 μm size) based on a previously published method¹²¹.

4.2.7 Static glucose-stimulated insulin secretion (GSIS) assay

Krebs Ringer Bicarbonate (KRB) buffer (2.6 mM CaCl₂·2H₂O, 1.2 mM MgSO₄·7H₂O, 1.2 mM KH₂PO₄, 4.9 mM KCl, 98.5 mM NaCl, and 25.9 mM NaHCO₃ (all from Sigma-Aldrich, St. Louis, MO) supplemented with 20 mM HEPES/Na-HEPES (Roche, Indianapolis, IN) and 0.1% BSA (Serological, Norcross, GA), was prepared beforehand. Encapsulated islets were incubated for 2h in KRB buffer at 37°C, 5% CO₂, and then incubated for 75 min with 2.8 mM or 16.7 mM glucose under the same condition. Insulin concentrations in the buffer solutions were determined by using ultrasensitive mouse/rat insulin ELISA kit (Crystal Chem) or human insulin ELISA kit (ALPCO) per suppliers' protocols. For devices retrieved from mice, 3 out of 5 retrieved TRAFFIC devices were tested with the GSIS assay (the remaining 2 devices were fixed right after retrieval and submitted for histology); for devices retrieved from dogs, 3 independent regions of the retrieved devices were cut and tested with the GSIS assay.

All the ELISA results were normalized to the IEQ's.

4.2.8 Perifusion test

Human islets were purchased from Prodolabs. Upon receipt, viability was assessed with the LIFE/DEAD Viability/Cytotoxicity kit (calcein-AM staining indicating living cells and ethidium homodimer-1 staining indicating dead cells) according to manufacturer's instructions (Invitrogen). Dynamic insulin release was examined with a perifusion system from Biorep, Miami Lakes, FL according to manufacturer's guidelines. In short, 250 hand-picked human islets or 1/3 device (expected 500 IEQ) were loaded on columns surrounded by Bio-Gel P-4 beads (Biorad) and allowed to acclimate for 60 min in KRBH containing 2 mM glucose at 100 μ l/min flow (kept constant during the experiment). Islets were then exposed to different glucose concentrations and/or factors and secreted insulin was collected in defined time frames. After the experiment, islets were collected and lysed (tissue extraction reagent I (Invitrogen) + tissue lyzer (Qiagen)). The insulin concentration was measured and normalized to DNA concentration (PicoGreen dsDNA kit, Thermofisher).

4.2.9 Implantation and retrieval in mice

Immune-competent male C57BL/6 mice and immuno-deficient SCID-Beige mice were utilized for transplantation. To create insulin-dependent diabetic mice, healthy mice were treated (50 mg/kg mouse) with freshly prepared streptozocin (STZ) (Sigma-Aldrich) solution (7.5 mg/mL in sodium citrate buffer solution) for 5 consecutive days. The blood glucose levels of all mice were retested prior to transplantation. Only mice whose non-fasted blood glucose levels were above 300 mg/dL for two consecutive measurements were considered diabetic and underwent

transplantation. The non-diabetic or STZ-induced diabetic mice were anesthetized with 3% isoflurane in oxygen and their abdomens were shaved and sterilized using betadine and 70% ethanol. Preoperatively, all mice received 0.3 mL of 0.9% saline subcutaneously to prevent dehydration. A ~1 mm incision was made along the midline of the abdomen and the peritoneal lining was exposed using blunt dissection. The peritoneal wall was then grasped with forceps and a ~1 mm incision was made along the linea alba. The device was then inserted into the peritoneal cavity through the incision. The incision was closed using 5-0 taper polydioxanone (PDS II) absorbable sutures. The skin was then closed over the incision using a wound clip. The devices were retrieved from mice at desired time points post-implantation or transplantation (with encapsulated cells) using similar procedures except that larger (~5 mm) incisions were made in the skin and the peritoneum. The device was located, grasped and pulled out by using blunt tweezers. After retrieval, the TRAFFIC devices were first submerged into a crosslinking solution containing 95 mM CaCl_2 and 5mM BaCl_2 for ~5min, and then transferred into a 4% paraformaldehyde for fixation or a cell culture medium for post characterization.

For the SCID-Beige mice and human islet study, the mice were rendered diabetic by 5 consecutive doses of STZ (70 mg/kg). During the first week after the STZ treatment, the mice were not intervened. After the first week, if the body weight of a mouse dropped more than 10%, the mouse was treated with insulin (NPH 100nmol/kg 1X daily). The insulin treatment was independent on whether the mouse was from experimental or control groups. Normally, the diabetic mice were used 3-4 weeks after STZ treatment, but for this batch of experiment, mice were used about 45 days after

treatment due to the logistics associated with human islet isolation and delivery. The TRAFFIC device transplantations were performed as described above but anesthesia and analgesia procedure were performed as for the kidney capsule transplantation.

Kidney capsule transplantation: Mice were anaesthetized using 5 % isoflurane with O₂ flow set at 1 liter for anesthetic induction (approx. 1-2 min). The anesthesia was maintained using 1-1.5% isoflurane. Rimadyl: 5 mg/kg. s.c. was administered 30 min pre-surgery and +24 +48 h post surgery. Temgesic: 0.05 mg/kg. was dosed s.c 30 min pre-surgery and 3-6 h post- surgery.

The sedated mice were shaved in the surgical area, more specifically the left lateral side of the mouse approximately 3x3 cm and about 2 cm from last rib down. The skin was washed with iodide and ethanol. The shaved area covered with a barrier drape. A small incision through the skin and muscle of the left flank of the animal was made and the kidney exposed outside the body using two saline-moistened cotton-tipped applicators. The kidney capsule was sliced using a small needle leaving a small hole. A pouch was made using a rounded glass capillary and a transfer pipette was used to transplant clusters of islets into the pouch. The kidney was returned to the peritoneal cavity and the muscle layer closed with a 4-0 absorbable suture and the skin closed with 2-3 staples.

4.2.10 Laparoscopic implantation and retrieval in dogs

Dogs were premedicated with glycopyrolate and butorphanol, induced with propofol, and anesthetized with isoflurane and oxygen. The abdomen was clipped and prepared for sterile surgery. A 10 mm laparoscopic camera port and two 5 mm instrument ports were percutaneously inserted into the abdomen. The abdomen was

insufflated to 12 mm Hg pressure with CO₂. The device was inserted into the abdomen through the left side instrument port. A laparoscopic probe was introduced through the right sided 5 mm port and was used to manipulate the device so that it was placed between the liver and the diaphragm. The remaining ports were then removed and the port sites were closed with 3-0 polydioxinone suture material. For retrieval of the devices, the procedure was similar using one 10 mm camera port and one or two 5 mm instrument ports. The previously implanted device was located and photographed. The device was grasped with laparoscopic Kelly forceps inserted through a 5 mm port and dissected from attached omentum if necessary using laparoscopic scissors. The device was then removed from the abdomen through the 5 mm port. The remaining laparoscopic ports were removed and the dogs were humanely euthanized.

4.2.11 Blood glucose monitoring

Blood glucose levels were monitored three times a week in mice following transplant surgery. A small drop of blood was collected from the tail vein using a lancet and tested using a commercial glucometer (Clarity One, Clarity Diagnostic Test Group, Boca Raton, FL). Mice with unfasted BG levels below 200 mg/dL were considered normoglycemic. For BG test in SCID-Beige mice: Blood samples were obtained from the tip of the tail by puncturing the tail capillaries with a lancet in conscious mice. The blood (5 µL) was collected into Na-heparinised capillary tubes and transferred to 250 µL EBIO haemolysing buffer. The glucose concentration was measured on Biosen 5040 S line glucose analyzer (Eppendorf, Germany).

4.2.12 Histological analysis and immunostaining

The retrieved devices were fixed in 4% paraformaldehyde, embedded in

paraffin, sectioned by Cornell Histology Core Facility. Ten-micrometer-thick paraffin sections were stained with hematoxylin /eosin. For staining of insulin with immunofluorescence, paraffin-embedded sections were rehydrated by sequentially washing in xylene, 100%, 95%, 75% ethanol and water. Then slides were boiled in 1 mM EDTA for antigen exposure. After blocking, primary Guinea pig anti-rat insulin antibody (Linco,1:200) was applied and incubated overnight at 4 °C, followed with wash and incubation with FITC-conjugated Donkey anti-Guinea pig IgG (Jackson Immunoresearch, 1:200). Slides were washed twice with water, applied with antifade/DAPI and covered with coverslips. Fluorescence images were captured under a ZeissLSM710 confocal microscope. The histologic analysis of human islets is as follows: Devices and grafted kidneys were fixed in 10% natural buffered formalin, processed to paraffin and sectioned (3µm). Islet morphology was visualized with hematoxylin and eosin staining. Alpha and beta cells were visualized in a triple immunohistochemical stain with guinea pig anti-Insulin (1/75 in 0.05% TNB; A0564, DAKO), rabbit anti-Nkx6.1 (1/1000 in 0.05% TNB; HPA036774, Sigma Aldrich) and mouse anti-glucagon (1/7800 in 0.05% TNB; Glu-001, Novo Nordisk). Insulin was visualized with goat-anti-guinea pig-488 (A11073, Invitrogen) and donkey-anti-goat-488 (705-545-147, Jackson). Nkx6.1 was visualized with donkey anti-rabbit-biotin (711-065-152, Jackson) and TSA cy3 (NEL704A001KT, Perkin Elmer). Glucagon was visualized with donkey anti-mouse-Cy5 (715-175-151, Jackson). Antigens were first retrieved with TEG buffer (AMPQ17020, Ampliqon), after which slides were blocked with 1% hydrogen peroxide, avidin, biotin and TNB buffer (0.05%). The slides were then incubated with primary antibodies for 45 minutes, secondary antibody and DAPI

for 30 minutes, Streptavidin-PO (1:500) and tertiary antibody for 30 minutes, TSA-cy3 substrate for 15 minutes and finally the slides were mounted with a fluorescent mount (DAKO). The stains were visualized on an Olympus VS120 slide scanner.

4.2.13 Statistical Analysis

Results are expressed as mean \pm s.e.m. The data were analyzed via student's *t* tests and analysis of covariance (ANCOVA) followed by a Tukey post-hoc test where appropriate. Treatment (i.e. TRAFFIC vs. diabetic control, vs. non-diabetic control, etc.) was considered as a factor while time was treated as a continuous covariate. In many experiments there were data collected before the treatment was applied and/or after the treatment was removed (e.g. before implantation of TRAFFIC and after retrieval).

4.3. Results and Discussion

4.3.1 Design and Fabrication of the Device

The TRAFFIC device consists of a tough polymer thread and a uniform, strongly adhered alginate hydrogel layer with controllable thickness (Figure 4.1a). To obtain strong adhesion between the thread and the hydrogel, we designed the thread by mimicking the highly adhesive, nanoporous silks that certain spiders use for capillary-enabled water collection and retention¹⁴⁸. To achieve uniform, controllable hydrogel formation, we incorporated a Ca²⁺-releasing mechanism into the thread design. The fabrication process (Figure 4.1b) is simple but involves several material design principles. First, to create the spider-silk-like, nanoporous (and mechanically tough) thread, we chose to coat a nylon suture with 7% (w/v) poly(methyl methacrylate)/N,N-dimethylformamide (PMMA/DMF) solution. Under humid conditions, the drying of the

polymer solution resulted in evaporative cooling and phase separation, leading to nanoporous structures^{149, 150}. However, due to the surface tension-driven Rayleigh Instability^{151, 152}, the coating solution dewetted on the suture and formed patchy beads instead of continuous coatings (Figure 4.1c), leading to a “beads-on-a-string” morphology after drying. To overcome this problem, we twisted two sutures (typically 5-0) together to form a double helix and folded the helix in the middle. Upon folding, the torsion generated from the twisting spontaneously led to a stable 4-strand thread with a “ridges-in-grooves” structure (Figure 4.1d, e). In contrast to the coating on the smooth suture, the solution formed liquid wedges along the grooves of the twist-folded, 4-strand thread. This simple method prevented the dewetting and resulted in a continuous nanoporous coating (Figure 4.1d, e) on the thread. Lastly, within the nanoporous coating, we incorporated the crosslinking agent CaCl₂ by taking advantage of an unusual and unique property of CaCl₂ - its solubility in DMF. By dissolving 2.5% (w/v) CaCl₂ in the PMMA/DMF coating solution, we obtained a nanoporous thread with a uniform distribution of Ca and Cl as evidenced by energy dispersive X-ray (EDS) element mapping (Figure 4.1f).

After the thread was made, the formation of an alginate hydrogel layer or the fabrication of a TRAFFIC device was achieved through a simple, one-step, *in situ* crosslinking process (Figure 4.1b). In a typical process, a 2% (w/v) alginate solution (e.g. ultra-pure sterile SLG100 alginate dissolved in a 0.9 wt% NaCl solution) was placed in a tubular mold or a channel reservoir and a modified thread was then inserted into the alginate solution. After a four-minute crosslinking, the entire device was taken out and placed in a Ca/Ba solution (typically 95 mM CaCl₂ and 5 mM BaCl₂) for 5

minutes for further crosslinking. The hydrogel layer that formed around the thread was uniform (Figure 4.1g, h). In addition, examination of the interface between the nanoporous thread and the hydrogel in a lyophilized sample (Figure 4.1i) seemed to suggest that the hydrogel infiltrated into the porous surface, which was believed to contribute to the strong thread-hydrogel adhesion. For cell encapsulation, the process was similar and an alginate solution containing cells or cell aggregates such as rat islets (Figure 4.1j) was used for crosslinking. It is noted that the continuous nanoporous modification of the thread, resulted from the twisted helical structure and the evaporative cooling, and the internal release of Ca^{2+} are both of great significance to this encapsulation design. Simple sequential dipping of a conventional thread (i.e. bare suture) into a CaCl_2 solution and an alginate solution resulted in much less well controlled hydrogel formation¹⁵³. Our biomimetic thread may be used as an off-the-shelf, ready-to-use product for cell encapsulation conveniently at the research or transplantation place.

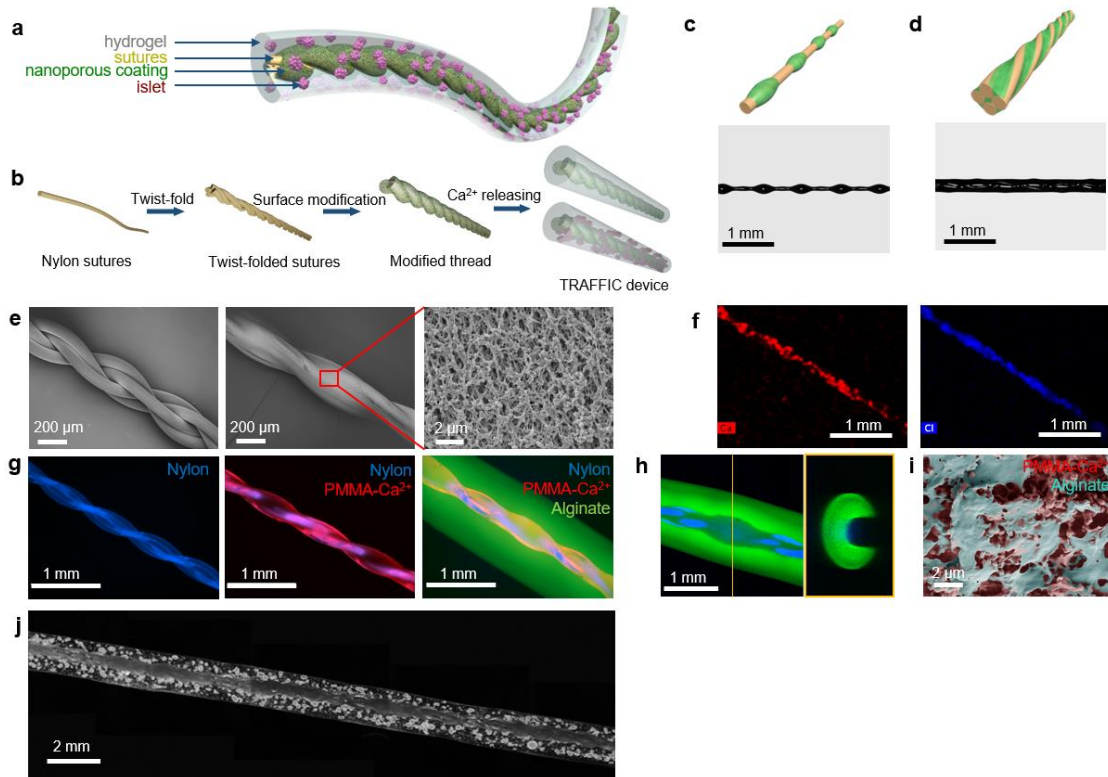


Figure 4.1. Schematics and fabrication of the TRAFFIC device. **a**, Schematic illustration of the design of TRAFFIC. **b**, Schematic illustration of the fabrication process. **c-d**, Schematic illustrations and optical images of the PMMA/CaCl₂/DMF solution coating on a monofilament nylon suture (**c**) and a thread made of twist-folded sutures (**d**). **e**, SEM images of the thread and the uniform nanoporous surface modifications. **f**, EDS element mapping of Ca and Cl on a modified thread. **g**, Fluorescent microscopic images of the thread, modified thread and a TRAFFIC device (without cells). **h**, Confocal images of a TRAFFIC device. **i**, A SEM image of the interface between alginate hydrogel and the modified thread after lyophilization. **j**, A microscopic image of a TRAFFIC device encapsulating rat islets.

4.3.2 Characterizations of the Mechanical Robustness, Mass Transfer Property and Biocompatibility

To show the mechanical robustness of the TRAFFIC device, we measured both the tensile strength of the whole device and the adhesion between the thread and the hydrogel. Compared with neat alginate hydrogel fiber, TRAFFIC exhibited drastically higher strength (Figure 4.2a). More importantly, the hydrogel-thread adhesion in TRAFFIC was also remarkably high, much higher than the device made from the non-uniform “beads-on-a-string” thread or the one made by sequential dipping of a bare suture (Figure 4.2b). We attributed the high adhesion to both the nanoporous surface structure (similar to the adhesion of water droplets to spider silks) and the macroscopic helices from the twisting of sutures. To further demonstrate the necessity of the thread reinforcement for easy handling, we compared the TRAFFIC with a neat alginate fiber. As shown in Figure 4.2c, the TRAFFIC was much more mechanically robust and easier to handle. In addition, the neat alginate fiber can clump or entangle with itself within the peritoneal cavity, jeopardizing the mass transfer or causing fibrosis (Figure 4.3). The mechanical robustness and easier handling are important advantages during implantation and retrieval.

Next, we investigated the biocompatibility of TRAFFIC. In cell encapsulation, the biocompatibility of the encapsulating material is one of the most important factors; foreign body reaction-induced fibrosis can negatively affect the mass transfer and the viability of encapsulated cells^{20, 154}. In recent years, much progress has been made on the biocompatibility of alginate materials including both purity and formulation^{46, 126}. Particularly, it has been shown that increasing the size of intraperitoneally implanted

alginate capsules from ~500 μm to ~1.5 mm reduced fibrosis⁴⁴. Inspired by these studies, we tested TRAFFIC with different thicknesses of the alginate layer in immunocompetent C57BL/6 mice and found that the thick device (overall diameter ~1.3 mm) had less cellular overgrowth than the thinner ones (~500 μm) after 2 weeks of intraperitoneal implantation (Figure 4.4). We believe this difference could be caused by many factors such as stiffness and surface area, and future work and more quantitative immunological studies are needed to elucidate the exact mechanisms. Nevertheless, encouraged by the short-term results, we further conducted longer-term studies (3 months, n=6; 7 months, n=11). In the 3-month study (Figure 4.5), while the thin devices induced variable cellular overgrowth, the thick ones had significantly less, consistent with the 2-week results. Interestingly, even after 7 months of implantation, 10 out of the 11 thick devices remained almost free of fibrosis (Figure 4.6). In the following tests of function and demonstration of scalability and retrievability, the thick device design was used.

Another factor that is critical to the function of an encapsulation device is the mass transfer property¹⁵⁵. In the TRAFFIC design, since the cells are encapsulated in alginate hydrogel that has been proven to have facile mass transfer and since all the cells are near the surface, we hypothesized that the mass transfer would be sufficient to support the cell survival and function. Indeed, experiments with human islets (Figure 4.7a, b) and several other types of cells (Figure 4.7c, d) confirmed the cell viability in *in vitro* cultures. In addition, we performed a dynamic glucose-stimulated insulin secretion (GSIS) experiment using an islet perfusion system. The islets were subjected to Krebs-Ringer bicarbonate HEPES (KRBH) buffers with low (2 mM) or high (20 mM)

glucose concentrations continuously in an alternating pattern and the secreted insulin was measured. The results showed that both the non-encapsulated and encapsulated human islets could sense the glucose concentration change and secrete insulin (Figure 4.7e). Application of 3-isobutylmethylxanthine (IBMX) and forskolin was included as a positive control and increased the insulin secretion in both cases. Although there appeared to be a delay in response for encapsulated islets, statistical analysis (see details in Methods) showed no significant difference in both total insulin secretion and the kinetics in this experiment. The facile mass transfer was probably due to the short diffusion distance (i.e. proximity of encapsulated islets to the surface). Previous studies have shown that the short diffusion distance was beneficial for not only cell survival but also glucose responsiveness^{143, 156}. We also measured the mass transfer of TRAFFIC more directly using different molecular weight, FITC-labelled dextran standards. The results indicated that the device would prevent the diffusion of molecules larger than ~250 kDa (Figure 4.8).

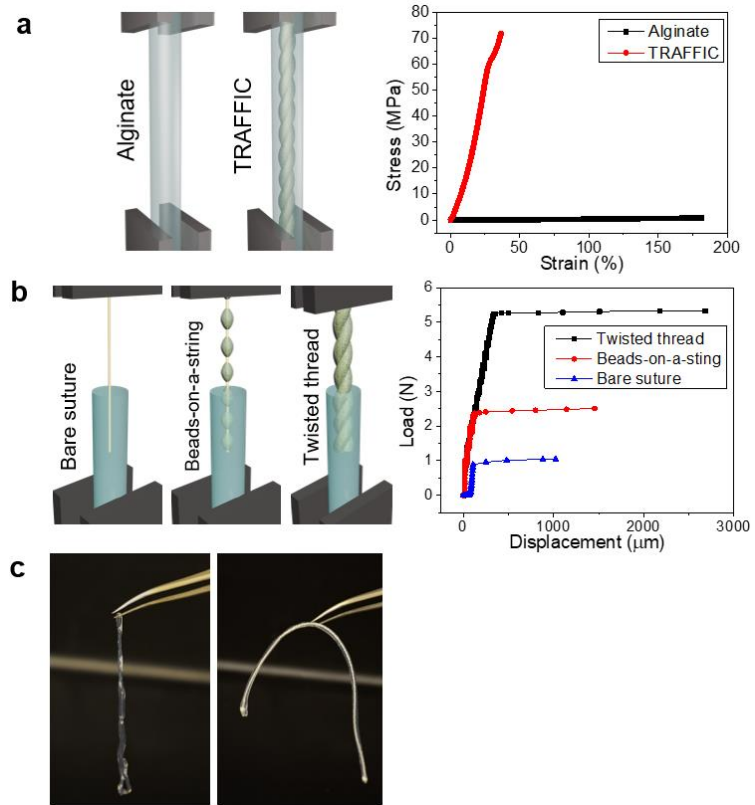


Figure 4.2. Characterizations of the mechanical robustness of TRAFFIC. **a-c**, Mechanical robustness test: strain-stress measurement (**a**), load-displacement measurement (**b**), and comparison between a neat alginate fiber and a TRAFFIC device in handling (**c**)

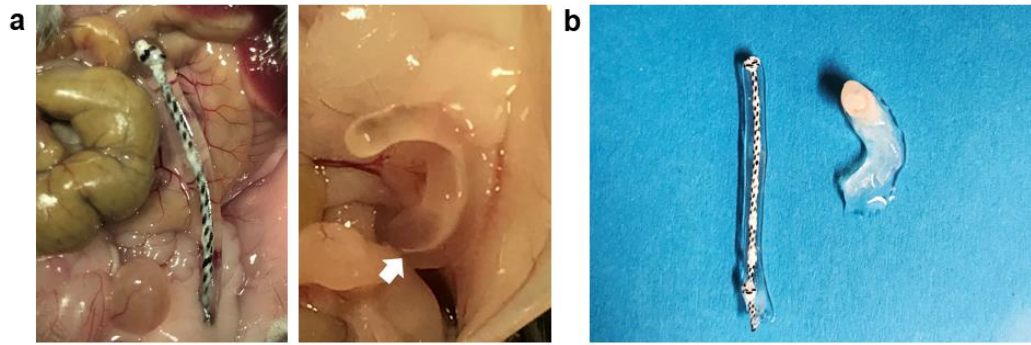


Figure 4.3. *In vivo* mechanical stability test. **a**, digital image of a TRAFFIC device (left panel) and a neat alginate hydrogel fiber (right) during retrieval, arrow indicating the entangled region. **b**, digital image of the retrieved TRAFFIC device and neat alginate hydrogel fiber.

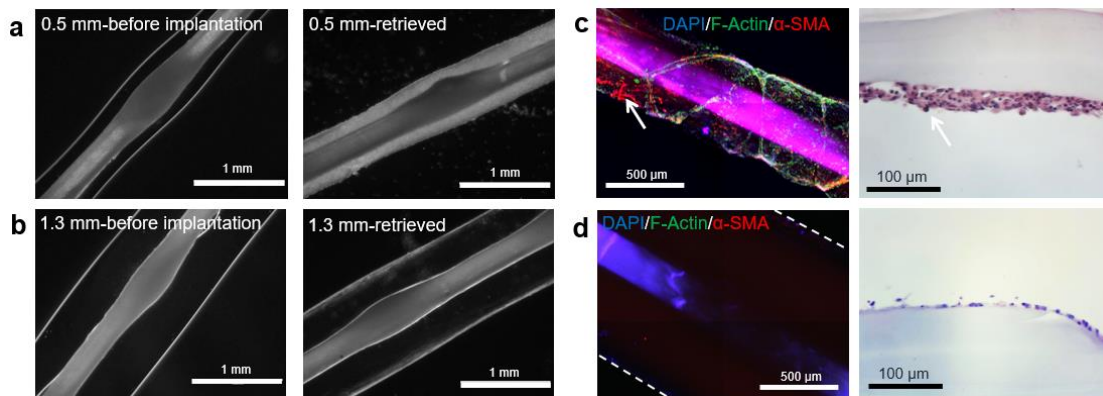


Figure 4.4. 2-week fibrosis study. **a,b**, TRAFFIC devices with diameters of 500 μm (**a**) and 1.3 mm (**b**) before and after implantation ($n=5$). **c,d**, Immunohistochemistry analysis and H&E staining of the retrieved devices with different sizes retrieved after 2 weeks: TRAFFIC with a diameter of 500 μm (**c**) and 1.3 mm (**d**) ($n=5$), cellular deposition was examined by immunostaining using DAPI (nucleus marker), F-actin (cellular cytoskeleton marker), and alpha-smooth muscle actin (α -SMA, myofibroblast marker).

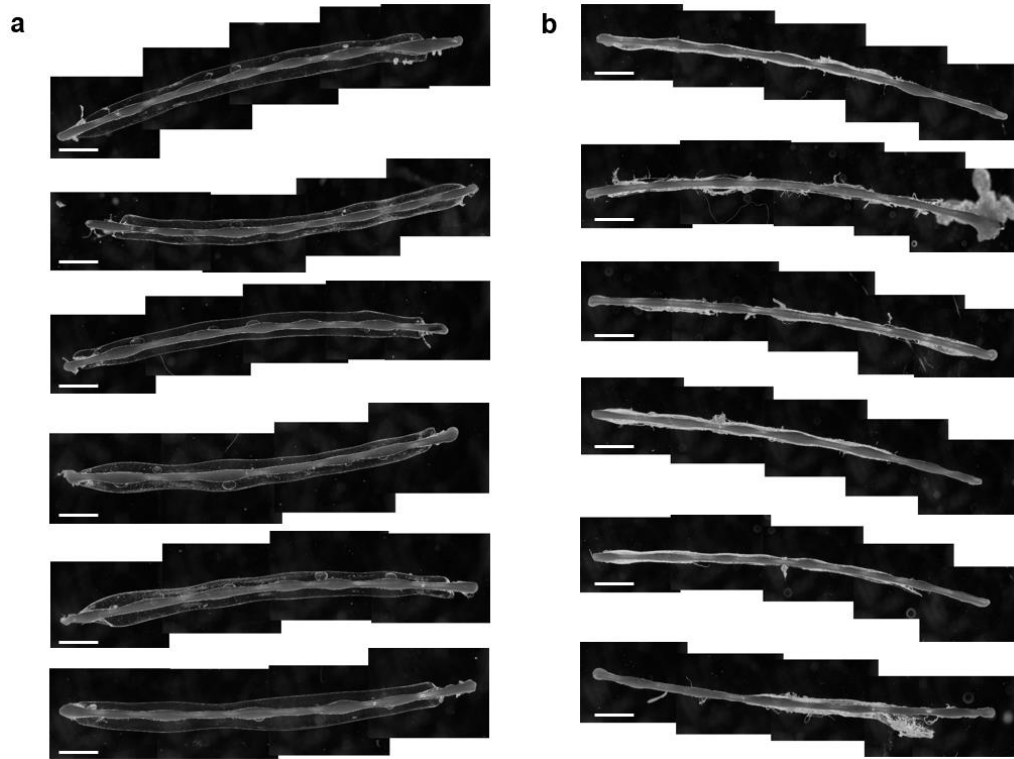


Figure 4.5. 3-month fibrosis study. Retrieved TRAFFIC devices with diameters of ~ 1.3 mm (**a**) and ~ 500 μm (**b**), all scale bars: 2mm.

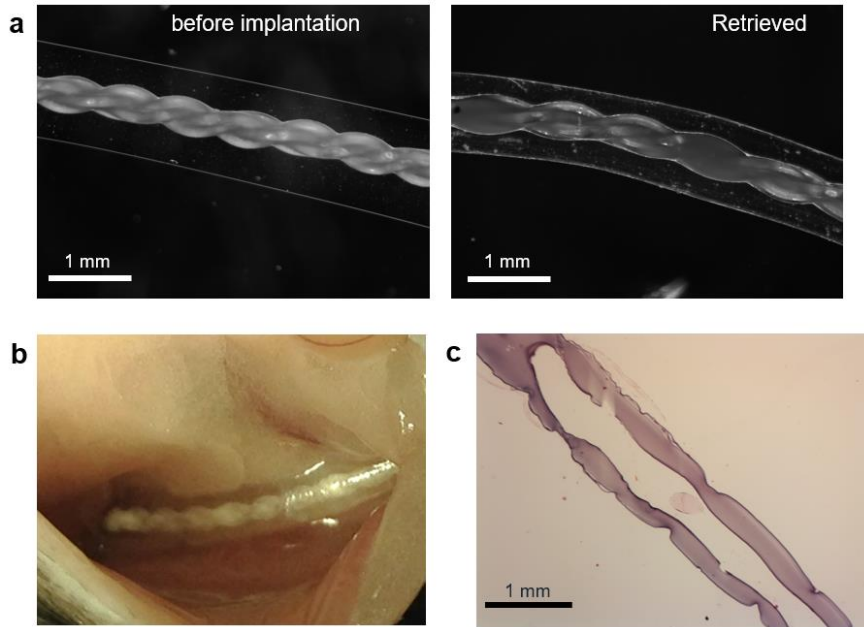


Figure 4.6. Characterizations of the biocompatibility of TRAFFIC. **a-c**, Biocompatibility characterization: Microscopic images of TRAFFIC before implantation and after 7-month implantation in mice (Note that the devices shrank slightly after being transferred into a 4% paraformaldehyde for fixation.) (a), digital photo of the device in the intraperitoneal space of a mouse during the retrieval (b), and a H&E stained image (c) of a retrieved device.

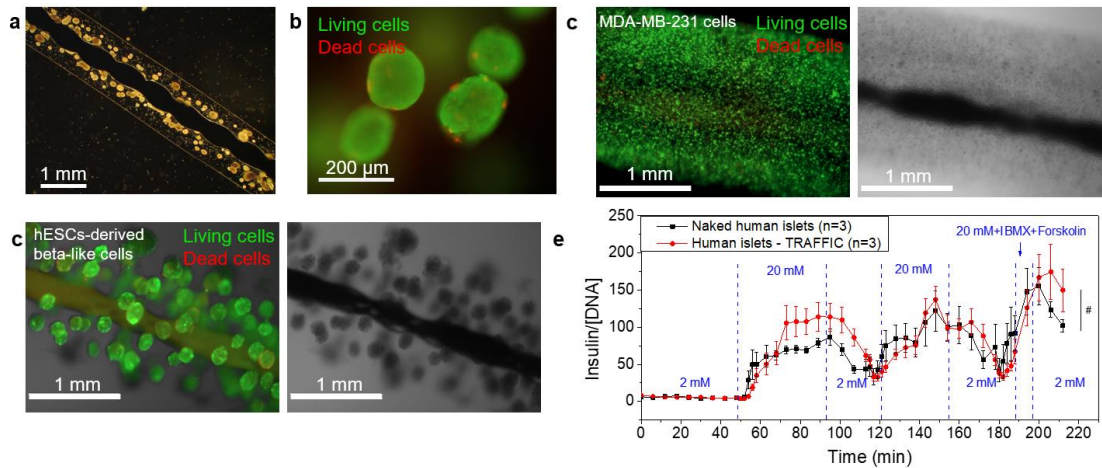


Figure 4.7. Characterizations of the mass transfer property of TRAFFIC. **a**, microscopic image of the TRAFFIC device encapsulating human islets. **b**, Live (green)/dead (red) staining of encapsulated human islets. **c**, Live (green) /dead (red) staining of MDA-MB-231 cells encapsulated in the device after a 4-day culture. **d**, Live/dead staining of aggregates of human Embryonic Stem Cell (hESC)-derived beta-like cells encapsulated in the device after a 3-day culture. **e**, the glucose-stimulated human insulin secretion in a dynamic perfusion test, n=3, mean \pm s.e.m., # $P>0.05$.

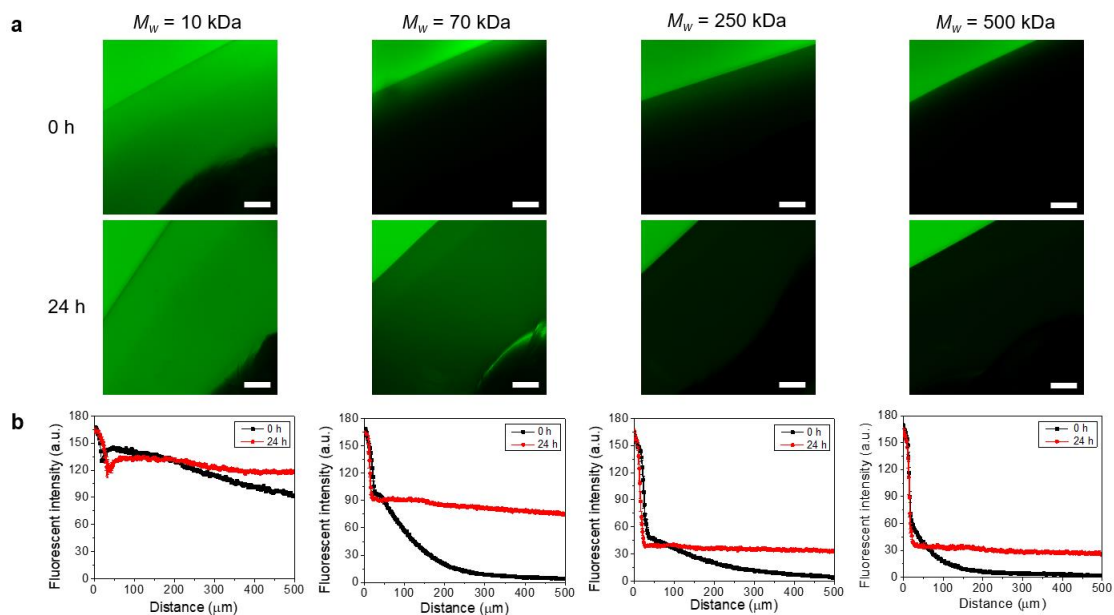


Figure 4.8. Permeability measurement of the TRAFFIC. Fluorescent images (a) and intensity profiles (b) showing the permeability of TRAFFIC devices to different molecular weight FITC-dextrans. The TRAFFIC devices were immersed in saline solutions containing FITC-dextrans with four molecular weight ($M_w=10,000$, $70,000$, $250,000$, and $500,000$), all scale bars: $100\ \mu\text{m}$.

4.3.3 Diabetes Correction in Mice

After confirming the mechanical robustness, biocompatibility, and mass transfer property of TRAFFIC, we explored its therapeutic potential. We transplanted encapsulated rat islets into the peritoneal cavity of streptozotocin (STZ)-induced C57BL/6 diabetic mice (n=10 pooled from 2 independent experiments). This “rat-to-mouse” model has been used extensively in the field and alginate hydrogel materials have been shown to be effective to protect xenografts without immunosuppression¹⁵⁷. Each diabetic mouse received a device of ~1-inch length containing $\sim 475 \pm 25$ islet equivalents (IEQ's) (Figure 4.9a)¹²¹. (Note that the cell survival post transplantation was not studied and therefore the actual, functional IEQ's inside a mouse was unknown.) The blood glucose (BG) level of the mice decreased to the normal glycemic range (BG < 200 mg/dL) 2 days after the transplantation and the mice remained cured for 4 weeks before the devices were retrieved. After retrieval, the mice returned to a diabetic state, indicating the effectiveness of the device in regulating the BG (Figure 4.9b). An intraperitoneal glucose tolerance test (IPGTT) was conducted on day 28 after transplantation, prior to retrieval. The BG increased to more than 400 mg/dL in both healthy and diabetic mice after an intraperitoneal injections of glucose solution (2g of glucose per kg body mass). The BG of the transplanted mice gradually dropped to normal range within 120 min, further confirming the function of transplanted islets (Figure 4.9c). The retrieved devices showed no tissue adhesion or significant fibrosis (Fig. 3d). *In vitro* static GSIS (Figure 4.9e) test of the retrieved devices suggested that the islets were responsive to glucose increase and secreted insulin, indicating the viability and normal function of the retrieved islets. Moreover, histological studies

(Figure 4.9f) showed minimal cellular overgrowth around the devices and normal morphology of islets with positive staining of insulin (Figure 4.9g).

In another set of 1-month transplantation experiments, we also included a control group of rat islets encapsulated in neat alginate fibers and a control group of BALB/c mouse islets encapsulated in TRAFFIC (Figure 4.10). With a similar number of rat islets ($\sim 475 \pm 25$ IEQ), TRAFFIC performed similarly to the neat alginate fiber, confirming that the modified thread in TRAFFIC had no negative effect on the therapeutic potential. The results from rat islets and BALB/c mouse islets were also similar, although we used a lower IEQ ($\sim 380 \pm 20$) for mouse islets. These control experiments confirmed the immunoprotective function of TRAFFIC for at least 1 month, similar to neat alginate fibers. However, compared to the neat alginate fibers, TRAFFIC had much more robust mechanical properties that were critical for handling, retrieval and scale-up. To examine whether TRAFFIC could have a longer-term function, we conducted two independent 3-month transplantation experiments using the rat-to-mouse model with a control group of unencapsulated rat islets transplanted in kidney capsules (in total, $n=14$ for TRAFFIC and $n=8$ for kidney capsules). For the mice with kidney capsule transplantation of unencapsulated islets, the blood glucose level was decreased briefly after transplantation, suggesting that the primary graft function was achieved. However, the transplants were rapidly rejected, all within 2 weeks. In contrast, TRAFFIC protected the islets from rejection and cured 10 out of 14 mice for at least 3 months (Figure 4.11). The normal morphology of islets retrieved from cured mice as shown by the H&E staining and the positive immunohistochemical staining of insulin and glucagon confirmed the islet function in the device (Figure 4.11d).

To further demonstrate the function of TRAFFIC, we performed more experiments in a different transplantation model using human islets. Given the large species difference between human and mouse, we chose immunodeficient SCID-Beige mice as recipients to minimize the complication of immune responses that occur in xenogeneic transplantation¹⁵⁸. We first tested the viability of encapsulated human islets (Figure 4.12a) in non-diabetic SCID-Beige mice. The devices were retrieved after one month and had minimal cell attachment and fibrosis (Figure 4.12b, c). Live/dead staining (Figure 4.12d) and *in vitro* GSIS (Figure 4.12e) of the retrieved islets indicated high viability and expected function. Next, we transplanted encapsulated human islets into STZ-induced diabetic SCID-Beige mice. We considered the mice to be diabetic when we had two consecutive measurements over 300 mg/dL which we acknowledge was a relatively low standard for diabetes. However, when we measured mouse c-peptide for the non-transplanted control groups we found that the average was 42.7 pM for the STZ-treated group (94 days after STZ treatment) and 123.2 pM for non-treated group. The c-peptide comparison in combination with the blood glucose levels indicated that the mice had lost a substantial part of the beta cell mass due to the STZ-treatment. Each STZ-treated mouse received 2 devices of ~1-inch-long containing ~1,900±100 IEQ's in total¹⁵⁹. Non-encapsulated human islets of a similar number were transplanted in kidney capsules as control. The BG and body weight were monitored over time. It took over 2 weeks after transplantation to reverse the hyperglycemia. This slow response could be due to the species difference and/or the islet quality; similarly slow BG reduction was observed previously following transplantation of human islets into kidney capsules of immunodeficient diabetic mice¹⁵⁹. However, after the initial diabetes

correction, the BG levels of the mice in both the device and kidney capsule groups were maintained within the normal range for more than 4 months until the experiment ended (Figure 4.13a). In addition, the mice in both groups gained weight after transplantation, as compared with the diabetic control group (Figure 4.13b). Immunohistochemical staining showed positive staining of human insulin, Nkx-6.1, and glucagon in the islets retrieved from both kidney capsule and TRAFFIC, similar to the islets before transplantation (Figure 4.13c). Assembled together, these data provide an important proof of concept for the use of TRAFFIC for T1D treatment.

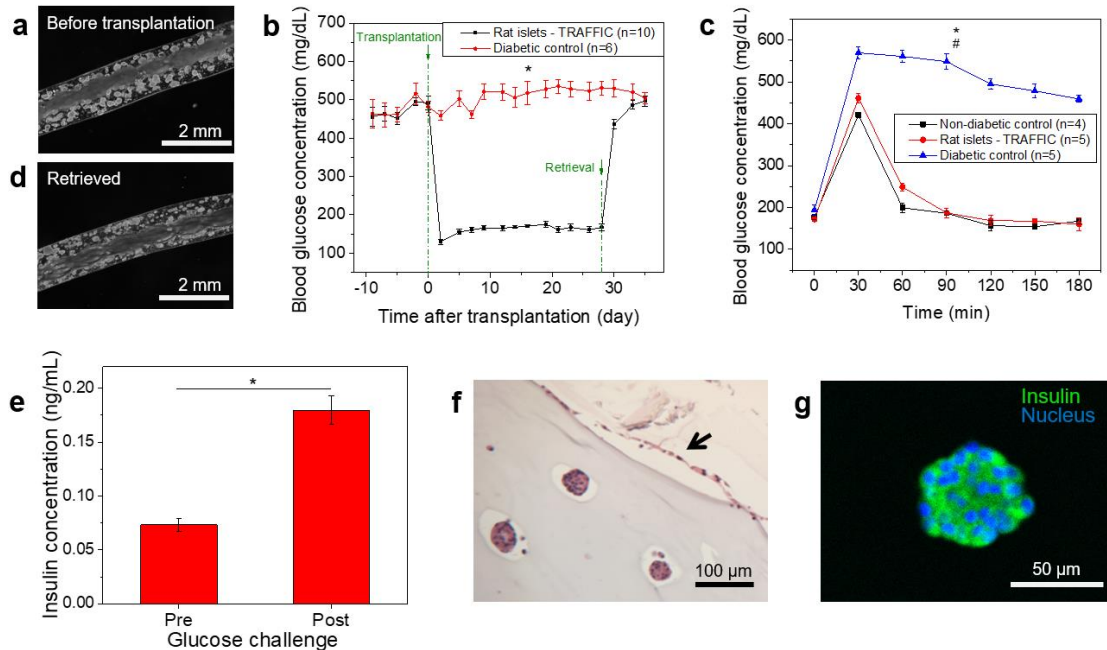


Figure 4.9. Demonstration of therapeutic potential of TRAFFIC using rat islets. **a**, Microscopic image of a TRAFFIC device encapsulating rat islets before transplantation. **b**, Blood glucose concentration of diabetic C57BL/6 mice after transplantation of encapsulated rat islets, $n=6-10$, mean \pm s.e.m., $*P < 0.05$. **c**, Intraperitoneal glucose tolerance test prior to retrieval on day 28, $n=4-5$, mean \pm s.e.m., $*P < 0.05$ (diabetic control versus rat islets - TRAFFIC), $\#P > 0.05$ (non-diabetic control versus rat islets - TRAFFIC). **d**, A microscopic image of the retrieved device. **e**, *In vitro* glucose-stimulated insulin secretion test of the retrieved rat islets, $n=3$, mean \pm s.e.m., $*P < 0.05$. **f**, H&E staining of cross-sections of retrieved islets (the arrow points to the cellular overgrowth on the device). **g**, Immunohistochemical staining of the islets in a retrieved device (green: insulin, blue: nuclei).

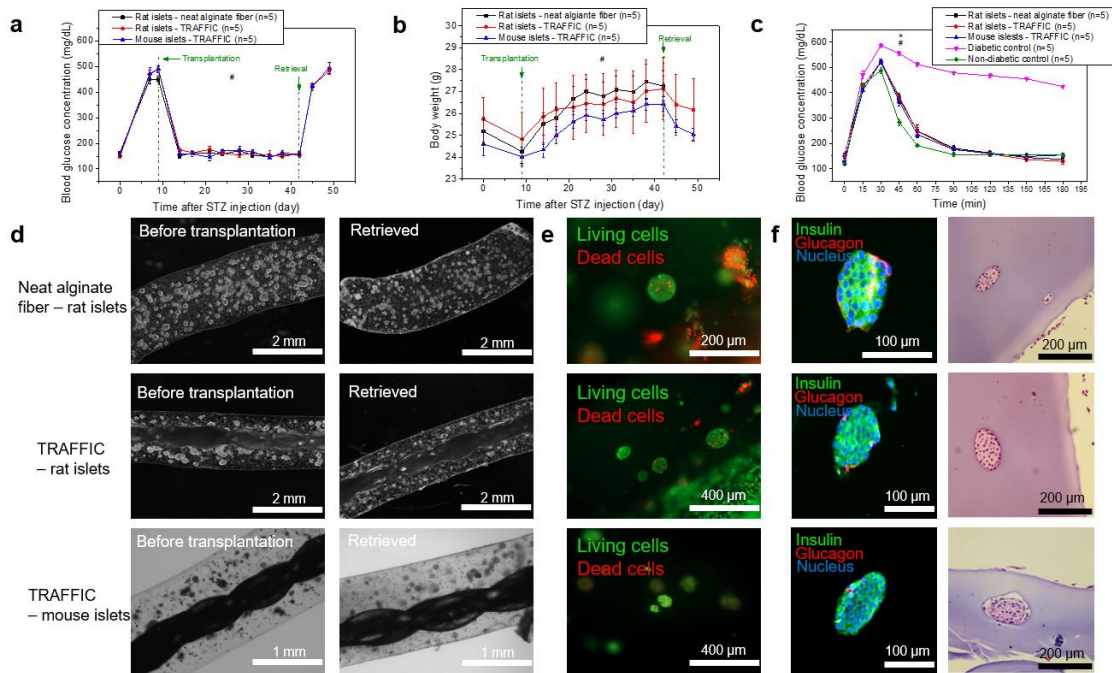


Figure 4.10. Transplantation of rat islets encapsulated in neat alginate fiber/TRAFFIC and allogenic mouse islets encapsulated with TRAFFIC. **a**, Blood glucose concentration of diabetic C57BL/6 mice after transplantation, $n=5$, $\text{mean} \pm \text{s.e.m.}$, $\#P > 0.05$ (between all three groups). **b**, Body weight of the diabetic mice after transplantation, $n=5$, $\text{mean} \pm \text{s.e.m.}$, $\#P > 0.05$ (between all three groups). **c**, Intraperitoneal glucose tolerance test prior to retrieval on day 28, $n=5$, $\text{mean} \pm \text{s.e.m.}$, $*P < 0.05$ (three groups with transplantations versus the diabetic control), $\#P > 0.05$ (among the three groups with transplantations). **d**, Optical microscope images of the device/islets before transplantation and after retrieval. **e**, Live/dead staining of the retrieved islets. **f**, Immunohistochemical staining and H&E staining of the retrieved islets.

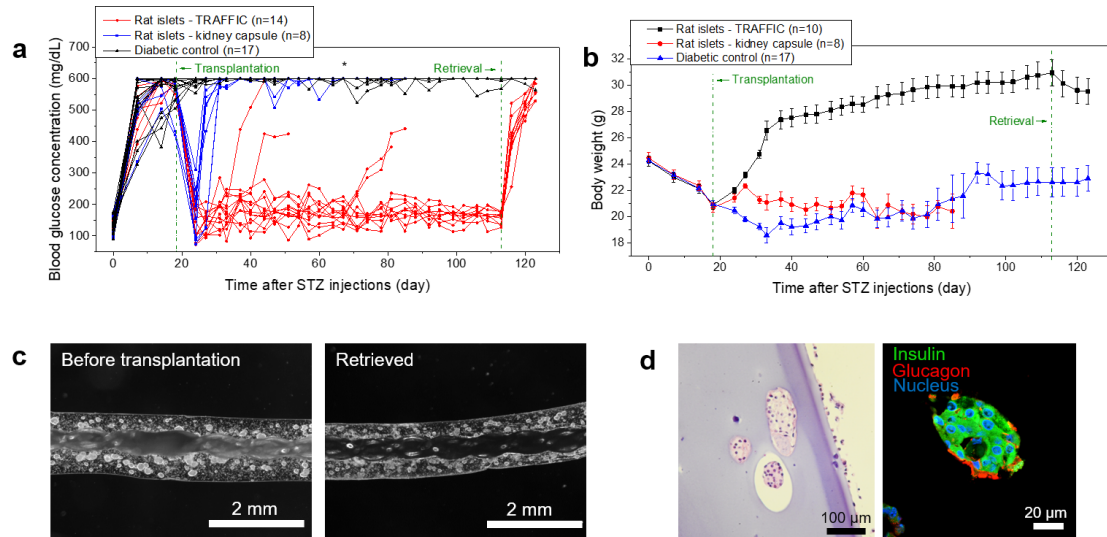


Figure 4.11. Long-term study of the transplantation of the rat islet encapsulated in TRAFFIC. **a**, Blood glucose concentrations of mice from 3-month transplantation studies, n=8-17, mean±s.e.m., *P<0.05 (diabetic control versus rat islets - TRAFFIC). **b**, Body weight of the C57BL/6 diabetic mice that received transplantation of rat islets. **c**, Optical microscopic images of the rat islets in TRAFFIC before transplantation and retrieved after 3 months. **d**, H&E staining and immunohistochemical staining of retrieved islets in TRAFFIC.

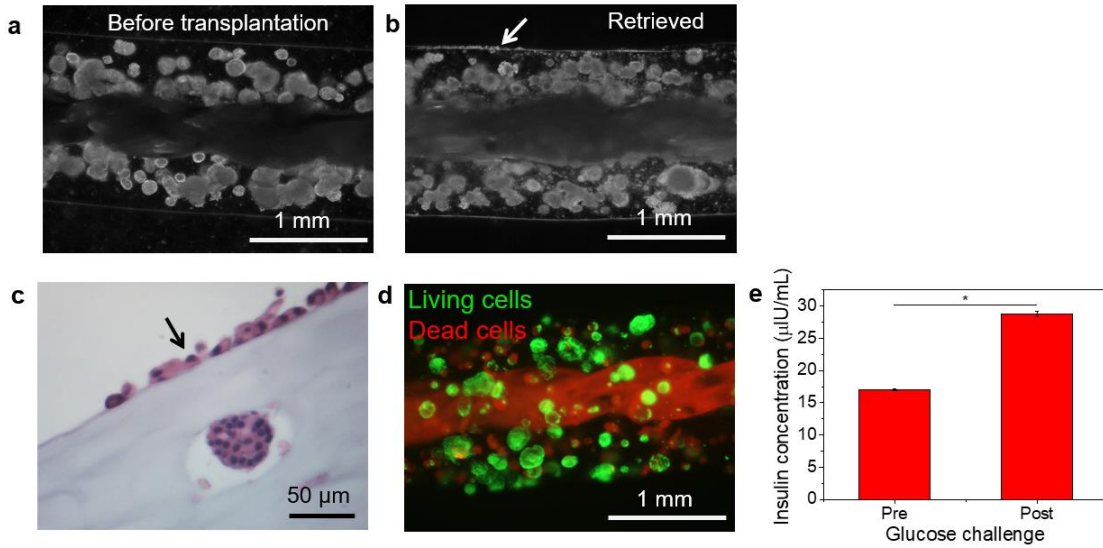


Figure 4.12. Transplantation of human islets encapsulated in TRAFFIC into healthy mice. **a**, Microscopic image of a TRAFFIC device with encapsulated human islets before transplantation. **b**, Microscopic image of a TRAFFIC device retrieved after 1 month. **c**, H&E staining of a cross-section of the device (the arrow points to the minimal cellular overgrowth on the device). **d**, Live (green)/dead (red) staining of human islets in retrieved device. **e**, *In vitro* glucose-stimulated insulin secretion test of human islets in retrieved device, $n=3$, mean \pm s.e.m., $*P<0.05$.

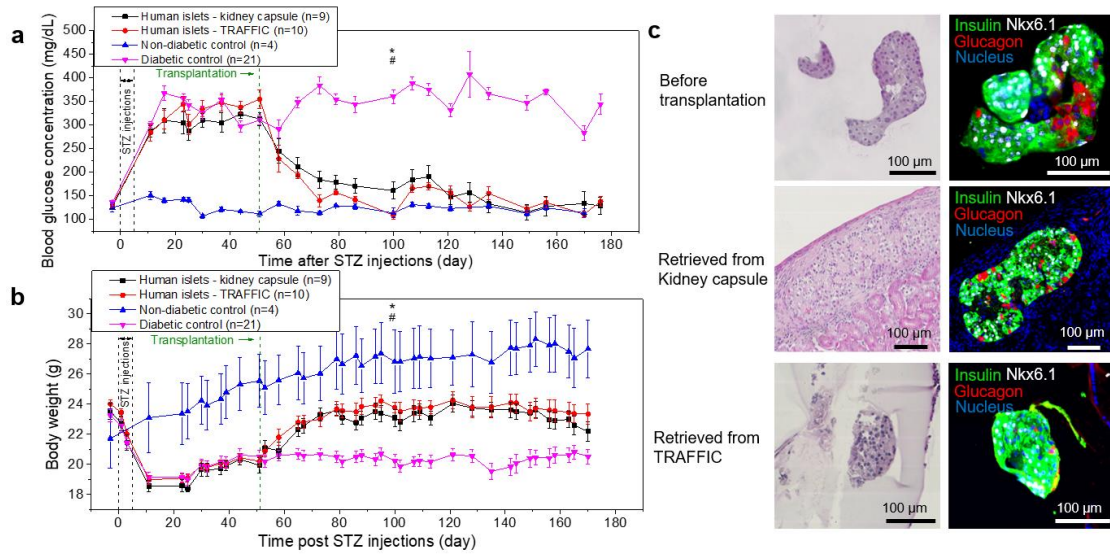


Figure 4.13. Demonstration of therapeutic potential of TRAFFIC using human islets. **a**, Blood glucose concentrations of diabetic SCID-Beige mice after transplantation of human islets, n=4-21, mean \pm s.e.m., * $P < 0.05$ (human islets – TRAFFIC versus diabetic control), # $P > 0.05$ (human islets – kidney capsule versus human islets - TRAFFIC). **b**, Body weights of the mice after transplantation. n=4-21, mean \pm s.e.m., * $P < 0.05$ (human islets – TRAFFIC versus diabetic control), # $P > 0.05$ (human islets – kidney capsule versus human islets - TRAFFIC). **c**, H&E staining and immunohistochemical staining of human islets before transplantation and retrieved from kidney capsules or TRAFFIC.

4.3.4 Scale-up and Test of Retrievability in Dogs

Two important advantages of the TRAFFIC design are scalability and retrievability. It is estimated that 500,000 IEQ's may be needed to cure a human T1D patient⁷³. To deliver such a large number of islets, scalability is critical to any successful cell encapsulation system. Due to the thin cylindrical geometry, TRAFFIC can be scaled up in the longitudinal direction to a large capacity and can still be retrieved through minimally invasive laparoscopic procedures. To prove this concept, we fabricated ~10-inch TRAFFIC devices using a custom-made thread holder and a channel reservoir (Figure 4.14a, b). Next, we performed some large animal experiments using dogs. In an initial pilot experiment, a ~1.5 mm diameter, 10-inch-long device (without cells) made from the "beads-on-a-string" thread (Figure 4.14b) was laparoscopically implanted into each of two dogs. The procedure was relatively simple and fast. Briefly, the device was placed in a pipette, which was then inserted through a laparoscopic trocar (Figure 4.14c, d). Under the laparoscopic visualization, the device was pulled into the peritoneal cavity using laparoscopic forceps (Figure 4.14c, left) and placed in the cranial abdomen near the liver. Two weeks later, the device was retrieved by grasping and pulling the device using a similar laparoscopic procedure (Figure 4.14c, right). In one dog, minor tissue adhesion occurred between the omentum and a segment of the device in which the hydrogel had detached and the thread was exposed (Figure 4.15). However, the device was still retrievable in its entirety after excising the adhered tissue. In the other dog, there was no adhesion or any gross fibrosis on the device (Figure 4.14e, f). Remarkably, even though the device left an indentation on the liver (Figure 4.14e), there was no fibrosis or histologic indication of inflammation in the tissue (Figure 4.14g). In both

dogs, there were no significant changes in bloodwork (i.e. fibrinogen concentration, white blood cell count, liver enzyme concentrations) suggesting that no inflammation was induced.

Although this first pilot experiment was promising, comparison of the results from the two dogs highlighted the importance of the thread design to ensure strong hydrogel-thread adhesion. To overcome the hydrogel detaching problem that occurred in one of the dogs, we repeated the implantation experiment with 3 more dogs using a device (diameter of ~2 mm) made from the continuously modified, twist-folded thread. One dog was implanted with an empty device while the other two were implanted with devices encapsulating sub-therapeutic doses of rat islets (~1,000 IEQ's /device). The devices were retrieved after 1 month. All three devices remained intact and no tissue adhesion occurred. To illustrate the convenient retrieval, we took videos both inside and outside the dog (Figure 4.16a, b). The retrieval was simple and rapid; it took merely 10 seconds from grasping the device to removal. The retrieved devices had only thin layers of attached cells (Figure 4.16c, d). The xenogeneic rat islets induced some local inflammation, however, there was no tissue adhesion and the devices were still easily retrievable. More importantly, the islets in retrieved devices were still viable and functional, as evidenced by live/dead staining (Figure 4.16e), insulin staining of cross-sectioned islets (Figure 4.16f) and *in vitro* GSIS (Figure 4.16g).

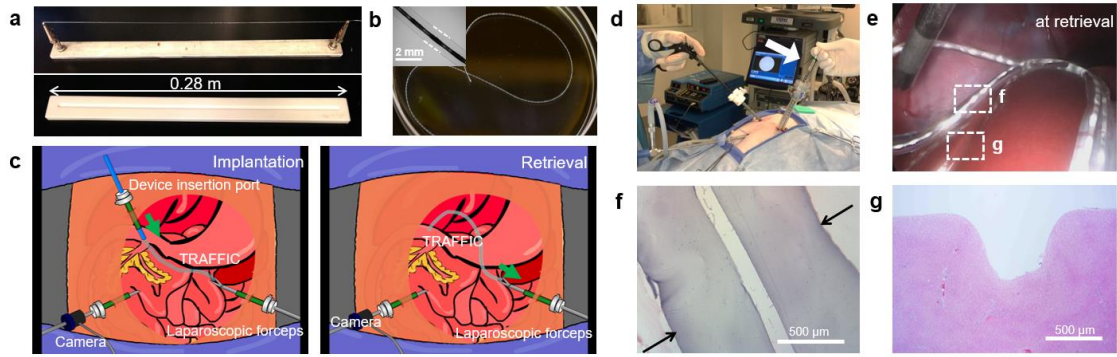


Figure 4.14. Scalability of TRAFFIC and laparoscopic retrieval. **a**, A digital image of custom-made tools for fabrication of long TRAFFIC. **b**, A digital image of a ~10-inch-long empty device for canine implantation, inset: a microscopic image of the device. **c**, **d**, Schematic illustrations and a digital image showing the laparoscopic procedures; the arrow in (**d**) indicates the insertion of the device into a dog during intraperitoneal implantation. **e**, Laparoscopic image of the device 2 weeks after implantation. **f**, H&E staining of the retrieved device. **g**, H&E staining of the liver tissue in contact with the device.

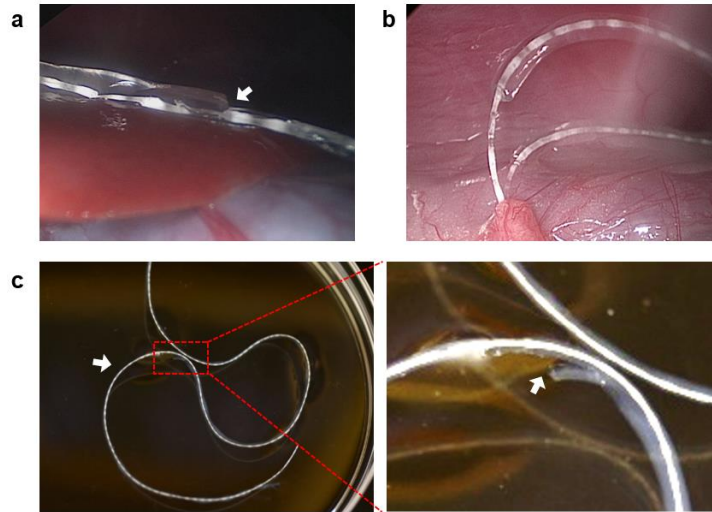


Figure 4.15. Weak mechanical stability of the device made from a “beads-on-a-string” thread. **a**, A laparoscopic image showing the alginate hydrogel partially detached in the peritoneal space of a dog. **b**, Laparoscopic image showing tissue adhesion of the exposed thread where the alginate hydrogel detached. **c**, Digital images showing a detached part of the retrieved device.

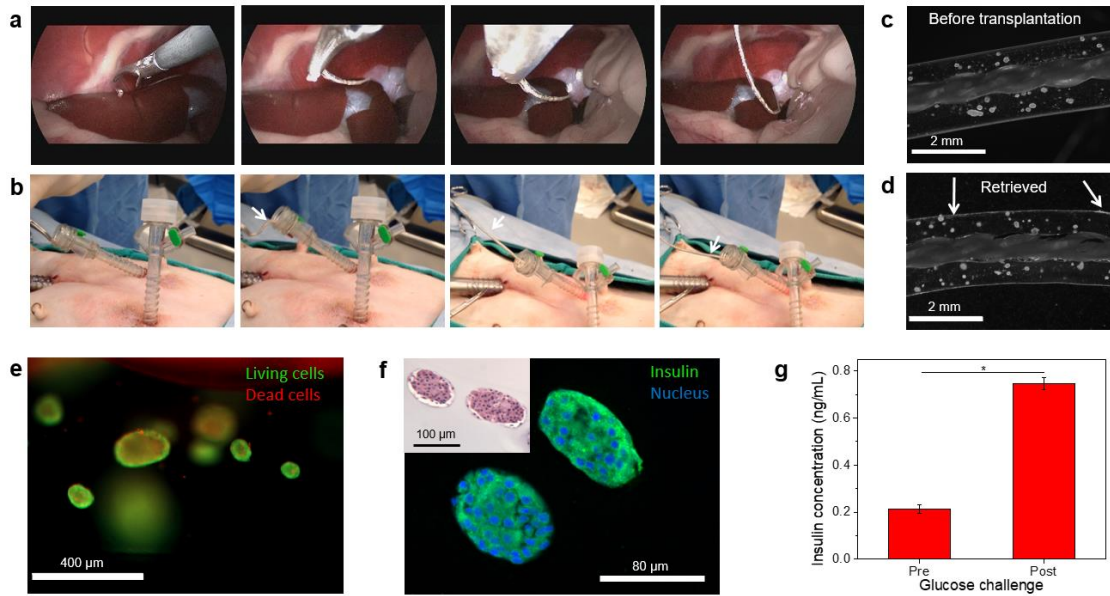


Figure 4.16. Demonstration of rapid device retrieval and cell survival in a dog model. **a**, A series of laparoscopic images showing the retrieval process. **b**, A series of digital images showing the device being pulled out from a trocar. **c, d**, Microscopic images of the device with encapsulated rat islets before (**c**) and after (**d**) transplantation in dogs (the arrow points to the minimal cellular overgrowth on the device). **e**, Live/dead staining of retrieved rat islets. **f**, Insulin staining of retrieved islets. inset: H&E staining. **g**, *In vitro* glucose-stimulated insulin secretion, $n=3$, mean \pm s.e.m., $*P<0.05$.

4.3.5 Discussion

Recent development of stem cell biology has brought tremendous hope that one-day human stem cells may be differentiated into functional beta-like cells and transplanted into T1D patients^{17, 160}. However, to prevent immune and autoimmune attack, the exogenous cells need to be encapsulated or immuno-protected. Developing an encapsulation system that can be clinically used has unfortunately been a great challenge^{4, 103}. Planar diffusion chambers such as the Viacyte® device have shown great promise in preclinical small animal studies¹⁶¹. However, there are considerable challenges to scale up the device to human patients due to the intrinsically low surface area for mass transfer; high cell packing density may lead to deficiency of oxygen and nutrients^{142, 143, 162}. The other major type of encapsulation system is the hydrogel capsule. Hydrogel capsules have a larger surface area and can potentially deliver a higher number of islets^{4, 44, 141, 162}. Importantly much progress has been made recently on the biocompatibility of alginate hydrogels^{46, 154}, which makes the capsules more functionally durable and easier to retrieve. However, common retrieval techniques such as aspiration and lavage are time-consuming and it is a great challenge to ensure complete retrieval given the large capsule number and the complicated organ structures inside the peritoneal space^{52, 163, 164}. Incomplete retrieval can cause serious safety concerns when stem cell-derived cells are used due to the potential of teratoma formation^{4, 12}.

4.4 Conclusion

In this work, we report a new encapsulation design that takes advantages of alginate hydrogel and is both scalable and retrievable. The key to the design is a tough

central thread with continuous nanoporous modification and uniform Ca^{2+} -release. The device is in contrast to conventional neat hydrogel fibers which although previously proposed for cell encapsulation^{98, 104, 165, 166}, were soft and easy to break and therefore not suited for clinical applications. The uniform and controllable hydrogel thickness as well as the strong thread-hydrogel adhesion are both important for function and translation. Convenient retrieval with a minimally invasive surgery would be particularly attractive for clinical applications. For any transplantation, straightforward removal after completion of therapy or failure of transplant would address patients' concerns of having foreign materials and cells permanently implanted in the body^{56, 103}. As therapeutic cells derived from stem cells or adult cells become a potential alternative to primary cells, retrievability is more highly desired to mitigate the concerns of teratoma formation¹². We believe this new encapsulation design will minimize the risks and discomfort associated with transplantation, make repeated transplantation a more acceptable option, and therefore likely accelerate and contribute to the translation of cell encapsulation for T1D and potentially many other diseases. Furthermore, our modified thread device could be available to researchers or clinicians as an off-the-shelf, ready-to-use product and cell encapsulation may be performed at site via a one-step *in situ* crosslinking.

CHAPTER 5: CONCLUSION AND FUTURE PERSPECTIVE

5.1 Conclusion

Mass transport property is a significant factor that determines the success of any cell encapsulation system. In microencapsulation systems, spherical hydrogel microparticles, typically with a diameter of 500-600 μm , are the most commonly used and widely studied materials. Recent studies have shown that it is actually more desirable to use larger size particles (about 1.5 mm or larger in diameter) for cell delivery, since larger particles generate less foreign body responses upon implantation. However, when increasing the overall size of the hydrogel particles, the diffusion distance within the hydrogel is also increased. Thus, mass transfer becomes a problem. For instance, the cells in the center of the sphere can experience the lack of nutrients and oxygen. Therefore, to address this dilemma, I developed a novel fabrication platform for preparing non-spherical particles. By combining the ubiquitous vortex ring phenomenon with rationally designed freezing events, I was able to produce toroidal shaped hydrogel particles in large scale. Compared to conventional spherical hydrogel particles, the toroidal ones have a shorter diffusion distance within, a better deformability and a larger surface/volume ratio. These advantages greatly facilitate the mass transport property of the hydrogel particle-based cell encapsulation system.

Besides mass transport property, good mechanical stability is another very important property affecting the effectiveness and usefulness of cell encapsulation devices. Here, I firstly engineered a nanofiber enabled hydrogel encapsulation device (NEED). In this design, I took advantage of the well-known capillary action that holds

wetting liquid in porous media. By impregnating the highly porous electrospun nanofiber membrane of pre-made tubular or planar devices with hydrogel precursor solutions and subsequent crosslinking, I obtained various nanofiber-enabled hydrogel devices. This approach is broadly applicable and does not alter the water content or the intrinsic chemistry of the hydrogels. The device takes advantages of the properties of both the hydrogel (e.g. the biocompatibility) and the nanofiber (e.g. the mechanical robustness). The facile mass transfer was confirmed by encapsulation and culture of different types of cells. Additional compartmentalization of the devices enabled paracrine cell co-culture in single implantable devices. Lastly, I provided a proof-of-concept study on potential therapeutic applications of the devices by encapsulating and delivering rat pancreatic islets into chemically-induced diabetic mice. The diabetes was corrected for the duration of the experiment (8 weeks) before the implants were retrieved. The retrieved devices showed minimal fibrosis and as expected, live and functional islets were observed within the device. This study suggests that the design concept of NEEDs may potentially help to overcome some of the challenges in the cell encapsulation field and therefore contribute to the development of cell therapies in future.

Besides the properties and problems mentioned above about the cell encapsulation systems, challenges still remain for clinical applications. For example, there is an unmet need for an encapsulation system that is capable of delivering sufficient cell mass while still allowing convenient retrieval or replacement. Therefore, I report a simple cell encapsulation design that is readily scalable and conveniently retrievable. The key to this design was to engineer a highly wettable, Ca^{2+} -releasing

nanoporous polymer thread that promoted uniform *in situ* cross-linking and strong adhesion of a thin layer of alginate hydrogel around the thread. The device provided immunoprotection of rat islets in immunocompetent C57Bl/6 mice in a short-term (1-month) study, similar to neat alginate fibers. However, the mechanical property of the device, critical for handling and retrieval, was much more robust than the neat alginate fibers due to the reinforcement of the central thread. It also had facile mass transfer due to the short diffusion distance. We demonstrated the therapeutic potential of the device through the correction of chemically induced diabetes in C57BL/6 mice using rat islets for 3 months as well as in immunodeficient SCID-Beige mice using human islets for 4 months. We further showed, as a proof of concept, the scalability and retrievability in dog, the device could be rapidly retrieved through a minimally invasive laparoscopic procedure. This encapsulation device may contribute to a cellular therapy for T1D because of its retrievability and scale-up potential.

In conclusion, the works presented in this dissertation focused on improving several crucial properties of both microencapsulation and macroencapsulation systems. Several solutions were proposed and tested in order to overcome the challenges discussed above, and they will contribute to a cellular therapy for T1D and potentially other endocrine disorders and hormone-deficient disease.

5.2 Future perspective

With a world diabetes prevalence of over 300 million and an estimated increase to over 500 million in 20 years, there is an urgent need for therapy. It is reasonable to envision that the cure of diabetes will rely on the combination of pharmacological and cell-based treatment. Islet transplantation represents a potential cure for T1D. However,

its wide use has been limited by insufficient long-term success, the risks associated with immunosuppression and donor organ shortage. Islets encapsulation is a fast emerging field which attempts to overcome these obstacles by transplanting islets without immunoisolation and provide the safe usage of other cell sources.

With the recent advances of stem cell research, stem cells become a very attractive alternative and theoretically unlimited cell source for transplantation. Recent reports on the generation of insulin-producing cells from human embryonic stem cells (hESCs) showed great promise. The Melton¹⁶⁰ and Hebrok¹⁶⁷ laboratories reported a culture system for generating insulin-producing cells from hESCs that can normalize hyperglycaemia in diabetic mice. Furthermore, encapsulation of these hESCs-derived immature β -cells within alginate hydrogel microcapsules and transplantation into immune-competent diabetic mice established euglycaemia that persisted for 25 weeks without any immunosuppression⁴⁶. Even though many promising results have been reported, challenges and concerns still exist. For instance, the material requirements for the transplantation of adult islets may differ relative to the systems for the transplantation of neonatal or progenitor cells. Moreover, the potential for immature cells or un-differentiated cells within the transplant may cause concerns that should be addressed.

BIBLIOGRAPHY

1. Amer Diabet, A. Diagnosis and Classification of Diabetes Mellitus. *Diabetes Care* **32**, S62-S67 (2009).
2. Dabelea, D. Incidence of diabetes in youth in the United States. *J. Am. Med. Assoc.* **298**, 627-627 (2007).
3. Jarosz-Chobot, P. et al. Rapid increase in the incidence of type 1 diabetes in Polish children from 1989 to 2004, and predictions for 2010 to 2025. *Diabetologia* **54**, 508-515 (2011).
4. Desai, T. & Shea, L.D. Advances In islet encapsulation technologies. *Nat. Rev. Drug Discov.* **16**, 338-350 (2017).
5. Shamoon, H. et al. The effect of intensive treatment of diabetes on the development and progression of long-term complications in insulin-dependent diabetes mellitus. *N. Engl. J. Med.* **329**, 977-986 (1993).
6. Ryan, E.A. et al. Five-year follow-up after clinical islet transplantation. *Diabetes* **54**, 2060-2069 (2005).
7. Barton, F.B. et al. Improvement in Outcomes of Clinical Islet Transplantation: 1999-2010. *Diabetes Care* **35**, 1436-1445 (2012).
8. Melssen, M.C. The SAGE Encyclopedia of Stem Cell Research, 2nd edition. *Ref. User Serv. Q.* **55**, 254-254 (2016).
9. Meyer, E.H., DeKruyff, R.H., Iliopoulou, P., Hsu, Y. & Cruz, M.P. BLOCKADE OF RGMb FOR REDUCING TRANSPLANTATION-ASSOCIATED IMMUNE RESPONSES. *US patent US20170121404A1* (2016).

10. Holmes-Walker, D.J. & Kay, T.W.H. Long-term effects of islet transplantation. *Curr. Opin. Organ Transpl.* **21**, 497-502 (2016).
11. Abboudi, H. & MacPhee, I.A. Individualized immunosuppression in transplant patients: potential role of pharmacogenetics. *Pharmgenomics Pers. Med.* **5**, 63 (2012).
12. Hentze, H. et al. Teratoma formation by human embryonic stem cells: Evaluation of essential parameters for future safety studies. *Stem Cell Res.* **2**, 198-210 (2009).
13. Bisceglie, V. Über die antineoplastische Immunität. *Zeitschrift für Krebsforschung* **40**, 122-140 (1934).
14. Algire, G.H. & Legallais, F.Y. Recent developments in the transparent-chamber technique as adapted to the mouse. *J. Natl. Cancer Inst.* **10**, 225-253 (1949).
15. Algire, G.H., Weaver, J.M. & Prehn, R.T. Growth of Cells In Vivo in Diffusion Chambers. I. Survival of Homografts in Immunized Mice. *J. Natl. Cancer Inst.* **15**, 493-507 (1954).
16. Prehn, R.T., Weaver, J.M. & Algire, G.H. The diffusion-chamber technique applied to a study of the nature of homograft resistance. *J. Natl. Cancer Inst.* **15**, 509-517 (1954).
17. Millman, J.R. et al. Generation of stem cell-derived β -cells from patients with type 1 diabetes. *Nat. Commun.* **7**, 11463 (2016).
18. Pagliuca, F.W. et al. Generation of Functional Human Pancreatic beta Cells In Vitro. *Cell* **159**, 428-439 (2014).
19. Reznika, A. et al. Reversal of diabetes with insulin-producing cells derived in

- vitro from human pluripotent stem cells. *Nat. Biotechnol.* **32**, 1121-1133 (2014).
20. Krishnan, R., Alexander, M., Robles, L., Foster 3rd, C.E. & Lakey, J.R. Islet and stem cell encapsulation for clinical transplantation. *Rev. Diabet. Stud.* **11**, 84 (2014).
 21. US National Library of Medicine. *ClinicalTrials.gov* <https://clinicaltrials.gov/ct2/show/NCT01652911> (2016).
 22. US National Library of Medicine. *ClinicalTrials.gov* <https://clinicaltrials.gov/ct2/show/NCT01739829> (2014).
 23. US National Library of Medicine. *ClinicalTrials.gov* <https://clinicaltrials.gov/ct2/show/NCT00790257> (2016).
 24. US National Library of Medicine. *ClinicalTrials.gov* <https://clinicaltrials.gov/ct2/show/NCT01379729> (2013).
 25. US National Library of Medicine. *ClinicalTrials.gov* <https://clinicaltrials.gov/ct2/show/NCT02239354> (2015).
 26. US National Library of Medicine. *ClinicalTrials.gov* <https://clinicaltrials.gov/ct2/show/NCT02064309> (2016).
 27. US National Library of Medicine. *ClinicalTrials.gov* <https://clinicaltrials.gov/ct2/show/NCT02213003> (2016).
 28. Uludag, H., De Vos, P. & Tresco, P.A. Technology of mammalian cell encapsulation. *Adv. Drug Deliv. Rev.* **42**, 29-64 (2000).
 29. Merani, S., Toso, C., Emamaullee, J. & Shapiro, A. Optimal implantation site for pancreatic islet transplantation. *Br. J. Surg.* **95**, 1449-1461 (2008).
 30. Chang, T.M. Semipermeable microcapsules. *Science* **146**, 524-525 (1964).

31. Lim, F. & Sun, A.M. Microencapsulated islets as bioartificial endocrine pancreas. *Science* **210**, 908-910 (1980).
32. O'Shea, G.M., Goosen, M.F. & Sun, A.M. Prolonged survival of transplanted islets of Langerhans encapsulated in a biocompatible membrane. *Biochim. Biophys. Acta-Mol. Cell Res.* **804**, 133-136 (1984).
33. Pedraz, J.L. & Orive, G. Therapeutic applications of cell microencapsulation, Vol. 670. (Springer Science & Business Media, 2010).
34. Teramura, Y. & Iwata, H. Bioartificial pancreas: microencapsulation and conformal coating of islet of Langerhans. *Adv. Drug Deliv. Rev.* **62**, 827-840 (2010).
35. Grainger, D.W. All charged up about implanted biomaterials. *Nat. Biotechnol.* **31**, 507-509 (2013).
36. De Vos, P., Hamel, A. & Tatarkiewicz, K. Considerations for successful transplantation of encapsulated pancreatic islets. *Diabetologia* **45**, 159-173 (2002).
37. De Vos, P., De Haan, B., Wolters, G.H. & Van Schilfgaarde, R. Factors influencing the adequacy of microencapsulation of rat pancreatic islets. *Transplantation* **62**, 888-893 (1996).
38. De Vos, P., De Haan, B. & Van Schilfgaarde, R. Effect of the alginate composition on the biocompatibility of alginate-polylysine microcapsules. *Biomaterials* **18**, 273-278 (1997).
39. Strand, B.L. et al. Poly-L-lysine induces fibrosis on alginate microcapsules via the induction of cytokines. *Cell transplantation* **10**, 263-275 (2001).

40. Tomei, A.A. et al. Device design and materials optimization of conformal coating for islets of Langerhans. *Proc. Natl. Acad. Sci. U.S.A.* **111**, 10514-10519 (2014).
41. Gattás-Asfura, K.M. & Stabler, C.L. Bioorthogonal layer-by-layer encapsulation of pancreatic islets via hyperbranched polymers. *ACS Appl. Mater. Interfaces* **5**, 9964-9974 (2013).
42. Wilson, J.T. et al. Cell surface engineering with polyelectrolyte multilayer thin films. *J. Am. Chem. Soc.* **133**, 7054-7064 (2011).
43. Rabanel, J.M., Banquy, X., Zouaoui, H., Mokhtar, M. & Hildgen, P. Progress technology in microencapsulation methods for cell therapy. *Biotechnol. Prog.* **25**, 946-963 (2009).
44. Veisheh, O. et al. Size- and shape-dependent foreign body immune response to materials implanted in rodents and non-human primates. *Nat. Mater.* **14**, 643-651 (2015).
45. Vegas, A.J. et al. Combinatorial hydrogel library enables identification of materials that mitigate the foreign body response in primates. *Nat. Biotechnol.* **34**, 345-352 (2016).
46. Vegas, A.J. et al. Long-term glycemic control using polymer-encapsulated human stem cell-derived beta cells in immune-competent mice. *Nat. Med.* **22**, 306-311 (2016).
47. Knazek, R.A., Gullino, P.M., Kohler, P.O. & Dedrick, R.L. Cell culture on artificial capillaries: an approach to tissue growth in vitro. *Science* **178**, 65-67 (1972).

48. Chick, W.L., Like, A.A. & Lauris, V. Beta cell culture on synthetic capillaries: an artificial endocrine pancreas. *Science* **187**, 847-849 (1975).
49. Sun, A.M., Parisius, W., Healy, G.M., Vacek, I. & Macmorine, H.G. The use, in diabetic rats and monkeys, of artificial capillary units containing cultured islets of Langerhans (artificial endocrine pancreas). *Diabetes* **26**, 1136-1139 (1977).
50. Maki, T. et al. Treatment of severe diabetes mellitus for more than one year using a vascularized hybrid artificial pancreas. *Transplantation* **55**, 713-717 (1993).
51. Weaver, J., Algire, G. & Prehn, R. The growth of cells in vivo in diffusion chambers. II. The role of cells in the destruction of homografts in mice. *J. Natl. Cancer Inst.* **15**, 1737-1767 (1955).
52. Scharp, D.W. & Marchetti, P. Encapsulated islets for diabetes therapy: history, current progress, and critical issues requiring solution. *Adv. Drug Deliv. Rev.* **67**, 35-73 (2014).
53. Brauker, J., Martinson, L.A., Young, S.K. & Johnson, R.C. Local inflammatory response around diffusion chambers containing xenografts: nonspecific destruction of tissues and decreased local vascularization. *Transplantation* **61**, 1671-1677 (1996).
54. Brauker, J.H. et al. Neovascularization of synthetic membranes directed by membrane microarchitecture. *J. Biomed. Mater. Res. B* **29**, 1517-1524 (1995).
55. Pepper, A.R. et al. Diabetes is reversed in a murine model by marginal mass syngeneic islet transplantation using a subcutaneous cell pouch device. *Transplantation* **99**, 2294 (2015).

56. Pepper, A.R. et al. A prevascularized subcutaneous device-less site for islet and cellular transplantation. *Nat. Biotechnol.* **33**, 518-523 (2015).
57. Pedraza, E., Coronel, M.M., Fraker, C.A., Ricordi, C. & Stabler, C.L. Preventing hypoxia-induced cell death in beta cells and islets via hydrolytically activated, oxygen-generating biomaterials. *Proc. Natl. Acad. Sci. U.S.A.* **109**, 4245-4250 (2012).
58. Cantley, J., Grey, S., Maxwell, P. & Withers, D. The hypoxia response pathway and β -cell function. *Diabetes Obes. Metab.* **12**, 159-167 (2010).
59. Ballian, N. & Brunnicardi, F.C. Islet vasculature as a regulator of endocrine pancreas function. *World J. Surg.* **31**, 705-714 (2007).
60. de Groot, M., Schuurs, T.A. & van Schilfgaarde, R. Causes of limited survival of microencapsulated pancreatic islet grafts. *J. Surg. Res.* **121**, 141-150 (2004).
61. Neufeld, T. et al. The efficacy of an immunoisolating membrane system for islet xenotransplantation in minipigs. *PLoS One* **8**, e70150 (2013).
62. Ludwig, B. et al. Improvement of islet function in a bioartificial pancreas by enhanced oxygen supply and growth hormone releasing hormone agonist. *Proc. Natl. Acad. Sci. U.S.A.* **109**, 5022-5027 (2012).
63. Ludwig, B. et al. Transplantation of human islets without immunosuppression. *Proc. Natl. Acad. Sci. U.S.A.* **110**, 19054-19058 (2013).
64. Henquin, J.-C. Triggering and amplifying pathways of regulation of insulin secretion by glucose. *Diabetes* **49**, 1751-1760 (2000).
65. Hellman, B. et al. Glucose induces oscillatory Ca^{2+} signalling and insulin release in human pancreatic beta cells. *Diabetologia* **37**, S11-S20 (1994).

66. Marchetti, P. et al. Pulsatile insulin secretion from isolated human pancreatic islets. *Diabetes* **43**, 827-830 (1994).
67. O'sullivan, E.S., Vegas, A., Anderson, D.G. & Weir, G.C. Islets transplanted in immunoisolation devices: a review of the progress and the challenges that remain. *Endocr. Rev.* **32**, 827-844 (2011).
68. Buchwald, P., Cechin, S.R., Weaver, J.D. & Stabler, C.L. Experimental evaluation and computational modeling of the effects of encapsulation on the time-profile of glucose-stimulated insulin release of pancreatic islets. *Biomed. Eng. Online* **14**, 28 (2015).
69. De Vos, P. et al. Kinetics of intraperitoneally infused insulin in rats: functional implications for the bioartificial pancreas. *Diabetes* **45**, 1102-1107 (1996).
70. Dionne, K.E., Colton, C.K. & Lyarmush, M. Effect of hypoxia on insulin secretion by isolated rat and canine islets of Langerhans. *Diabetes* **42**, 12-21 (1993).
71. Sato, Y. et al. Cellular hypoxia of pancreatic β -cells due to high levels of oxygen consumption for insulin secretion in vitro. *J. Biol. Chem.* **286**, 12524-12532 (2011).
72. Dulong, J.L. & Legallais, C. A theoretical study of oxygen transfer including cell necrosis for the design of a bioartificial pancreas. *Biotechnol. Bioeng.* **96**, 990-998 (2007).
73. Robertson, R.P., Lanz, K.J., Sutherland, D.E. & Kendall, D.M. Prevention of diabetes for up to 13 years by autoislet transplantation after pancreatectomy for chronic pancreatitis. *Diabetes* **50**, 47-50 (2001).

74. Ludwig, B. & Ludwig, S. Transplantable bioartificial pancreas devices: current status and future prospects. *Langenbecks Arch. Surg.* **400**, 531-540 (2015).
75. Van Der Windt, D.J., Echeverri, G.J., Ijzermans, J.N. & Cooper, D.K. The choice of anatomical site for islet transplantation. *Cell transplantation* **17**, 1005-1014 (2008).
76. Yang, H.K. & Yoon, K.-H. Current status of encapsulated islet transplantation. *J. Diabetes Complications* **29**, 737-743 (2015).
77. Pareta, R. et al. Long-term function of islets encapsulated in a re-designed alginate microcapsule construct in omentum pouches of immune-competent diabetic rats. *Pancreas* **43**, 605 (2014).
78. Kawakami, Y. et al. Successful subcutaneous pancreatic islet transplantation using an angiogenic growth factor-releasing device. *Pancreas* **23**, 375-381 (2001).
79. Wang, W. et al. Reversal of diabetes in mice by xenotransplantation of a bioartificial pancreas in a prevascularized subcutaneous site. *Transplantation* **73**, 122-129 (2002).
80. Vaithilingam, V. & Tuch, B.E. Islet transplantation and encapsulation: an update on recent developments. *Rev. Diabet. Stud.* **8**, 51 (2011).
81. Birch, J.M. & Dickinson, M.H. Spanwise flow and the attachment of the leading-edge vortex on insect wings. *Nature* **412**, 729-733 (2001).
82. Chakraborty, P., Gioia, G. & Kieffer, S.W. Volcanic mesocyclones. *Nature* **458**, 497-500 (2009).
83. Hu, D.L., Chan, B. & Bush, J.W. The hydrodynamics of water strider

- locomotion. *Nature* **424**, 663-666 (2003).
84. San Lee, J. et al. Origin and dynamics of vortex rings in drop splashing. *Nat. Commun.* **6** (2015).
 85. Ungphaiboon, S. et al. Materials for microencapsulation: what toroidal particles (“doughnuts”) can do better than spherical beads. *Soft Matter* **6**, 4070-4083 (2010).
 86. Ruzicka, B. et al. Observation of empty liquids and equilibrium gels in a colloidal clay. *Nat. Mater.* **10**, 56-60 (2011).
 87. Yang, D. et al. Enhanced transcription and translation in clay hydrogel and implications for early life evolution. *Sci. Rep.* **3** (2013).
 88. Dendukuri, D., Pregibon, D.C., Collins, J., Hatton, T.A. & Doyle, P.S. Continuous-flow lithography for high-throughput microparticle synthesis. *Nat. Mater.* **5**, 365-369 (2006).
 89. Du, Y. et al. Sequential assembly of cell-laden hydrogel constructs to engineer vascular-like microchannels. *Biotechnol. Bioeng.* **108**, 1693-1703 (2011).
 90. Fang, A., Gaillard, C. & Douliez, J.-P. Template-free formation of monodisperse doughnut-shaped silica microparticles by droplet-based microfluidics. *Chem. Mater* **23**, 4660-4662 (2011).
 91. Tian, Y., Wu, G., Tian, X., Tao, X. & Chen, W. Novel erythrocyte-like graphene microspheres with high quality and mass production capability via electrospray assisted self-assembly. *Sci. Rep.* **3** (2013).
 92. Xie, J., Jiang, J., Davoodi, P., Srinivasan, M. & Wang, C.-H. Electrohydrodynamic atomization: A two-decade effort to produce and process

- micro-/nanoparticulate materials. *Chem. Eng. Sci.* **125**, 32-57 (2015).
93. Hsiao, M., Lichter, S. & Quintero, L.G. The critical Weber number for vortex and jet formation for drops impinging on a liquid pool. *Phys. Fluids* **31**, 3560-3562 (1988).
 94. Peck, B. & Sigurdson, L. The three-dimensional vortex structure of an impacting water drop. *Phys. Fluids* **6**, 564-576 (1994).
 95. Lu, Y.-C. et al. Designing compartmentalized hydrogel microparticles for cell encapsulation and scalable 3D cell culture. *J. Mater. Chem. B* **3**, 353-360 (2015).
 96. Wang, X.-X. et al. Monodisperse erythrocyte-sized and acid-soluble chitosan microspheres prepared via electrospraying. *RSC Adv.* **5**, 34243-34250 (2015).
 97. Soon-Shiong, P. et al. Insulin independence in a type 1 diabetic patient after encapsulated islet transplantation. *Lancet* **343**, 950-951 (1994).
 98. An, D. et al. Developing robust, hydrogel-based, nanofiber-enabled encapsulation devices (NEEDs) for cell therapies. *Biomaterials* **37**, 40-48 (2015).
 99. Ma, M. et al. Core-shell hydrogel microcapsules for improved islets encapsulation. *Adv. Healthc. Mater.* **2**, 667-672 (2013).
 100. McEvoy, M.A. & Correll, N. Materials that couple sensing, actuation, computation, and communication. *Science* **347**, 1261689 (2015).
 101. Fusco, S. et al. An integrated microrobotic platform for on-demand, targeted therapeutic interventions. *Adv. Mater.* **26**, 952-957 (2014).
 102. Weir, G.C. & Susan, B.-W. Scientific and political impediments to successful islet transplantation. *Diabetes* **46**, 1247-1256 (1997).

103. Orive, G. et al. Cell encapsulation: technical and clinical advances. *Trends Pharmacol. Sci.* **36**, 537-546 (2015).
104. Onoe, H. et al. Metre-long cell-laden microfibres exhibit tissue morphologies and functions. *Nat. Mater.* **12**, 584-590 (2013).
105. Dufrane, D., Goebbels, R.-M. & Gianello, P. Alginate macroencapsulation of pig islets allows correction of streptozotocin-induced diabetes in primates up to 6 months without immunosuppression. *Transplantation* **90**, 1054-1062 (2010).
106. Khademhosseini, A. & Langer, R. Microengineered hydrogels for tissue engineering. *Biomaterials* **28**, 5087-5092 (2007).
107. Lee, K.Y. & Mooney, D.J. Hydrogels for tissue engineering. *Chem. Rev.* **101**, 1869-1880 (2001).
108. Calvert, P. Hydrogels for soft machines. *Adv. Mater.* **21**, 743-756 (2009).
109. Sun, J.-Y. et al. Highly stretchable and tough hydrogels. *Nature* **489**, 133-136 (2012).
110. Peppas, N., Huang, Y., Torres-Lugo, M., Ward, J. & Zhang, J. Physicochemical foundations and structural design of hydrogels in medicine and biology. *Annu. Rev. Biomed. Eng.* **2**, 9-29 (2000).
111. Gong, J.P., Katsuyama, Y., Kurokawa, T. & Osada, Y. Double-network hydrogels with extremely high mechanical strength. *Adv. Mater.* **15**, 1155-1158 (2003).
112. Huang, T. et al. A novel hydrogel with high mechanical strength: a macromolecular microsphere composite hydrogel. *Adv. Mater.* **19**, 1622-1626 (2007).

113. Li, D. & Xia, Y. Electrospinning of nanofibers: reinventing the wheel? *Adv. Mater.* **16**, 1151-1170 (2004).
114. Agarwal, S., Wendorff, J.H. & Greiner, A. Progress in the field of electrospinning for tissue engineering applications. *Adv. Mater.* **21**, 3343-3351 (2009).
115. Liu, W., Thomopoulos, S. & Xia, Y. Electrospun nanofibers for regenerative medicine. *Adv. Healthc. Mater.* **1**, 10-25 (2012).
116. Song, W. et al. Nanofibrous microposts and microwells of controlled shapes and their hybridization with hydrogels for cell encapsulation. *ACS Appl. Mater. Interfaces* **6**, 7038-7044 (2014).
117. Stankus, J.J. et al. Fabrication of cell microintegrated blood vessel constructs through electrohydrodynamic atomization. *Biomaterials* **28**, 2738-2746 (2007).
118. Panseri, S. et al. Electrospun micro-and nanofiber tubes for functional nervous regeneration in sciatic nerve transections. *BMC biotechnol.* **8**, 39 (2008).
119. Xu, C. et al. Feeder-free growth of undifferentiated human embryonic stem cells. *Nat. Biotechnol.* **19**, 971-974 (2001).
120. Lacy, P.E. & Kostianovsky, M. Method for the isolation of intact islets of Langerhans from the rat pancreas. *Diabetes* **16**, 35-39 (1967).
121. Ricordi, C. et al. Islet isolation assessment in man and large animals. *Acta diabetologia latina* **27**, 185-195 (1990).
122. Washburn, E.W. The dynamics of capillary flow. *Phys. Rev.* **17**, 273 (1921).
123. Balguid, A. et al. Tailoring fiber diameter in electrospun poly (ϵ -caprolactone) scaffolds for optimal cellular infiltration in cardiovascular tissue engineering.

- Tissue Eng. Part A* **15**, 437-444 (2008).
124. Andrejcsk, J.W. et al. Paracrine exchanges of molecular signals between alginate-encapsulated pericytes and freely suspended endothelial cells within a 3D protein gel. *Biomaterials* **34**, 8899-8908 (2013).
 125. King, A., Sandler, S. & Andersson, A. The effect of host factors and capsule composition on the cellular overgrowth on implanted alginate capsules. *J. Biomed. Mater. Res. A* **57**, 374-383 (2001).
 126. De Vos, P. Cell encapsulation: ready for the next step. *Adv. Drug Deliv. Rev.* **67-68**, 1-2 (2014).
 127. Wang, T. et al. An encapsulation system for the immunoisolation of pancreatic islets. *Nat. Biotechnol.* **15**, 358-362 (1997).
 128. Shin, H., Jo, S. & Mikos, A.G. Biomimetic materials for tissue engineering. *Biomaterials* **24**, 4353-4364 (2003).
 129. Sill, T.J. & von Recum, H.A. Electrospinning: applications in drug delivery and tissue engineering. *Biomaterials* **29**, 1989-2006 (2008).
 130. Martinsen, A., Storrø, I. & Skjærk-Bræk, G. Alginate as immobilization material: III. Diffusional properties. *Biotechnol. Bioeng.* **39**, 186-194 (1992).
 131. Vacanti, N.M. et al. Localized delivery of dexamethasone from electrospun fibers reduces the foreign body response. *Biomacromolecules* **13**, 3031-3038 (2012).
 132. Zhang, L. et al. Zwitterionic hydrogels implanted in mice resist the foreign-body reaction. *Nat. Biotechnol.* **31**, 553-556 (2013).
 133. Khanna, O., Moya, M.L., Opara, E.C. & Brey, E.M. Synthesis of multilayered

- alginate microcapsules for the sustained release of fibroblast growth factor-1. *J. Biomed. Mater. Res. A* **95**, 632-640 (2010).
134. Ma, M. et al. Development of cationic polymer coatings to regulate foreign-body responses. *Adv. Mater.* **23** (2011).
135. Kroon, E. et al. Pancreatic endoderm derived from human embryonic stem cells generates glucose-responsive insulin-secreting cells in vivo. *Nat. Biotechnol.* **26**, 443-452 (2008).
136. Rezanian, A. et al. Maturation of human embryonic stem cell–derived pancreatic progenitors into functional islets capable of treating pre-existing diabetes in mice. *Diabetes* **61**, 2016-2029 (2012).
137. Lacy, P.E., Hegre, O.D., Gerasimidi-Vazeou, A., Gentile, F.T. & Dionne, K.E. Maintenance of normoglycemia in diabetic mice by subcutaneous xenografts of encapsulated islets. *Science* **254**, 1782-1784 (1991).
138. Lanza, R.P. et al. Xenotransplantation of canine, bovine, and porcine islets in diabetic rats without immunosuppression. *Proc. Natl. Acad. Sci. U.S.A.* **88**, 11100-11104 (1991).
139. Sörenby, A.K. et al. Preimplantation of an immunoprotective device can lower the curative dose of islets to that of free islet transplantation—Studies in a rodent model. *Transplantation* **86**, 364-366 (2008).
140. Scharp, D.W. et al. Protection of encapsulated human islets implanted without immunosuppression in patients with type I or type II diabetes and in nondiabetic control subjects. *Diabetes* **43**, 1167-1170 (1994).
141. Calafiore, R. & Basta, G. Clinical application of microencapsulated islets: actual

- prospectives on progress and challenges. *Adv. Drug Deliv. Rev.* **67**, 84-92 (2014).
142. Ledford, H. Stem-cell success poses immunity challenge for diabetes. *Nature* **514** (2014).
143. Colton, C.K. Oxygen supply to encapsulated therapeutic cells. *Adv. Drug Deliv. Rev.* **67**, 93-110 (2014).
144. Papas, K.K., Avgoustiniatos, E.S. & Suszynski, T.M. Effect of oxygen supply on the size of implantable islet-containing encapsulation devices. *Panminerva Med.* **58**, 72-77 (2016).
145. Smink, A.M., Faas, M.M. & de Vos, P. Toward engineering a novel transplantation site for human pancreatic islets. *Diabetes* **62**, 1357-1364 (2013).
146. Matsumoto, S., Tomiya, M. & Sawamoto, O. Current status and future of clinical islet xenotransplantation. *J. Diabetes* **8**, 483-493 (2016).
147. Lindvall, O. & Wahlberg, L.U. Encapsulated cell biodelivery of GDNF: a novel clinical strategy for neuroprotection and neuroregeneration in Parkinson's disease? *Exp. Neurol.* **209**, 82-88 (2008).
148. Zheng, Y. et al. Directional water collection on wetted spider silk. *Nature* **463**, 640-643 (2010).
149. Srinivasarao, M., Collings, D., Philips, A. & Patel, S. Three-dimensionally ordered array of air bubbles in a polymer film. *Science* **292**, 79-83 (2001).
150. Bognitzki, M. et al. Nanostructured fibers via electrospinning. *Adv. Mater.* **13**, 70-72 (2001).
151. Quéré, D., Di Meglio, J.-M. & Brochard-Wyart, F. Spreading of liquids on

- highly curved surfaces. *Science* **249**, 1256-1261 (1990).
152. Duprat, C., Protiere, S., Beebe, A. & Stone, H. Wetting of flexible fibre arrays. *Nature* **482**, 510-513 (2012).
 153. Akbari, M. et al. Composite living fibers for creating tissue constructs using textile techniques. *Adv. Funct. Mater.* **24**, 4060-4067 (2014).
 154. Bray, N. Biomaterials: Modified alginates provide a long-term disguise against the foreign body response. *Nat. Rev. Drug Discov.* **15**, 158-159 (2016).
 155. Gurruchaga, H. et al. Advances in cell encapsulation technology and its application in drug delivery. *Expert. Opin. Drug. Deliv.* **12**, 1251-1267 (2015).
 156. De Vos, P., Wolters, G., Fritschy, W. & Van Schilfgaarde, R. Obstacles in the application of microencapsulation in islet transplantation. *Int. J. Artif. Organs* **16**, 205-212 (1993).
 157. Omer, A. et al. Survival and maturation of microencapsulated porcine neonatal pancreatic cell clusters transplanted into immunocompetent diabetic mice. *Diabetes* **52**, 69-75 (2003).
 158. Bruin, J.E. et al. Treating diet-induced diabetes and obesity with human embryonic stem cell-derived pancreatic progenitor cells and antidiabetic drugs. *Stem Cell Reports* **4**, 605-620 (2015).
 159. Stokes, R.A. et al. Transplantation sites for human and murine islets. *Diabetologia* **60**, 1961-1971 (2017).
 160. Pagliuca, F.W. et al. Generation of functional human pancreatic β cells in vitro. *Cell* **159**, 428-439 (2014).
 161. Anonymous First stem cell-derived islets in humans. *Nat. Biotechnol.* **32**, 959

- (2014).
162. Dolgin, E. Encapsulated this. *Nat. Med.* **9**, 104-107 (2014).
 163. Jacobs-Tulleneers-Thevissen, D. et al. Beta Cell Therapy Consortium EU-FP7 Sustained function of alginate-encapsulated human islet cell implants in the peritoneal cavity of mice leading to a pilot study in a type 1 diabetic patient. *Diabetologia* **56**, 1605-1614 (2013).
 164. Tuch, B.E. et al. Safety and viability of microencapsulated human islets transplanted into diabetic humans. *Diabetes Care* **32**, 1887-1889 (2009).
 165. Raof, N.A., Padgen, M.R., Gracias, A.R., Bergkvist, M. & Xie, Y. One-dimensional self-assembly of mouse embryonic stem cells using an array of hydrogel microstrands. *Biomaterials* **32**, 4498-4505 (2011).
 166. Lee, K.H., Shin, S.J., Park, Y. & Lee, S.H. Synthesis of cell-laden alginate hollow fibers using microfluidic chips and microvascularized tissue-engineering applications. *Small* **5**, 1264-1268 (2009).
 167. Russ, H.A. et al. Controlled induction of human pancreatic progenitors produces functional beta-like cells in vitro. *EMBO J.* **34**, 1759-1772 (2015).